November 2020

Cost Efficient Algorithms and Methods for Spectral Efficiency in Future Radio Access

Murat Karabacak
University of South Florida

Follow this and additional works at: https://digitalcommons.usf.edu/etd

Part of the Electrical and Computer Engineering Commons

Cost Efficient Algorithms and Methods for Spectral Efficiency in Future Radio Access

by

Murat Karabacak

A dissertation submitted in partial fulfillment
of the requirements for the degree of
Doctor of Philosophy
Department of Electrical Engineering
College of Engineering
University of South Florida

Major Professor: Huseyin Arslan, Ph.D.
Gokhan Mumcu, Ph.D.
Nasir Ghani, Ph.D.
Selcuk Kose, Ph.D.
Srinivas Katkoori, Ph.D.

Date of Approval:
November 3, 2020

Keywords: Beamforming, Narrow Beam, Multiplexing, Milimeter-Wave

Dedication

To my renunciant & enduring parents, for all their support.

It is always fun to learn new things, find clever solutions, and provide means to improve our knowledge and experience. However, this journey was also sometimes hard, sometimes exhausting, and sometimes *insane*. I will never forget all the experience I got from this journey and I will always remember the people I have met in this long adventure.

I would like to close my acknowledgment with the following sentence *The definition of insanity is doing the same thing over and over again and expecting different results* which is widely credited to Albert Einstein on many occurrences. That inspired me to seek for slight differences to improve my solutions whenever I have failed to solve my problems. You will see some small changes can create miracles.

Table of Contents

List of Tables

List of Figures

Abstract

The growing interest in data-hungry wireless applications of mobile devices has led the cellular industry to look for new frequencies and new techniques for utilization of next-generation wireless technologies. As millimeter-wave (mmWave) communication becoming a promising solution, It can provide greater bandwidth and higher data rates in future radio access. While in the hostile environment of mmWave bands, the signals suffer from high propagation loss, the smaller wavelengths of mmWave frequencies make it possible to practically pack a large number of antennas with reasonable form factors. Thus, mmWave communication can provide directional transmission with high gain antenna arrays to penetrate the hostile environment. Digital, analog, and hybrid beamforming are commonly used methods to form directional transmission using antenna arrays. However, as the Millimeter-wave (mmWave) components are expensive, even simple analog beamforming approach would need phase shifters, control circuits, and may still require an expensive circuit design. The increase on the array size, also complicates the hardware and algorithms to control the generated beams which also require more advanced resource allocation including beam-user association.

In this dissertation, first, data rate and energy efficiency performance of mmWave wireless communication systems consisting of a new lens antenna subarray (LAS) based hybrid multiple-input-multiple-output (MIMO) architecture is investigated. LAS architecture simplifies hardware requirements and lowers the cost by reducing the number of phase shifters while potentially maintaining near identical beam-steering and gain capabilities with respect to the traditional hybrid MIMO architecture (TA). The LAS architecture degenerates into TA or single lens antenna array architecture (SLA) when the lens diameter of the subarray is reduced or enlarged, respectively. Second, dynamic sidelobe multiplexing (DSM) algorithm is proposed to overcome restrictions that comes from limited number of radio-frequency (RF) chain usage. The proposed multiplexing

technique precodes the transmitted data over transmitter beams in order to open up a new path to the receiver. Therefore, the proposed method provides an opportunity to exceed the limits of conventional hardware usage in beamspace MIMO. Third, an algorithm for joint optimization of antenna parameters with load balancing is presented to distribute users to cells while optimizing the antenna parameters. The proposed approach does not only change the serving range of each cell but also re-assign users to cells for effective system capacity to provide maximized resource allocation. Fourth, another resource allocation problem is investigated in Manhattan grid layout mobility performance of Macrocell-assisted small Cell concept. Fifth, perturbed antenna array geometries are investigated for a novel authentication approach which introduces an identity to formed beams. Sixth, RF domain Doppler emulator, which is compact and easy to control, is presented to measure signal characteristics under frequency dispersive channel conditions for swift evaluation of developed algorithms.

Chapter 1: Introduction

In the previous generations of wireless communication, systems were able to provide sufficient capacity with one large cell. Simple frequency reuse techniques have been implemented to improve the performance [1]. However, tremendous growth in the variety and the number of the wireless applications results in a hunger more and more data rates. This growing interest in data greedy wireless applications made the cellular industry to seek new frequencies and new techniques for utilization of next-generation wireless technologies [2,3]. mmWave communication becomes a promising technology to support wireless systems for larger bandwidth and higher data rates in fifth generation (5G) networks [4–7]. Federal Communications Commission (FCC) has already stepped forward and opened 3.85 GHz commercial spectrum at 28 GHz, 37 GHz, and 38 GHz including 7 GHz free access spectrum at 67.5 GHz [8].

Hostile channel characteristics in mmWave bands, i.e. atmospheric absorption (upto 15 dB/km loss), sensitivity to blockage (upto 40 dB loss), had kept the band usage challenging for dynamic access multiuser communication [9–11]. It is well known that in mmWave bands, the communication signals suffer from high propagation loss [12, 13]. Because of those problems methods and techniques are required to compensate strong path-loss while providing accessto multiple users. As an important feature of mmWave bands, the smaller wavelengths make it possible to practically pack a large number of antennas with reasonable form factors. Thus, mmWave communication can provide directional transmission with high gain antenna arrays.

Beamforming algorithms are used to optimize transmission direction and overcome harsh channel conditions (i.e., high attenuation, blockage) [14–17]. There are three beamforming architectures presented in the literature (i.e. Digital, analog, and hybrid beamforming) [18]. As the mmWave components are expensive, hybrid or analog only structures are expected to be im-

plemented to prevent usage of many DAC/ADC components [19]. However, even simple analog beamforming approach would require phase shifters, control circuits, and still hard to implement. The increase on the array size, also complicates the hardware and algorithms to control the generated beams. As the current systems can introduce upto 256 antenna elements [20], it is challenging to implement the system in a cost effective way. The cost effective solutions are needed because mmWave transmission points (TPs) are planned to be densely deployed to increase the chance of establishing LOS links [11]. Since available high bandwidth and spatial diversity can be utilized to provide self-hauling capability over a wireless link, mmWave systems already show a promising cost effective feature for rapid deployment [20].

1.1 Overview of Techniques to Establish mmWAve Communication

Directive communication is an essential technique for mmWave communication to compensate strong propagation via focusing transmitted signal towards receiver direction [20]. Therefore, it is a key element in mmWave systems to overcome harsh channel conditions of the band. To achieve high beamforming gains, TPs and user equipments need to construct their beams towards each other. In this section, we discuss on beamforming architectures following with beam association methods and their relation to the architecture. Then, we review the current approach to the beam design from system perspective as TPs, and discuss on hardware complexity.

1.1.1 Beamforming Techniques

Steerable beamforming is implemented in three basic structures: Digital beamforming, Analog beamforming, and Hybrid beamforming. While the signal is processed in digital domain for digital beamforming, in analog beamforming, the signal is processed on set of analog RF/IF components. As the name implies hybrid approach is implemented in both domains.
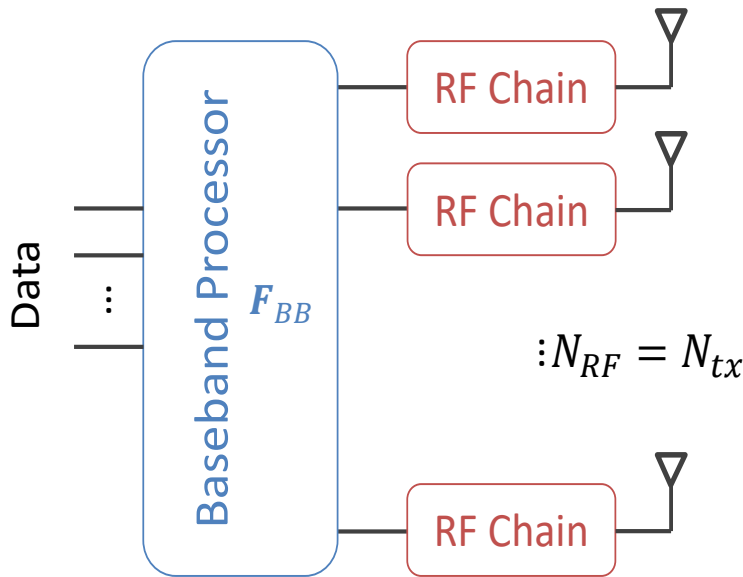
Figure 1.1: Fully digital beamforming architecture

Digital flexibility in baseband processing allows better control on the formed beam via single user, multi-user, or multi-cell precoding algorithms. As shown in Fig. 1.1, digital beamforming algorithm would require a separate RF chain in each antenna path. Considering the wide-band requirements of mmWave systems, ADC/DACs implemented in each RF chain should be able to work in large dynamic range [20]. However, with the current technology, designing the TPs with already expensive ADC/DACs and implementing upto 256 RF chains would be extremely cost inefficient especially for dense deployment [19, 21].

In analog beamforming, the signal is processed in RF domain using network of phase shifters and control circuit. Block diagram of this analog processing is shown in Fig. 1.2. Its simple design is an immediate solution to overcome the hardware limitations on the hardware complexity and power consumption of mmWave systems [20]. However, analog beamforming only supports single stream transmission at a time.
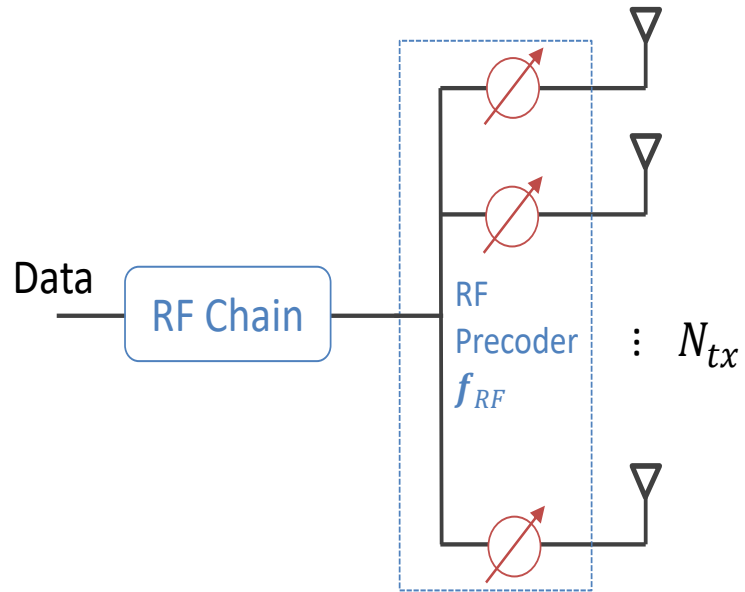
Figure 1.2: Analog only beamforming architecture
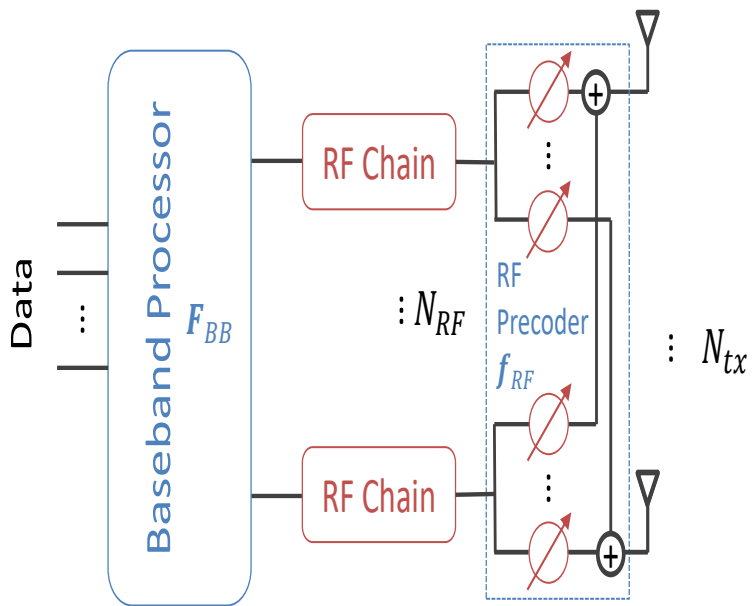
Figure 1.3: Hybrid beamforming architecture
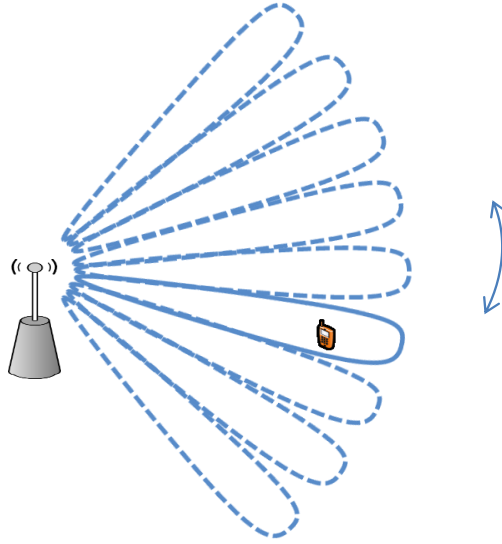
Figure 1.4: Illustration of exhaustive search method

Hybrid approach is driven from digital beamforming aproach with the goal of reducing required number of RF chains while providing similar performances [22]. Fig. 1.3 shows a block diagram for hybrid architecture. Compared to RF beamforming, N_{RF} number of RF chains could support N_{RF} parallel data streams, however each RF chain would require a separate phase shifter network to implement RF beamforming. Further details on mmWave beamforming can be found in [19].

1.1.2   Beam Association

In cellular communication, the network must be aware of the users in the coverage area. Implementation of focused transmission with narrow beams requires more detailed awareness within the coverage area, i.e. direction of available users. Therefore the TPs perform a periodical scan using beam search algorithms to detect and synchronize on new users [23, 24]. Commonly used search algorithms are exhaustive and iterative search algorithms.

First Step   Second Step
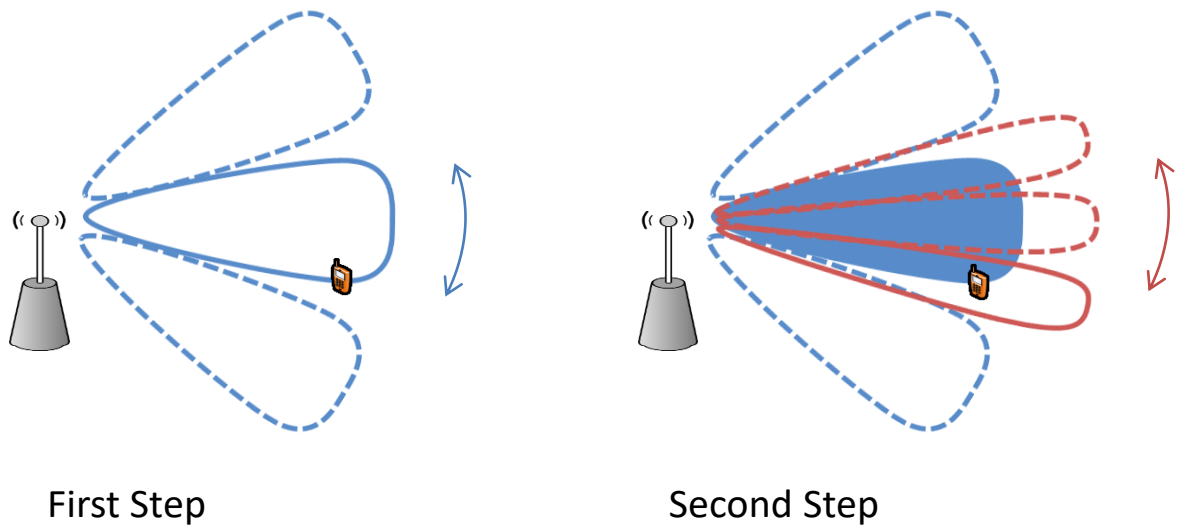
Figure 1.5: Illustration of iterative search method

In exhaustive search shown in Fig. 1.4, the user and TP makes trials on every possible beam direction (for each beamforming precoder) and select the best. As the beams get narrower, the required number of trials would increase and cause increased discovery delays. The iterative approach shown in Fig. 1.5, would solve delay problem, since iterative search starts with wider beams and get narrower to refine the scan in the best direction. Unfortunately, iterative search cannot be implemented for analog beamforming with only phase shifter networks, since this algorithm would require amplitude changes in precoder to manipulate beam width.

1.1.3 Transmission Points

Transmission points electrically steer/switch the high gain beams to identify and communicate with the users. An illustration of TP setup for mmWave can be given as in Fig 1.6. In the figure, the TPs are designed to serve every direction and each antenna array assumed to serve $90°$ sectors. In the current design trend, large antenna arrays are capable to generate high gain narrow beams and they are also designed to electronically change the direction of the beam to cover all
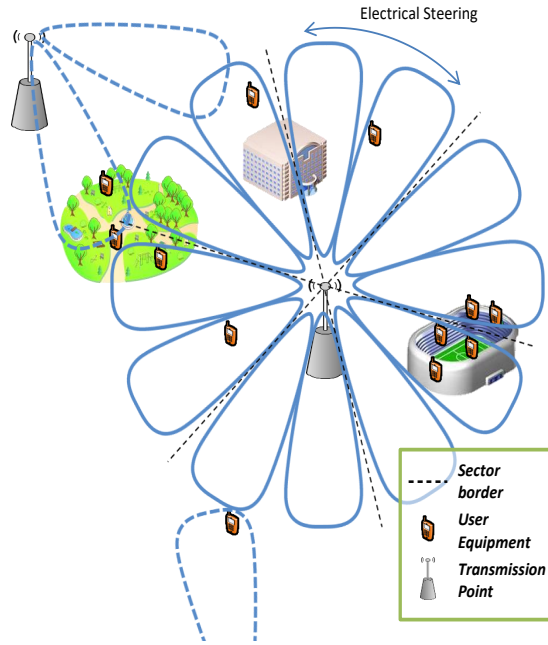
Figure 1.6: An illustration of transmission points implementing beamforming in mmWave networks.

the possible directions. Therefore, the hardware complexity increases to provide narrower beams. With the goal of serving surrounding users from one point, the beams are required to be settled as quickly as possible from one user to another. Thus a seamless transmission can be achieved [25] to chance active beam in time.

Dense deployment and expectation of few number of users per cell implies that mmwave links will be established along a few direction at a time. In Figure 1.6, users are gathered towards a certain directions within each sector. This might happen depending on changing channel conditions and daily life events. While blockage (e.g. buildings) might prevent TP to communicate users behind it, hotspot (e.g. stadium event) attracts more users to its locations. In this kind of situation field of view (FoV) of electrical steering should be focused more towards the hotspot direction while prevent utilizing resources towards the blockage. Thus, achieving 256 (even more) antennas array gains would be more cost effective for dense deployment of the mmWave systems.

Currently discussed/proposed approaches for mm-wave wireless network beam management remain mostly impractical for implementing very narrow beams due to high cost associated with constructing and deploying the needed TP and user hardware. For example, despite the physically small wavelengths, high gain mm-wave antenna arrays (especially those operating below 60 GHz) are not suitable for on-chip integration due to their relatively large physical size. Above 60 GHz, wafer-scale integration of mm-wave antennas [26, 27] continues to be a challenge and a major cost driver due to the need for a large number of antenna elements to realize the high gain apertures. Silicon-based phased arrays potentially reduce system development to commercial timescales. A number of bottlenecks, however, affect feasibility of the latter topologies in addition to the aforementioned footprint concerns. Specifically, low-resistivity substrates of mainstream silicon processes preclude on-chip integration of an efficient antenna, rendering the off-chip radiator as the only practical option, while potentially introducing routing parasitics on typical array platforms (e.g. bond wires between the chips and a holder PCB). Moreover, RF circuit design becomes more challenging as the carrier frequencies extend into the mm-wave region due to several factors such as reduced gain of analog circuits, pronounced effects of device/interconnect parasitics, wide channel bandwidth requirements, and increased sensitivity to process, bias voltage and temperature. Consequently, deployment of mm-wave networks within the mass-scale, communications market necessitates joint network and hardware innovations that complement each other.

1.2   Dissertation Outline

1.2.1   Lens Antenna Subarrays in mmWave Hybrid MIMO Systems

Data rate and energy efficiency performance of mmWave wireless communication systems consisting of a new lens antenna subarray (LAS) based hybrid multiple-input-multiple-output (MIMO) architecture is investigated. LAS architecture simplifies hardware requirements and lowers the cost by reducing the number of phase shifters while potentially maintaining near identical beam-steering and gain capabilities with respect to the traditional hybrid MIMO architecture (TA). The LAS architecture degenerates into TA or single lens antenna array architecture (SLA) when the

lens diameter of the subarray is reduced or enlarged, respectively. It is shown that under mmWave channel scattering conditions, LAS architecture operates with a data rate approaching that of TA while significantly exceeding the data rate of the SLA. Due to the reduced hardware complexity and power consumption, LAS architectures operate with a significantly improved energy efficiency. In an example system consisting of 64 and 16 transmitter and receiver antennas with 2 RF chains, it is shown that the LAS architecture operates with $2\times$ energy efficiency and 98% spectrum efficiency. In a larger hybrid MIMO antenna systems, LAS architecture is expected to benefit even more.

1.2.2 Dynamic Sidelobe Multiplexing in Beamspace MIMO Systems

Recent studies on multiplexing concept over beamspace MIMO can reduce the need for using phase shifters while keeping the directivity performance at similar levels. Thus, beamspace MIMO provides cost-effective and simple hardware designs for millimeter-wave (mmWave) systems. However, the number of users/streams that can be supported at the same time-frequency resource is limited to the number of radio-frequency (RF) chains. In this letter, to overcome this restriction, dynamic sidelobe multiplexing (DSM) algorithm is proposed. The proposed multiplexing technique precodes the transmitted data over transmitter beams in order to open up a new path to the receiver. Therefore, the proposed method provides an opportunity to exceed the limits of conventional hardware usage in beamspace MIMO. The numerical results show that the proposed approach enhance the system performance for more than 50% compared to conventional beamspace MIMO techniques.

1.2.3 Joint Approach to Beam Optimization and User Association

Efficiently managed user-cell association is important for self-optimization of communication networks. Edge user performance and fairness of the service quality can be improved by offloading heavily loaded cells to neighboring cells. In this paper, an algorithm for joint optimization of antenna parameters with load balancing is presented to distribute users to cells while

optimizing the antenna parameters. The proposed approach does not only change the serving range of each cell but also re-assign users to cells for effective system capacity. The performance evaluations show that the presented approach increases the edge user capacity by 27% compared to conventional approach.

1.2.4 Mobility Performance of Macrocell-Assisted Small Cells in Manhattan Model

Macrocell-assisted small cell concepts, such as "Phantom cell concept" and "soft cell concept", have been proposed previously for interference management, flexible cell planning, and energy saving in dense small cell deployments. These concepts require macrocell involvement to improve links between small cell and user. Since target implementation areas of the concepts are crowded urban areas (e.g. downtown New York City) to satisfy the data need, more realistic simulations are needed to be implemented compared to conventional evaluations. In this paper, as a new approach to urban area LTE simulations, Manhattan grid layout is presented and implemented for mobility performance of Macrocell-assisted small Cell concept. The results show that the macrocell involvement to improve mobility performance gives a great advantage compared to using the conventional mobility solution for dense small cell deployments.

1.2.5 Arraymetrics: Authentication Through Chaotic Antenna Array Geometries

Advances in computing have resulted in an emerging need for multi-factor authentication using an amalgamation of cryptographic and physical keys. This letter presents a novel authentication approach using a combination of signal and antenna activation sequences, and most importantly, perturbed antenna array geometries. Possible degrees of freedom in perturbing antenna array geometries affected physical properties and their detection are presented. Channel estimation for the plurality of validly authorized arrays is discussed. Accuracy is investigated as a function of SNR and number of authorized arrays. It is observed that the proposed authentication scheme can provide 1% false authentication rate at $10\,\mathrm{dB}$ SNR, while it is achieving less than 1% missed authentication rates.

1.2.6 RF Circuit Implementation of a Real-Time Frequency Spread Emulator

Despite their reliability, on-site measurements are time-consuming and costly actions for the evaluation of new devices. Channel emulators are widely utilized measurement instruments to generate desired environmental channel effects in laboratory environments. Within these instruments, baseband emulators are expensive, and reverberation chambers provide limited control of the channel. However, radio frequency (RF) circuit implementation of channel emulators provides an affordable and an easy tool to test performances of new systems and methods under different channel effects. In this study, a new RF domain Doppler emulator, which is compact and easy to control, is presented for measuring signal characteristics under frequency dispersive channel conditions. The circuit has been implemented using variable attenuators, switches, and power splitters to emulate Doppler spread of air-ground channels, and the performance is evaluated through measurements. It is observed that the emulator indeed generates the desired Doppler model close enough to replicate environmental channels for mobile applications in laboratory environments.

Chapter 2: Lens Antenna Subarrays in mmWave Hybrid MIMO Systems

Multimedia driven technologies and multifunctional wireless devices have pushed the existing wireless systems to their limits in traditionally utilized spectrum and increased the desire to operate at higher frequency bands [7, 9]. FCC has already stepped forward and opened mmWave band for future radio access [8]. It is well known that in mmWave bands, the communication signals suffer from high propagation loss [12, 13]. On the other hand, as an important feature of mmWave bands, the smaller wavelengths make it possible to practically pack a large number of antennas with reasonable form factors. Thus, mmWave communication can provide directional transmission with high gain antenna arrays. Beamforming algorithms are used to optimize transmission direction and overcome harsh channel conditions (i.e., high attenuation, blockage) [14–17]. Unlike the lower frequency bands, cost and power consumption of hardware components in mmWave band limits the widespread utilization of mmWave communication systems. This problem is further exacerbated with the desire of including radio frequency (RF) chains and analog to digital (ADC) / digital to analog (DAC) converters per antenna element since high gain antenna arrays consist of many elements. Thus, hybrid multiple input multiple output (MIMO) architecture that packs fewer RF chains at the back of the high gain antenna array has attracted great interest over the recent years [28].

Hybrid MIMO architecture prevents usage of many RF chains and ADC/DACs [19, 28–31]. Although number of RF chains are less than the number of antenna elements, the complexity and power consumption of hybrid MIMO architecture continues to be challenging for hardware implementations due to need for large number of analog RF components (e.g. phase shifters). The implementation and power consumption challenges increase for larger antenna arrays such as 256 antenna elements [20] or more to satisfy necessary system performance. In addition to

hardware complexity and cost, recent studies demonstrate that the DC power consumed by the phase shifters (and their variable gain amplifiers) becomes critical [32, 33]. This problem is exacerbated in the traditional hybrid MIMO architecture (TA) since the number of phase shifters becomes multiple of the number of RF chains and antennas employed within the architecture. Therefore, several alternative architectures that reduce the total number of phase shifters have been recently investigated with regards to their spectrum and energy efficiencies [33]. These alternative architectures have reduced the total number of phase shifters with combinations of replacing them with less power demanding RF switches, implementing different signal summation paths, and grouping elements into smaller phased arrays. However, these investigations have shown that although alternative architectures consume less power (due to the removal of phase shifters), they operate with less spectrum efficiency. Hence, the energy efficiency (i.e. data rate / power consumption) have remained very similar to the traditional hybrid MIMO architecture (TA) [33]. A different approach to the problem is presented in [34, 35] using a few bit ADC receivers, where in the receiver a cost efficient ADC with less number of quantization levels is implemented.

The main issue with the proposed alternative hybrid MIMO architectures in [33] is related to their inability to generate the same antenna gain and similar beamforming as TA could do. For example, one classical approach for reducing the total number of phase shifters in a phased antenna array is the subarraying technique [36]. However, classical subarraying significantly reduces the beam steering range that can be achieved without grating lobes. Consequently, although the subarray may operate as well as a TA in line-of-sight (LOS) communications falling within a narrow scan range, it cannot provide a large scan range and demonstrate full capability to constructively add the multipath scattering with optimum coefficients. On the other hand, single lens antenna array architecture (SLA) provides a similar capability to TA. They consist of an electrically large lens with antenna elements placed at the focal plane. Switching the excitation element also switches the radiated beam. The beam is high in gain and can be steered over a large angle. Since beam steering is performed with switches, hardware implementation is simplified and power consumption is reduced, typically at the expense of a larger antenna structure. Consequently, a number of studies

have proposed usage of SLAs in mmWave wireless communication systems [37–41]. Reference [37] investigates SLA with 1 RF chain for mmWave systems. In [38], SLA supporting RF chains that are much fewer in number than the total number of antennas is investigated for MIMO communications. Reference [42] provides multi-user extension to the SLA. In [40], pre-compensation of path delays is proposed to implement low complexity single carrier transmission. In [41], wide band beam selection algorithm is presented to improve sum-rate of the system.

The main drawbacks of SLAs can be considered to be their larger size and limitation for the beamforming precoding. In SLA, an RF chain gets connected to only one antenna element at a given time. In multipath environment, this prevents to implement a precoder/combiner that will optimize the shape of the beam and related coefficients to constructively combine signals arriving from multipaths. Hence, SLA is expected to underperform in spectrum efficiency in a multipath environment. In this chapter, we propose to investigate spectrum and energy efficiency of a recently introduced architecture: lens antenna subarrays (LAS) [43, 44]. LAS architecture is shown in Fig. 2.1 and compared to the TA with Fig. 2.2. Signal from an RF chain (out of a total of N^{RF} chains) gets connected to L discrete lenses after passing from a phase shifter. Within the lens, the signal gets delivered to an antenna element by a RF switch network. The total number of antennas is N where $M = N/L$ denotes the number of antennas per lens. The total physical footprint of the lenses are approximately equal to the physical size of the half-wave spaced N antenna elements so that the TA and LAS architectures exhibit similar antenna gains. The total number of phase shifters are reduced by a factor of M. However, despite this reduction, each LAS maintains electronic beam-steering capability. Hence, the LAS architecture can potentially provide similar beam steering range with the TA and SLA. In fact, one can consider LAS architecture to be degenerating into a TA and
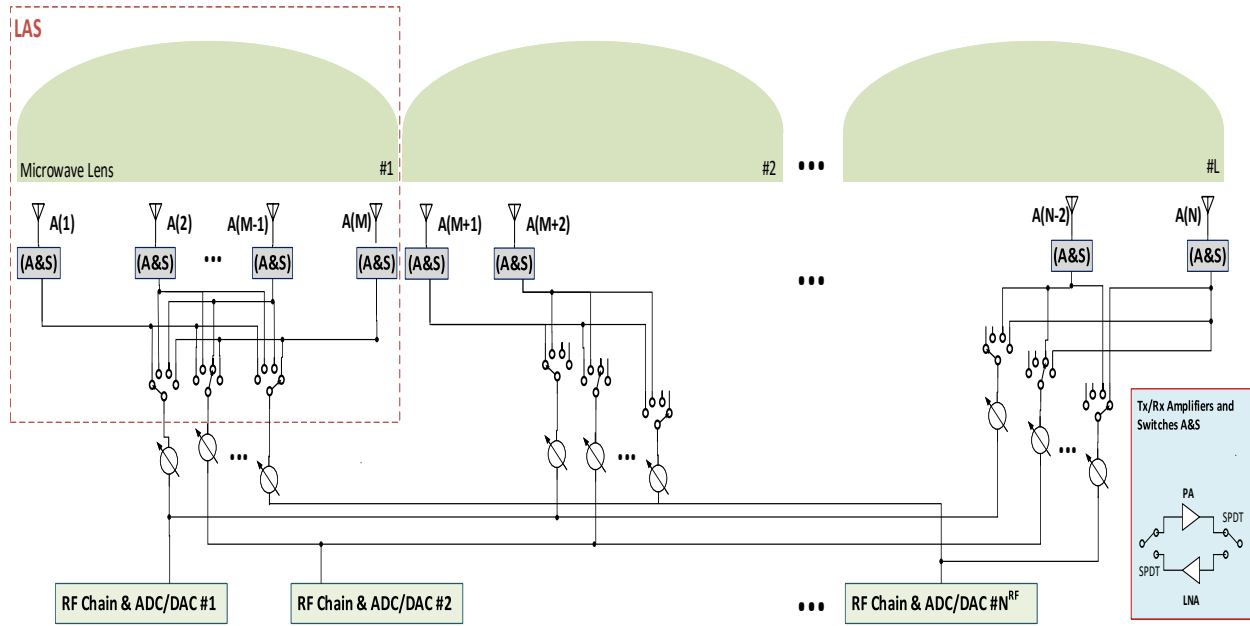
Figure 2.1: Lens antenna subarray (LAS) hybrid MIMO architecture.

SLA with the choices of $M = 1$ and $M = N$, respectively. Power consumption is expected to be reduced as M increases towards the SLA, however, this will negatively impact the spectrum efficiency in multipath environments. In contrast, reducing M will increase power consumption, but also increase its spectrum efficiency.

In this chapter, we demonstrate for the first time that the proper choice of M can be utilized to obtain a better energy efficiency (i.e. data rate per power consumption) in mmWave communication systems as opposed to the conventional wisdom of using TA or SLA. Contributions of this chapter can be summarized as

- For the first time, spectrum and energy efficiency of LAS architecture is investigated.

- Multiple stream and multiple RF chain scenarios for the LAS architecture are presented.

- The LAS architecture is evaluated with exhaustive search search algorithms to prove its capabilities.
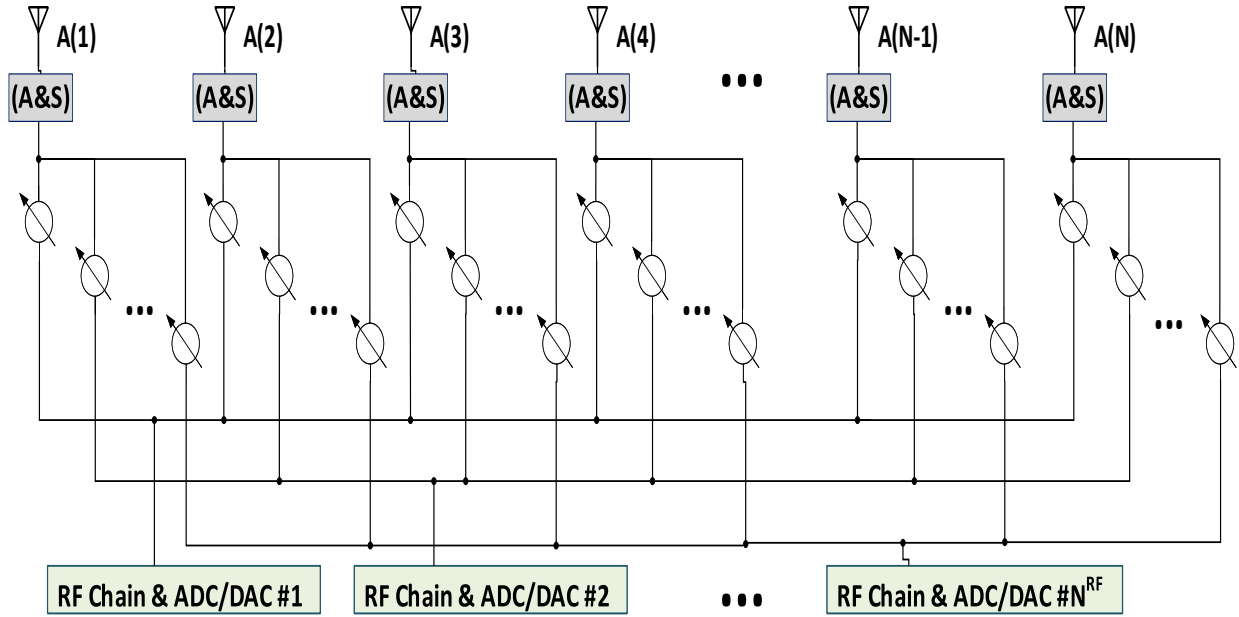
Figure 2.2: Traditional hybrid MIMO architecture (TA).

- The performance of the LAS architecture is investigated within varying scattering environments to demonstrate its capabilities over SLA.

Section II describes the LAS architecture, wireless channel model, and system model. Section III demonstrates the performance of LAS architecture. Specifically by considering a mmWave propagation channel which consist of 6 clusters with 8 rays per cluster, it is shown that a mmWave system employing LAS architecture in its transmitter and receiver can operate with $2\times$ energy efficiency and 98% spectrum efficiency as compared to usage of TA.

Throughout this chapter, matrices are denoted by bold uppercase letters (e.g. A), and vectors are denoted by bold lowercase letters (e.g. a). A^H and a^T denote the Hermitian (conjugate transpose) of matrix A and regular transpose operation of a, respectively.

2.1 System Model

2.1.1 Lens Antenna Subarray (LAS)

Dividing a large phased antenna array into subarrays for reducing the total number of phase shifters and simplifying the back-end electronics is a well-recognized concept [36]. In this case, array factor (AF) of the antenna can be written as $AF = AF_p AF_s$, where AF_p and AF_s stand for the primary and secondary AFs corresponding to the subarray and array of subarrays, respectively. The absence of phase shifters causes AF_p to lose its electronic beam-steering capability, while AF_s exhibits grating lobes due to the large spacing among the subarrays. Consequently, for large scan angles, grating lobes of AF_s enter into the visible range and cause a limited scan range with large side lobe levels (SLLs). Overlapping and interlacing subarrays improves scan range and SLL [36, 45]. However, these techniques still underperform in comparison to the traditional phased arrays. Additionally, these techniques present implementation challenges. For example, overlapping requires smaller inter-element spacing and multiple RF crossings in the feed network – not easily scalable to mmWaves. Amplitude control and randomization of subarray antenna grouping are promising to enhance performance [46], but scan range is still well below the traditional phased array. Importantly, amplitude control is performed with variable gain amplifiers – implying significant power consumption for massive MIMO arrays [47].

LAS architecture places microwave lenses over the subarrays. Antenna elements of the subarray are located in the focal plane of the lens. Consequently, each antenna within the subarray becomes associated with a beam pointed towards a different angular direction. The LAS architecture therefore necessitates to include a switch network per a subarray as well to perform antenna selection based on desired angular beam direction. These architectural modifications allows AF_p to gain its electronic beam-steering capability. Hence, $AF_p AF_s$ can perform without issues of grating lobes when AF_p and AF_s are properly steered through the switch network and phase shifter included

under each lens. Due to AF_p gaining electronic beam-steering capability, LAS based antenna offers a large scan range as compared to other subarray techniques. The LAS architecture is flexible for making trade-offs between the total number of switches and phase shifters by adjusting the number of antennas placed under each lens (L).

LAS architecture is presented in Fig. 2.1. In a particular LAS architecture example, the variables were selected as N = 20 antenna elements, L = 5 lenses, $M = N/L = 4$, $N^{RF} = 1$ and radiation performance was investigated [43]. This was a 1D linear array implementation of the LAS architecture. It was designed with the objectives of meeting the radiation efficiency and aperture efficiency (i.e. half-power beamwidth (HPBW)) performance of a traditional N = 20 element $\lambda/2$ spaced 1D linear phased antenna array (i.e. > 15 dBi gain, and 80% radiation efficiency based on full wave simulation of traditional array). These objectives were met with an SLL below 9 dB and scan range of $\pm 37.5°$. In [48], this concept was extended to 2D beam steering by using extended hemispherical dielectric lenses with variables selected as N = 119 antenna elements, L = 7 lenses, $M = N/L = 17$, and $N^{RF} = 1$. The antenna operated with 19.8 dBi gain, $10°$ degree HPBW, SLL below -9.7 dB, and a scan range approaching $\pm 45°$. As shown in the table provided in [48], LAS architecture significantly enhances the scan range over other subarrays.

Typically, TAs operate with scan ranges of $\pm 45°$ and can approach to $\pm 60°$ with careful design considerations (such as suppression of surface waves). As a new architecture, LAS architecture may have potential to match this scan range in future and has already demonstrated $\approx \pm 45°$. Therefore, in the system analysis, scan range of TA and LAS architectures will be treated as equal to each other as $\pm 45°$.

Uniform TAs operate with -13 dB SLL. LAS architecture is already shown to provide ≈ -10 dB SLL in recent publications [43, 48]. In addition, antenna gain obtained from LAS architecture is shown to be comparable to that of the TA. Due to the low level of SLL and on-going research in the design of LAS architectures towards improving performance, system analysis will treat the SLL level of LAS to be equal of TA for simplicity. Under equal SLL, equal scan range, and equal HPBW assumption, the radiated beam from a LAS architecture consisting of M antennas

will be equal to the beam radiated by M element half-wavelength spaced TA. Therefore, in the system analysis, the LAS can be replaced with a M element TA with beam steering vector of

$$\mathbf{A}^m = [e^{-j\pi M\sin(\theta_m)}, e^{-j\pi(M-1)\sin(\theta_m)}, \ldots, e^{j\pi M\sin(\theta_m)}]^T, \tag{2.1}$$

where $\theta_m = \pi/4 - (m-1)\pi/2/(M-1)$ is the direction of the radiating beam from LAS while $m = 1, 2, \ldots M$ indicates the antenna selected with the switch network. Radiated beam directions from the LAS architecture takes discrete values due to the discrete number of antenna elements. Location of these elements are designed to generate beams with equal θ spacing.

2.1.2   System Model

We assume that the LAS architecture shown in Fig. 2.1 is used in a single-user mmWave system. The transmitter with N_t antennas, L_t lenses, N_t^{RF} chains transmits N_s data streams to the receiver with N_r antennas, L_r lenses, N_r^{RF} chains where $N_s \leq N_t^{RF} \leq N_t$ and $N_s \leq N_r^{RF} \leq N_r$. Based on hybrid beamforming equations given in [31], and considering narrowband frequency-flat channel model, the received signal can be given as

$$\mathbf{r} = \sqrt{\rho}\mathbf{HFs} + \mathbf{n} \tag{2.2}$$

where $\mathbf{r}$ is the $N_r \times 1$ received signal vector, $\mathbf{H}$ is the $N_r \times N_t$ channel matrix, $\mathbf{F}$ is the $N_t \times N_s$ precoder matrix, $\mathbf{s}$ is the $N_s \times 1$ transmitted data, ρ is average received power and $\mathbf{n}$ is the vector of independent and identically distributed complex $N(0, \sigma_n)$ noise.

The high propagation loss characteristics of mmWave channel causes limited scattering in the environment. Therefore, narrowband clustered channel model is more accurate for mmWave systems [15, 49–51]. Using the clustered channel model, channel matrix $\mathbf{H}$ can be expressed as summation of scattering components which consist of N_{cl} number of clusters and N_{ray} number of

rays in each cluster. Considering that, the channel matrix $\mathbf{H}$ can be written as

$$\mathbf{H} = \sqrt{\frac{N_t N_r}{N_{cl} N_{ray}}} \sum_{i=1}^{N_{cl}} \sum_{k=1}^{N_{ray}} \alpha_{i,k} \mathbf{a}_r(\phi_{i,k}) \mathbf{a}_t^H(\theta_{i,k}), \tag{2.3}$$

where $\alpha_{i,k}$ is the complex gain of the kth ray in the ith cluster, $\mathbf{a}_t(\theta_{i,k})$ is the transmit antenna array response vector which is evaluated for $\theta_{i,k}$ departure angle of kth ray in the ith cluster, $\mathbf{a}_r(\phi_{i,k})$ is the receiver antenna array response vector which is evaluated for $\phi_{i,k}$ arrival angle of kth ray in the ith cluster. The N element array vector for TAs can be expressed as

$$\mathbf{a}(\theta_{i,k}) = \begin{bmatrix} 1 & \cdots & e^{-j2\pi n\sin(\theta)} & \cdots & e^{-j2\pi(N-1)\sin(\theta)} \end{bmatrix}^T. \tag{2.4}$$

Since the receiver implements a hybrid combiner $\mathbf{W}$ to the received signal, the processed received signal vector can be written as

$$\mathbf{y} = \sqrt{\rho} \mathbf{W}^H \mathbf{H} \mathbf{F} \mathbf{s} + \mathbf{W}^H \mathbf{n} \tag{2.5}$$

where $\mathbf{W}$ is the $N_r \times N_s$ receiver combining matrix. Considering $\mathbf{F}_{Lens}$ transmitter lens effect and hybrid precoding matrices, the precoding matrix $\mathbf{F}$ can be expanded as

$$\mathbf{F} = \mathbf{F}_{Lens}^{\mathbf{m}_t} \mathbf{F}_{RF} \mathbf{F}_{BB}, \tag{2.6}$$

where $\mathbf{m}_t$ represents $1 \times L_t$ vector of selected antenna indexes under each lens at the transmitter, $\mathbf{F}_{Lens}^{\mathbf{m}_t}$ is the $N_t \times L_t$ lens antenna effect, $\mathbf{F}_{RF}$ is the $L_t \times N_t^{RF}$ RF precoder using phase shifters at the transmitter, and $\mathbf{F}_{BB}$ is the $N_t^{RF} \times N_s$ digital precoder. Each column of $\mathbf{F}_{Lens}^{\mathbf{m}_t}$ matrix consist of zeros and $\mathbf{A}^m$. It can be expressed as

$$\mathbf{F}_{Lens}^{\mathbf{m}_t} = \begin{bmatrix} \mathbf{A}^{\mathbf{m}_t(1)} & \mathbf{0}_{Mx1} & \cdots & \mathbf{0}_{Mx1} \\ \mathbf{0}_{Mx1} & \mathbf{A}^{\mathbf{m}_t(2)} & \mathbf{0}_{Mx1} & \\ \vdots & & \ddots & \\ \mathbf{0}_{Mx1} & \cdots & \mathbf{0}_{Mx1} & \mathbf{A}^{\mathbf{m}_t(L_t)} \end{bmatrix}_{N_t x L_t}. \tag{2.7}$$

The zeros in the matrix indicates that there is no contribution between subarrays to their individual beams that they generate. For a clear understanding of $\mathbf{F}_{Lens}^{\mathbf{m}_t}$ an example matrix with $M = 3$, $L = 2$, and $N = ML = 6$ can be given as

$$\mathbf{F}_{Lens}^{\mathbf{m}_t} = \begin{bmatrix} e^{j\pi M \sin(-\pi/4)} & 0 \\ 1 & 0 \\ e^{-j\pi M \sin(-\pi/4)} & 0 \\ 0 & 1 \\ 0 & 1 \\ 0 & 1 \end{bmatrix} \tag{2.8}$$

where $\mathbf{m}_t$ is selected as $[3, 2]$ which means that first LAS is excited by the 3rd antenna element radiating towards $\theta_3 = -\pi/4$ while second LAS is excited by the 2nd antenna element radiating towards $\theta_2 = 0$. Similarly, the combining matrix $\mathbf{W}$ can be written as

$$\mathbf{W} = \mathbf{W}_{Lens}^{\mathbf{m}_r} \mathbf{W}_{RF} \mathbf{W}_{BB}, \tag{2.9}$$

where $\mathbf{m}_r$ represents vector of selected antenna indexes under each lens at the receiver, and $\mathbf{W}^{\mathbf{m}_r}_{Lens}$ is the $N_r \times L_r$ lens antenna effect, $\mathbf{W}_{RF}$ is the $L_r \times N_r^{RF}$ RF combiner using phase shifters at the receiver, and $\mathbf{W}_{BB}$ is the $N_r^{RF} \times N_s$ digital domain combining matrix. $\mathbf{W}^{\mathbf{m}_r}_{Lens}$ matrix can also be formed similarly to $\mathbf{F}^{\mathbf{m}_t}_{Lens}$ matrix by replacing transmitter domain variables with receiver domain variables.

Equation (2.5) represents all the antenna, RF processing, and digital processing of the system consisting of LAS architecture. Using this equation, the link throughput of the system can be calculated similarly to [31] as

$$R = \log_2 \left(\mathbf{I}_N s + \frac{\rho}{N_s} \mathbf{R}_n^{-1} \mathbf{W}^H \mathbf{H} \mathbf{F} \mathbf{F}^* \mathbf{H}^* \mathbf{W} \right). \tag{2.10}$$

where $\mathbf{I}_N$ is $N_s \times N_s$ identity matrix, $\mathbf{R}_n = \sigma^2 \mathbf{W}^H \mathbf{W}$ is the noise covariance matrix after combining. However, finding an optimal precoding and combining matrices of $\{\mathbf{F}^{\mathbf{m}_t}_{Lens}, \mathbf{F}_{RF}, \mathbf{F}_{BB}, \mathbf{W}^{m_r}_{Lens}, \mathbf{W}_{RF}, \mathbf{W}_{BB}\}$ is unlikely due to the non-convex constrains on $\{\mathbf{F}^{\mathbf{m}_t}_{Lens}, \mathbf{F}_{RF}, \mathbf{W}^{m_r}_{Lens}, \mathbf{W}_{RF}\}$. Thus, to show the performance of proposed LAS concept, exhaustive search has been implemented during performance analysis to find efficient precoding and combining matrices.

2.2 Performance Analysis

In this section, we first provide a power consumption model for TA and LAS architecture. Subsequently, we investigate spectrum efficiency of these architectures with the system model presented in previous section. Finally, we evaluate the energy efficiency using the ratio of spectrum efficiency and power consumption.

2.2.1 Power Consumption

Power consumption in traditional and alternative hybrid MIMO architectures has been investigated [33, 52] by considering the number of total hardware components (e.g. phase shifters, switches) and typical power consumption expected from these components. Reference [33] also presents a survey of hardware components developed for 60 GHz band applications. A wide range of power consumption values are typically observed and power consumption of particular hardware is selected based on certain justifications such as average value and expected trend in future years. We take a similar approach at the component level to evaluate and compare the power consumption of the LAS architecture and TA. First, these architectures are compared by assuming a single RF chain and ADC/DAC, i.e. architectures in Fig. 2.1 with $N^{RF} = 1$. We set the desired effective isotropic radiated power (EIRP) to 45 dBm based on existing/expected standards. We calculate the peak broadside gain of the traditional linear antenna array (G_{TA}) by assuming a 90% aperture efficiency (η_{TA}) as

$$G_{TA} = (4\pi/\lambda^2)A_p\eta_{TA}, \tag{2.11}$$

where A_p stands for the footprint area. A_p is linearly proportional to the element number N and element spacing d that is taken as $d = \lambda/2$ with λ representing the free space wavelength. The aperture efficiency of extended hemispherical or slab dielectric lenses used in [43, 48] can be as high as patch antenna arrays when compared with respect to the "footprint of lens base (= A_p)". Due to the lens/air mismatch and attractiveness of using low-cost (but with slightly higher loss) materials such as Acrynolitrile Butadiene Styrene (ABS) in 3D printing, aperture efficiency of LAS (η_{LAS}) is set to 80% and its gain is evaluated as

$$G_{LAS} = (4\pi/\lambda^2)A_p\eta_{LAS}. \tag{2.12}$$

To be similar with the antenna presented in [43], we set frequency to 38 GHz and take physical aperture area as $A_p = (N * 4) * 4$ mm^2, where 4 mm is a rounded value for the half of the free space wavelength $\lambda = 7.8947$ mm.

To achieve the desired EIRP (given in dBm), the total RF power that must be transmitted from the antenna elements can be expressed as

$$P_{T_x}^{TA} = 10^{0.1\text{EIRP}}/G_{TA} \qquad (2.13)$$

$$P_{T_x}^{LAS} = 10^{0.1\text{EIRP}}/G_{LAS} \qquad (2.14)$$

For the TA architecture consisting of single RF chain ($N^{RF} = 1$), the number of phase shifters is equal to the total number of antenna elements (i.e. $N_{PS} = N$). By representing the efficiency of the transmit amplifier with η_{PA}, DC power consumption of a phase shifter with P_{PS} and DC power consumption of an RF chain connected to ADC/DAC with P_C, the expression for the DC power consumption of TA becomes

$$P_{TA_t} = P_{T_x}^{TA}/\eta_{PA} + N P_{PS} + P_C. \qquad (2.15)$$

In this equation, the insertion loss (IL) of N-way power dividers within the architecture is not modeled as in [33]. LAS architecture can potentially provide further advantage in this perspective since switches also perform power division. Phase shifters are in general implemented as active or passive devices. Passive phase shifters exhibit negligible power consumption, however, they are in need of amplifier to compensate for their high losses.

For the LAS architecture consisting of single RF chain ($N^{RF} = 1$), equation (2.15) must be modified to account for IL and DC power consumption of the switch network. The switch network performs single pole multiple throw functionality. It can be implemented in various ways depending on choice of M in architecture. Here, we consider using SP2T, SP4T, and SP8T switches for $M = 4, 8$, and 16. We assume the switch network's loss as $IL_{SW} = \ell * 1$ dB,
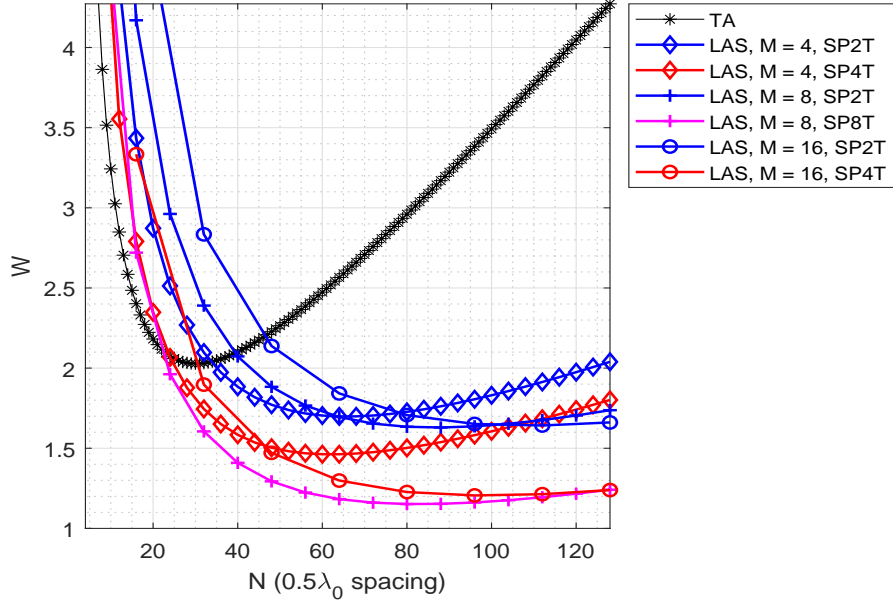
Figure 2.3: Power consumption of Lens Antenna Subarray (LAS) and Traditional (TA) hybrid MIMO architectures with single RF chain.

where ℓ stands for the number of switches in series within the network. The IL introduced by the SP2T implementations will be higher due to the need for using multiple switches in series. For example, SP4T and SP8T switch functionalities can be implemented with a total of $N_{SW} = 3$ and $N_{SW} = 7$ SP2T switches, IL_{SW} of 2 dB and 3 dB, since $\ell = 2$ and $\ell = 3$ for these implementations, respectively. Accounting for the switches, the DC power consumption of the LAS architecture becomes

$$P_{LAS_t} = \frac{P_{T_x}^{LAS}}{\eta_{PA}\eta_{SW}} + LP_{PS} + LN_{SW}P_{SW} + P_C. \tag{2.16}$$

where $\eta_{SW} = 10^{(-IL_{SW}/10)}$ stands for the efficiency of the switch network and P_{SW} represents the DC power consumption of the switch. The curves shown in Fig. 2.3 are generated with $\eta_{PA} = 0.2$, $P_{PS} = 30$ mW, and $P_C = 220mW$. As in [33, 53], P_C is taken significantly higher than P_{PS}. P_{PS} is based on commercially available phase shifters. P_{SW} is taken significantly lower as $P_{SP2T} = 10$ mW. For power consumption of larger throw switches, we use $P_{SP4T} = 20$ mW and $P_{SP8T} = 40$ mW. Fig. 2.3 demonstrates that for small arrays with $N < 30$, the efficiency of amplifiers dominate the power consumption. However, for larger arrays, power consumption in control components is

the dominant contributor and larger lenses with more multiple throw switches offer better power savings. Different power consumption assumptions for the components produces similar trends demonstrating that large antenna arrays will benefit from the LAS architecture in terms of total power consumption.

Equations (2.15) and (2.16) can be generalized to multiple RF chains as

$$P_{TA_t}^{N^{RF}} = \frac{P_{T_x}^{TA}}{\eta_{PA}} + N^{RF} N P_{PS} + N^{RF} P_C, \tag{2.17}$$

$$\begin{aligned} P_{LAS_t}^{N^{RF}} = \; & P_{T_x}^{LAS}/(\eta_{PA}\eta_{SW}) + N^{RF} L P_{PS} \\ & + N^{RF} L N_{SW} P_{SW} + N^{RF} P_C. \end{aligned} \tag{2.18}$$

Fig. 2.4 depicts that the TA power consumption becomes heavily dominated by the phase shifters with increasing N^{RF}. For instance, for $N = 64$ the power consumption for $N^{RF} = 4$ and $N^{RF} = 8$ TA are 9 W and 18 W, respectively. Significant power savings can be achieved by the LAS architecture even in small array settings. For example, the power consumption ratio between TA and LAS architecture is $> 2 : 1$ for $N = 64$ and $N^{RF} = 8$ when LAS architecture is implemented with $M = 16$ elements per lens, $L = N/M = 4$ lenses and SP4T switches.

Receiving architectures will employ low noise amplifiers (LNAs) at the antenna elements. Therefore, the power consumption model can be expressed by replacing transmitted RF power related quantities in equations (2.17) and (2.18) with LNA power consumption P_{LNA} as

$$P_{TA_r}^{N^{RF}} = N P_{LNA} + N^{RF} N P_{PS} + N^{RF} P_C, \tag{2.19}$$

$$\begin{aligned} P_{LAS_r}^{N^{RF}} = \; & N P_{LNA} + N^{RF} L P_{PS} \\ & + N^{RF} L N_{SW} P_{SW} + N^{RF} P_C. \end{aligned} \tag{2.20}$$

Fig. 2.5 shows $P_{TA_r}^{N^{RF}}$ and $P_{LAS_r}^{N^{RF}}$ as a function of N and N^{RF} with $P_{LNA} = 20$ mW [33]. It is observed that for multiple RF chains, the LAS architecture again presents significant reduction in power consumption.

26
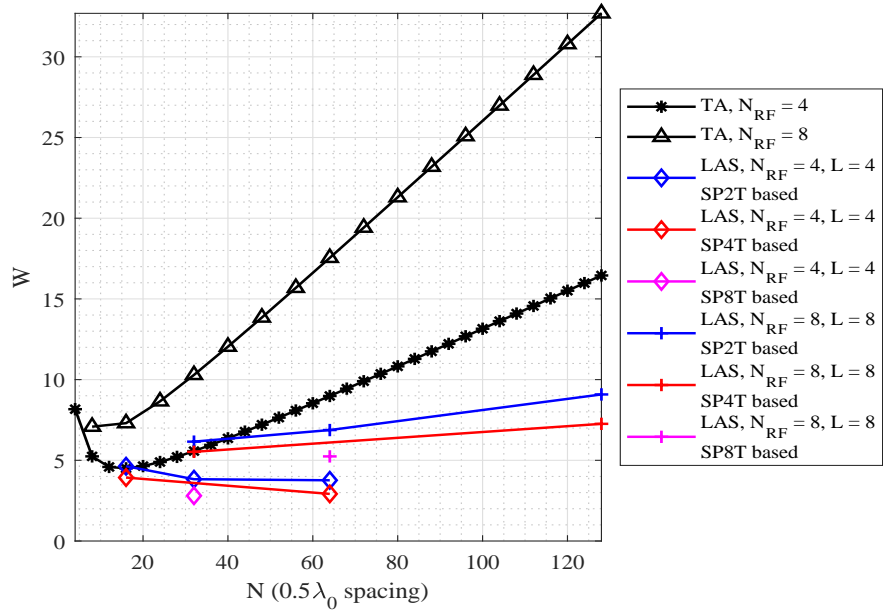
Figure 2.4: Power consumption of LAS and TA architectures with multiple RF chains ($N^{RF} \neq 1$).
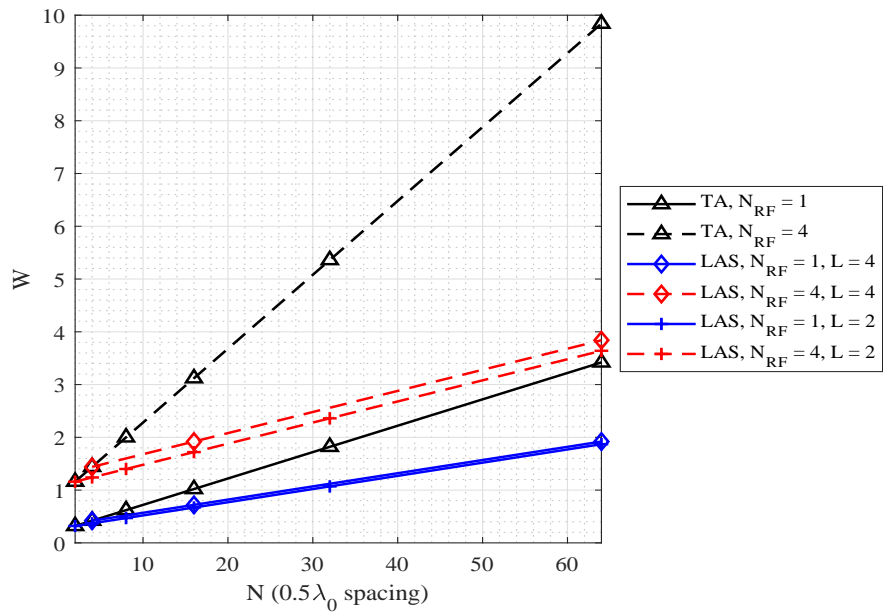
Figure 2.5: Power consumption of LAS and TA architectures when they are in receiving mode.
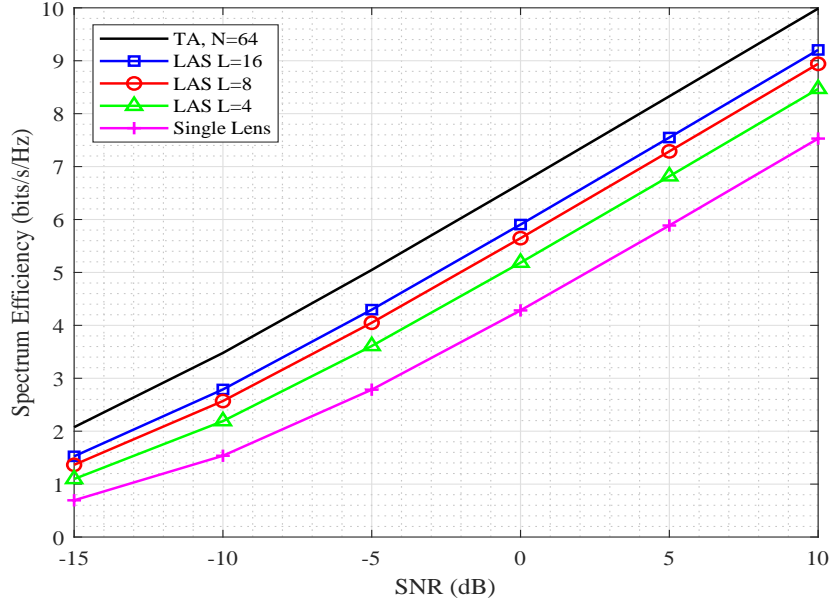
Figure 2.6: Spectrum efficiency of LAS and TA architectures with single RF chain when receiver is equipped with omni-directional antenna.

2.2.2 Spectrum and Energy Efficiency

To evaluate the performance of the TA and LAS architecture, a scattering propagation channel is assumed. The propagation environment is modeled consisting of $N_{cl} = 6$ clusters with $N_{ray} = 8$ rays per cluster which are distributed on azimuth angles with Laplacian distribution as already utilized to model mmWave wireless communications in [49, 50]. For simplicity, all the clusters are assumed to have equal powers. The angular spread at both transmitter and receiver are distributed with the same variance. The channel is assumed to be known. The channel estimation can be performed with similar approaches presented in [33,54,55], but LAS may potentially benefit from a different channel estimation approach and this is beyond the scope of this manuscript. SNR is calculated as SNR $= \rho/\sigma_n^2$. Finally, all the reported results are averaged over 500 random channel realizations.
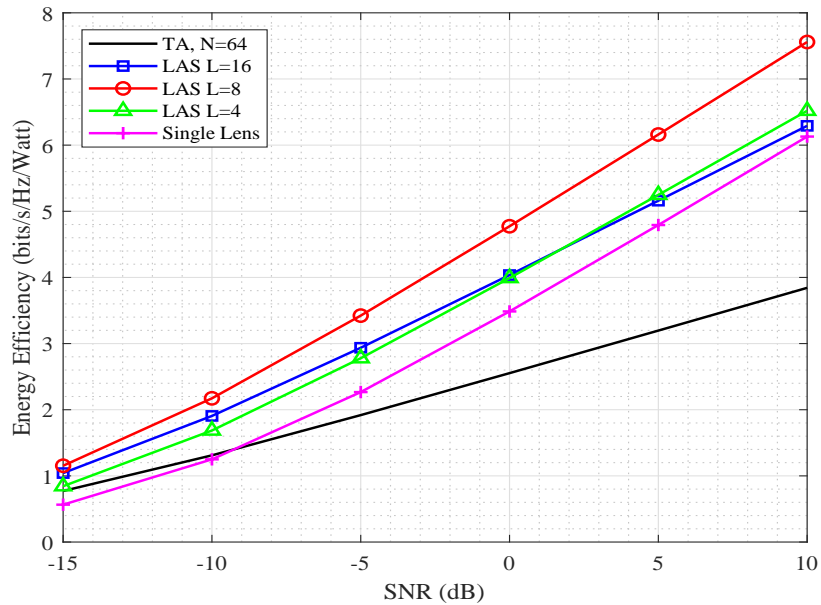
Figure 2.7: Energy efficiency of LAS and TA architectures with single RF chain when receiver is equipped with omni-directional antenna.

Fig. 2.6 and Fig. 2.7 show the spectrum and energy efficiency performances for $N^{RF} = 1$ scenario employing a transmitter consisting of $N_t = 64$ antenna elements while the receiver is equipped with an omni-directional antenna. When compared to SLA ($L = 1$), which can be referred as conventional beamspace MIMO, the LAS architecture provides increased spectrum efficiency. Specifically, the spectrum efficiency is improved by 15%, 24%, and 28% for $L = 4$, $L = 8$, and $L = 16$, respectively at SNR = 5dB. Due to its reduced precoding capability, the LAS architecture cannot reach to the spectrum efficiency performance of the TA which improves by 41% as compared to the SLA. However, these values still implies that spectrum efficiency of the LAS architecture is within 91% of TA for $L = 16$. Despite this minimal penalty in spectrum efficiency, the LAS architecture outperforms all other architectures in energy efficiency as seen in Fig. 2.7. Specifically, the energy efficiency of the LAS architecture is 161% of the TA for $L = 16$. It is important to note that the best energy efficient architecture in Fig. 2.7 is with $L = 8$ with 194% of the TA, showing the importance of making a careful trade-off between precoding gain and and power consumption in the LAS architecture design.
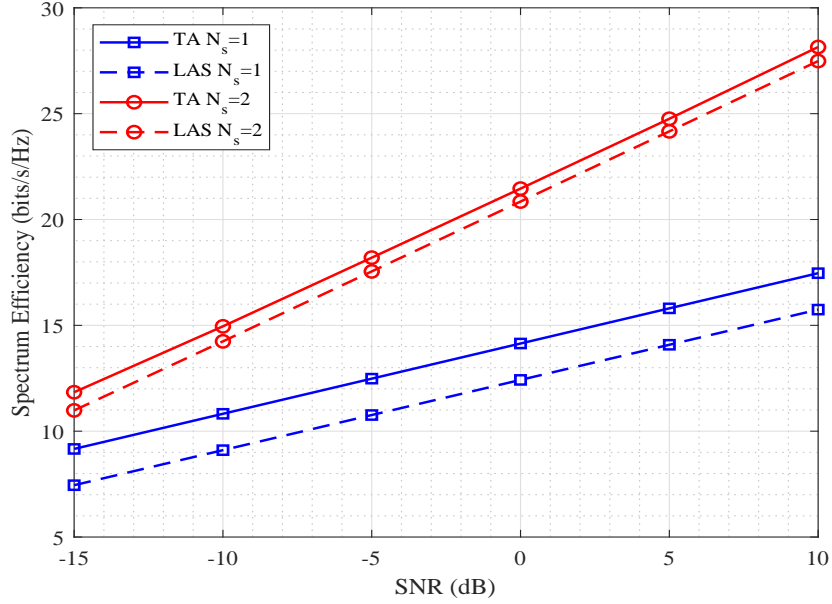
Figure 2.8: Spectrum efficiency of LAS and TA architectures with multiple RF chains and data streams. For LAS modeling, both transmitter and receiver are equipped with LAS.

Fig. 2.8 and Fig. 2.9 show the spectrum and energy efficiency performances for multiple RF chain scenarios. Transmitter is assumed to employ $N_t = 64$ antenna elements, and $L_t = 16$ lenses with $N_t^{RF} = 8$ RF chains. Receiver is assumed to be equipped with $N_r = 16$ antenna elements, $L_r = 4$ lenses, and $N_r^{RF} = 4$ RF chains. The system is evaluated for 1 and 2 simultaneous streaming data cases to evaluate multiplexing effects as well. As seen in Fig. 2.8, the LAS architecture performs within 89% and 98% of the spectrum efficiency of the TA for 1 and 2 streaming data cases, respectively. Based on Fig. 2.9, energy efficiency of the LAS architecture is significantly better than the TA. Specifically, energy efficiency of the LAS architecture is 181% and 198% of that of the TA.

Fig. 2.10 and Fig. 2.11 show the performance under different scattering channel scenarios when $N^{RF} = 1$. A rich scattering channel is implemented with $N_{cl} = 12$ clusters and $N_{ray} = 16$ rays per cluster, while a poor scattering channel is implemented as $N_{cl} = 2$ clusters and $N_{ray} = 2$ rays per cluster. These selections can be interpreted as if the rich channel has 192 and the poor channel has 4 scatterers, respectively. As seen in Fig. 2.10 the LAS architecture performs better in a poor
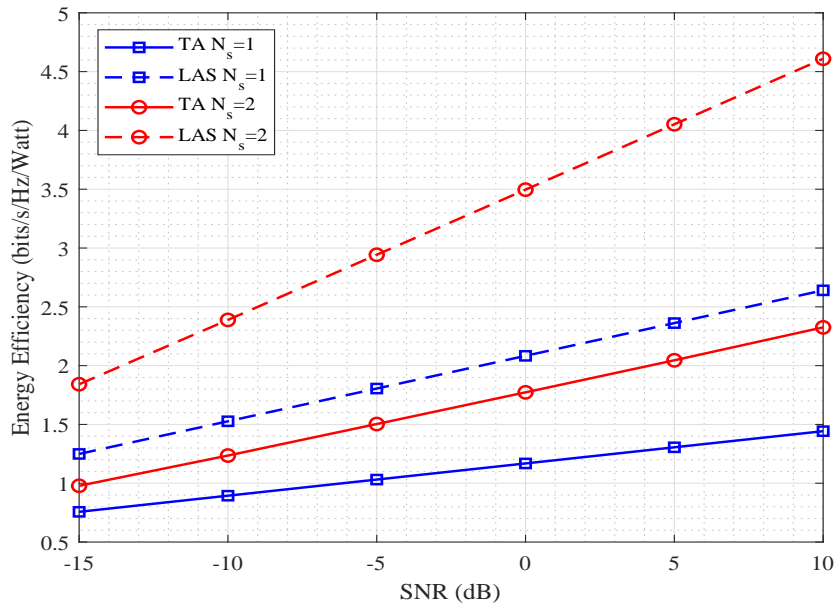
Figure 2.9: Energy efficiency of LAS and TA architectures with multiple RF chains and data streams. For LAS modeling, both transmitter and receiver are equipped with LAS.

scattering environment as compared to a rich scattering environment. Its performance gets even closer to the TA in poor scattering channel conditions. This observation is also true for the SLA. However, both LAS architecture and TA outperforms the SLA in rich and poor scattering channels. Most importantly, it is observed that SLA suffers the most in a rich scattering environment, while the LAS architecture still can perform close to a TA within 90% of spectrum efficiency for $L = 16$. Fig. 2.10 also shows that the LAS architecture slightly performs worse in a rich scattering channel as compared to poor scattering channel. This is related to the limited precoding capability of the architecture as compared to TA. When the signal arrives from too many multipath directions, the LAS architecture will not be able to adapt the antenna gain pattern as flexibly as TA can do. The pattern created by an antenna group (i.e. M elements) behind a lens cannot be optimized by changing antenna coefficients. Only the pattern direction can be changed by selecting the antenna element exciting the lens. Due to this reason, the SLA suffers most as it does not exhibit any precoding capability since all antenna elements are behind the lens with no capability of pattern optimization by changing antenna coefficients.

31
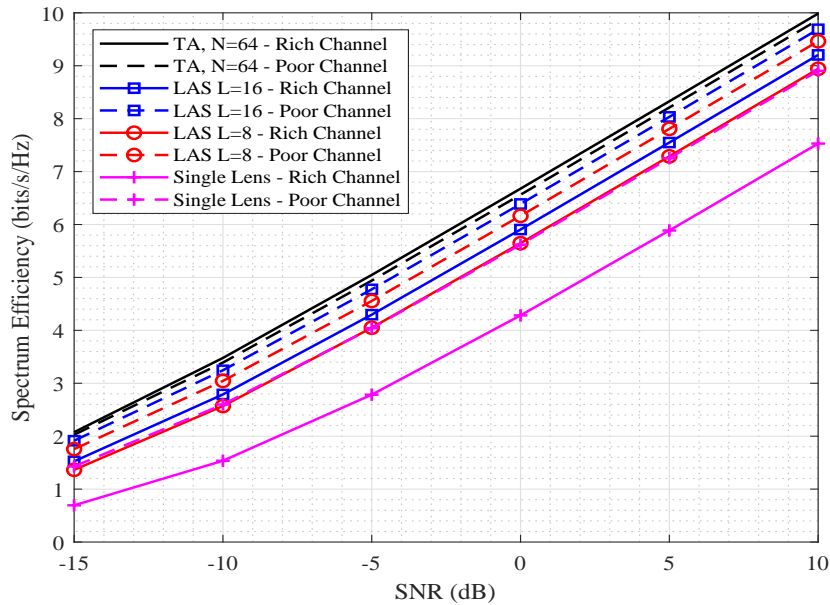
Figure 2.10: Spectrum efficiency of LAS and TA architectures for rich and poor channel scaterring scenarios when receiver is equipped with omni-directional antenna.

Fig. 2.11 shows that the energy efficiency of the LAS architecture again outperforms the TA approach by about 100% in rich or poor scattering channel conditions. This is again due to the close spectrum efficiency between the two architectures, but significantly reduced power consumption in the LAS architecture. Finally, Table 2.1 presents the summary of the observations that has been made during the performance evaluation of the LAS architecture throughout this manuscript.

2.3 Conclusion

Spectrum and energy efficiencies of mmWave wireless communication systems consisting of a new lens antenna subarray (LAS) based hybrid multiple input multiple output (MIMO) architecture were investigated. The LAS architecture was shown to provide improved energy efficiency while providing similar spectrum efficiency to the traditional hybrid MIMO architecture (TA). For example in a system with $N_s = 2$ data stream transmissions, employing LAS architecture at the transmitter ($N_t = 64$ antennas, $L_t = 16$ lenses, $N_t^{RF} = 8$ RF chains) and at the receiver ($N_r = 16$ antennas, $L_r = 4$ lenses, $N_r^{RF} = 4$ RF chains) provides 98% of the data rate that can be achieved
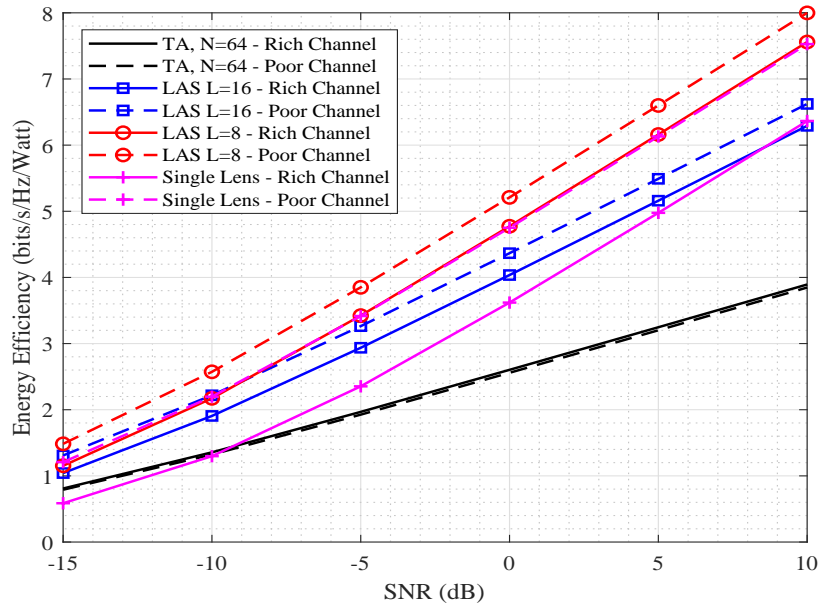
Figure 2.11: Energy efficiency of LAS and TA architectures for rich and poor channel scaterring scenarios when receiver is equipped with omni-directional antenna.

by the TA. On the other hand, in this scenario, the LAS architecture operates with 194% energy efficiency of the TA. As compared to single lens antenna array architecture (SLA), the LAS architecture provides significant advantages in data rate and energy efficiency particularly in scatttering channel conditions that will be observed in mmWave bands. The presented system model used exhaustive search for precoding/combiner matrices and channel estimation was not performed. Future work will consider LAS architecture specific channel estimation and precoder/combiner estimation algorithms to investigate the performance towards practical system implementations. Multi-user scenarios will also be investigated along with antenna hardware implementations.

Table 2.1: Performance comparison of LAS architecture with TA when SNR = 5 dB, see Section III.A for power consumption model and assumptions, $L_t = 8$ for $N_t^{RF} = 1$ and $L_t = 16$ for $N_t^{RF} = 8$.

(bits/s/Hz)	$N_t = 64$	**TA**	**SLA**	**LAS (This Work)**
Data Rate	$N_s = 1$ $N_t^{RF} = 1$	8.33	5.89 71% of TA	7.29 88% of TA
	$N_s = 2$ $N_t^{RF} = 8$	24.76	-	24.16 98% of TA
Energy Efficiency (per Watt)	$N_s = 1$ $N_t^{RF} = 1$	3.2	4.8 150% of TA	6.2 194% of TA
	$N_s = 2$ $N_t^{RF} = 8$	2.05	-	4.05 198% of TA
Poor Channel	$N_s = 1$ $N_t^{RF} = 1$	8.21	7.25 88% of TA	7.8 95% of TA
Rich Channel	$N_s = 1$ $N_t^{RF} = 1$	8.33	5.89 71% of TA	7.29 88% of TA

Chapter 3: Dynamic Sidelobe Multiplexing in Beamspace MIMO Systems[1]

The tremendous growth in communication systems has already filled up the traditional microwave spectrum. Still growing interest in data greedy wireless applications made the cellular industry to seek new frequencies for utilization of next-generation wireless technologies [2, 3]. mmWave communication becomes a promising technology to support wireless systems for larger bandwidth and higher data rates in 5G networks [4–6].

MIMO and mmWave integration has been estimated as one of the key technologies in 5G wireless communication systems to compensate for the severe path loss [57]. However, as each antenna element in MIMO systems requires one devoted radio frequency (RF) chain, the hardware complexity and energy consumption become excessive with large number of antenna elements [58]. Investigations in [37, 59] show that beamspace MIMO can provide an efficient solution for this problem. The implementation of electromagnetic lenses in beamspace MIMO, replaces phase shifters with switches which increases energy efficiency. The direction of the generated beam is controlled by switching between the antenna apertures placed on the focal plane of the lens. Beamforming with the lens antenna array is not only a cost-efficient solution but also achieves similar directivity gain with simplified hardware [38]. Thus, lens antennas show a promising future in mmWave systems [58]. [60, 61] present studies on beam tracking and beam selection for effective communication in beamspace MIMO. [62] provides a channel estimation scheme based on a reliable support detection which is proposed to overcome exhaustive overhead processing of the beamspace MIMO channel. According to these above-mentioned works [38, 60–62], the number of users/streams that can be supported at the same time-frequency resource is limited with the number of RF chains in conventional multiplexing of beamspace MIMO

---

[1]This chapter was published in [56]. Permission is included in Appendix A.
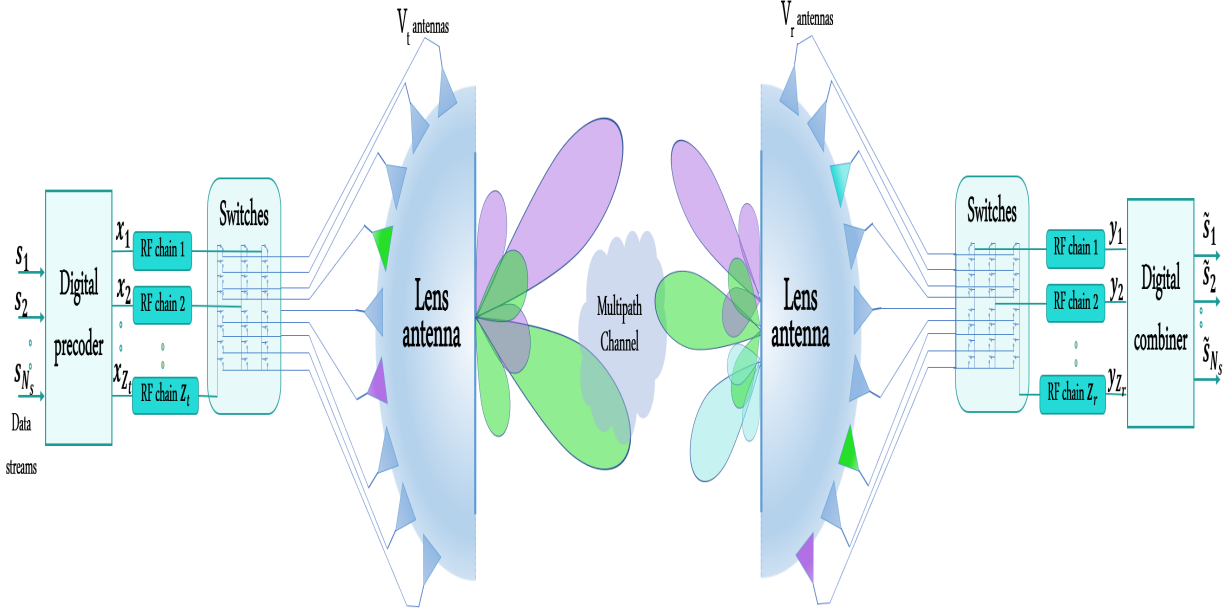
Figure 3.1: System model for beamspace MIMO architecture.

systems. To overcome this limitation, [63, 64] propose the concept of non-orthogonal multiple access (NOMA) with beamspace MIMO. Following this work, [65] presents power allocation method for beamspace MIMO-NOMA systems using sequential convex approximation with energy-efficiency goal. Similarly, [66] proposes user clustering for further enhancement in energy and spectrum efficiency, while a precoding technique is used inside each cluster to reduce the inter-user and inter-beam interferences. [67] introduces another NOMA variant which is called layered division multiplexing (LDM) to integrate mmWave MIMO system with full-duplex device-to-device communications in order to implement broadcast and unicast services. [68] indicates that clustering a few users on a single beam with small bandwidth to implement NOMA limits its potential on energy efficiency, and proposes a beam splitting scheme to serve more users located in different beam coverage.

Despite the advantages of the aforementioned studies, the conventional transmitter systems should provide at least the same number of transmitting beams and RF chains as the number of multipath streams [37, 38]. In order to relieve the system from this constrain, we propose a novel multiplexing method, called *Dynamic Sidelobe Multiplexing (DSM)*, that allows additional

36

data streams to be multiplexed and reconstructed. The main contribution of the proposed DSM method is to introduce additional receiver beams to open up new paths to receive the additional streams that is transmitted under the main signal. Due to multipath effects of the environment, the signal gathered on the additional beams are not only from main lobes of the transmitted beams but also from the sidelobes. Therefore, in the proposed DSM method, the Tx and Rx beams are dynamically selected to maximize the goal function, i.e. capacity and signal-to-interference-plus-noise-ratio (SINR). Compared to conventional beamspace MIMO, numerical results show that the DSM technique can provide more than 50% spectral efficiency enhancement at high SNR).

3.1   System Model

In this chapter, we consider a typical mmWave beamspace MIMO system with capability of establishing links through multiple beams. As illustrated in Fig. 3.1, the transmitter and receiver are equipped with lens antenna array (LAA) with V_t, V_r antenna elements, respectively. To represent multiple input and multiple output, the received noisy signal can be written in a matrix form as

$$\boldsymbol{y} = \boldsymbol{H}\boldsymbol{x} + \boldsymbol{n}, \tag{3.1}$$

where $\boldsymbol{x} = [x_1, x_2, \ldots, x_{Z_t}]^T$ is the transmitted signal vector over the beams while $(\cdot)^T$ denotes transposition. $\boldsymbol{n}$ is noise vector where each element is independent and has zero mean complex Gaussian distribution with covariance of σ_n. $\boldsymbol{H}$ is narrowband multipath geometrical channel matrix, and it is in [4] given as

$$\boldsymbol{H} = \sum_{i=1}^{P} g_i \boldsymbol{a}_r(\theta_{i,A}) \boldsymbol{a}_t^H(\theta_{i,D}), \tag{3.2}$$

where P is the number of resolvable channel paths, g_i is the complex channel coefficient on each ith path, θ_A is angle of arrival (AoA), and θ_D is angle of departure (AoD). $\boldsymbol{a}_t$ and $\boldsymbol{a}_r$ are the steering vector of the transmitter and receiver, respectively, where $(\cdot)^H$ denotes Hermitian transposition.

In the beamspace MIMO model, the LAA components as shown in Fig. 3.1, are located in the focal region of electromagnetic lens [38], and they follow the condition of

$$\sin(\phi) = \frac{v_j}{\overline{D_j}} \quad , \qquad v_j \in V_j, \tag{3.3}$$

where ϕ is the angle of antenna element relative to the x-axis, and v_j denotes the selected antenna index at transmitter/receiver $j \in \{t, r\}$ for $v_j = 1, 2, ..., V_j$. The column elements of the steering vector $\boldsymbol{a}_j$ can be given as

$$a_j(\theta_l) = \sqrt{(\overline{D_j})} \ \text{sinc}(v_j - \overline{D_j}\sin(\theta_l)), \quad v_j \in V_j, \tag{3.4}$$

where $\overline{D} = D/\lambda_c$ is the lens antenna dimension D normalized by carrier wavelength λ_c, and $l \in \{D, A\}$. Note that the number of antenna V depends on $\overline{D}$ such as $V = \lfloor 2\overline{D} \rfloor + 1$ where $\lfloor \cdot \rfloor$ is the floor function. The "sinc" function formula in (3.4) represents the angle-dependent energy focusing property of LAA as it has been shown in [38].

Using (3.4), the elements $h(v_r, v_t)$ of channel matrix $\boldsymbol{H}$ represent the channel coefficient from transmitting antenna $v_t \in V_t$ to receiving antenna $v_r \in V_r$ and can be given as

$$\begin{aligned} h(v_r, v_t) = \sum_{i=1}^{P} g_i \sqrt{(\overline{D_r}\overline{D_t})} \\ \times \ \text{sinc}(v_r - \overline{D_r}\sin(\theta_{i,A})) \\ \times \ \text{sinc}(v_t - \overline{D_t}\sin(\theta_{i,D})). \end{aligned} \tag{3.5}$$

Accordingly, the received signal on the mth antenna can be summed through active transmission antennas as

$$y_{m^{th}} = \sum_{v_t^{active}} y(v_t, v_r = m), \tag{3.6}$$

where

$$y(v_t, v_r) = x_{v_t} h_k(v_t, v_r) + n. \tag{3.7}$$

3.2 The Proposed DSM Method

In order to improve the spectral efficiency in beamspace MIMO systems, we propose a dynamic multiplexing algorithm using the sidelobe radiation on beam. The goal of the proposed DSM algorithm is to transmit more number of data streams (N_s) than the available RF chains (Z_t) at the transmitter ($N_s > Z_t$). In the algorithm, the transmitted data streams are processed based on an algorithm similar to power domain NOMA implementation. To be able to receive the transmitted data streams, the receiver should have same or greater number of RF chains than the streams ($Z_r \geqslant N_s$). Thus, a cost efficient transmitter (i.e. user equipment (UE)) can be able to transmit more data streams than its original capabilities to a more powerful receiver (i.e. base station (BS)).

To clearly explain the DSM method, it is assumed that the transmitter has two RF chains, while the receiver has three. The method can be easily applied to the systems with (Z_t, Z_r) RF chains by arranging them into groups, where each group has two transmitted RF chains and three received RF chains.

At the transmitter, three data streams s_1, s_2, s_3 precoded into two transmitted signals x_1, x_2 using the following equation

$$
\begin{aligned}
x_1 &= s_1\sqrt{\gamma_1} + s_3\sqrt{1 - \gamma_1}, \\
x_2 &= s_2\sqrt{\gamma_2} + s_3\sqrt{1 - \gamma_2},
\end{aligned}
\tag{3.8}
$$

where $\gamma \in (0, 1)$ defines power ratio between the data streams. Each signal is transmitted over an antenna aperture which defines a beam through a narrowband multipath geometrical channel as given in (3.2).

In order to receive the multiple data stream, the receiver is implemented to utilize same number of RF chains as the stream, which is three-RF chains in this particular example. While the first two chains are receiving y_{m_1} and y_{m_2} through matching Tx beams with Rx beams, the third chain receives y_{m_3} through a third receiver beam. Since the third beam does not have a matching beam at the transmitter, it is expected to receive power from sidelobes of the transmitter beams as well as main lobes due to multipath channel effects. The received signal at the receiver can be

39

expressed as

$$\begin{bmatrix} y_{m_1} \\ y_{m_2} \\ y_{m_3} \end{bmatrix} = \begin{bmatrix} h_{m_1,k_1} & h_{m_1,k_2} \\ h_{m_2,k_1} & h_{m_2,k_2} \\ h_{m_3,k_1} & h_{m_3,k_2} \end{bmatrix} \begin{bmatrix} x_1 \\ x_2 \end{bmatrix} + \begin{bmatrix} n_{m_1} \\ n_{m_2} \\ n_{m_3} \end{bmatrix}, \tag{3.9}$$

where $m \in V_r$ and $k \in V_t$ are the activated received and transmitted antenna indexes, respectfully. The channel coefficient between the selected antenna apertures can be easily defined using (3.5), as

$$h_{m,k} = h(v_r = m, v_t = k). \tag{3.10}$$

At the receiver, successive interference cancellation (SIC) is applied to ensure a minimum sum link capacity in the presence of the interference between the data streams, as well, improving the SINR for other signals [69, 70]. Assuming perfect channel estimation, the received first two signal y_{m_1} and y_{m_2} are demodulated under the interference of s_3 to get s_1 and s_2 data streams, respectively, as in

$$\begin{aligned} \tilde{s}_1 &= \text{demod}(y_{m_1}), \\ \tilde{s}_2 &= \text{demod}(y_{m_2}). \end{aligned} \tag{3.11}$$

Then, these demodulated data streams are used to remove interference from the third received signal y_{m_3} by subtracting them for the demodulation of s_3 as in

$$\tilde{s}_3 = \text{demod}(y_{m_3} - \tilde{s}_1 h_{m_3,k_1} \sqrt{\gamma_1} - \tilde{s}_2 h_{m_3,k_2} \sqrt{\gamma_2}). \tag{3.12}$$

Consequently, the capacity of each data stream depends on its SINR can be expressed as

$$R = \sum_{q=1}^{N_s} \log_2(1 + SINR_q), \tag{3.13}$$

where the SINR can be given as

$$\text{SINR}_q =$$

$$\begin{cases} \dfrac{\gamma_q |h_{m_q,k_q}|^2}{\sum_{b \neq q} \gamma_b |h(m_q,k_b)|^2 + \sum_b (1-\gamma_b)|h(m_q,k_b)|^2 + \sigma_n^2} \quad, \quad q \leq 2, \\[3mm] \dfrac{\sum_b (1-\gamma_b)|h(m_q,k_b)|^2}{\sigma_n^2} \quad\quad\quad\quad, \quad q > 2, \end{cases} \tag{3.14}$$

where $q \in \{1,2,3\}$ is the transmitted stream index, and $b \in \{1,2\}$ is transmitted signal index. In order to maximize the total capacity over all the streams, (3.13) can be optimized as

$$\gamma, m, k = \arg \max_{\gamma,m,k} R(\gamma, m, k), \tag{3.15}$$

where $\gamma = [\gamma_1, \gamma_2]$, $m = [m_1, m_2, m_3]$, and $k = [k_1, k_2]$.

Other than the capacity maximization given in (3.15), the parameters can be optimized to provide fair SINR over each stream. The fairness can be provided as

$$\gamma, m, k = \arg \max_{\gamma,m,k} \prod_{q=1}^{N_s} \text{SINR}_q(\gamma, m, k). \tag{3.16}$$

Joint maximization problems in (3.15) and (3.16) is a complex problem. In order to simplify this problem and follow a more practical approach, the transmitter beam indexes k and receiver beam indexes m can be selected to maximize received power for each stream by maximizing the channel gains as follow

$$\begin{aligned} \{m_1, k_1\} &= \arg \max_{m_1,k_1} |h_{m_1,k_1}|^2, \\ \{m_2, k_2\} &= \arg \max_{m_2,k_2} |h_{m_2,k_2}|^2, \\ m_3 &= \arg \max_{m_3} |h_{m_3,k_1}|^2 + |h_{m_3,k_2}|^2. \end{aligned} \tag{3.17}$$

Following the selection of k and m, γ can be optimized using (3.15) or (3.16).
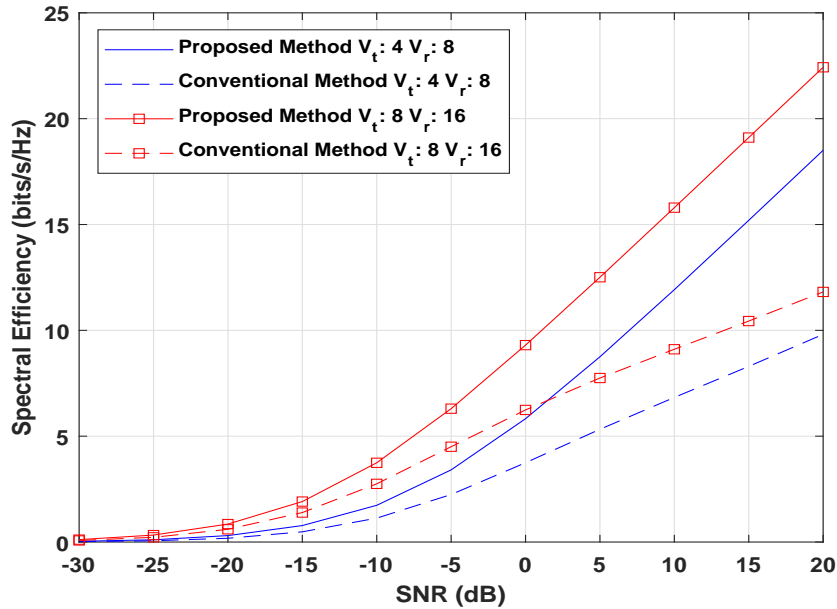
Figure 3.2: Spectral efficiency vs SNR with capacity optimization.

3.3 Numerical Results

In order to evaluate the performance of the proposed DSM method, Monte Carlo simulations have been performed. In the simulations, $Z_t = 2$, $Z_r = 3$, $V_t = 8$, and $V_r = 16$ are assumed. Two signals x_1 and x_2 are transmitted over a mmWave channel that is assumed to have $P = 48$ resolvable paths consists of randomly generated six multipath clusters and each cluster has randomly generated eight rays [4]. The dash lines in Fig. 3.2, Fig. 3.3, and Fig. 3.4 represent the conventional multiplexing method in mmWave beamspace MIMO system, refers to conventional method, while the solid lines represent the proposed DSM method, refers to proposed method.

In Fig. 3.2, the spectral efficiency results of proposed DSM method with capacity goal is presented. The results are compared with the conventional method in different antenna element sizes, i.e. $V_t = 8$, $V_r = 8$ and $V_t = 8$, $V_r = 16$ over different SNRs. Quantitatively, the proposed DSM method has about 50% enhancement over the conventional multiplexing method at $5\,dB$ SNR. The trend of this enhancement increases as the SNR increases in the system. Since the conventional method is affected by interference between beams, it converges towards a performance ceil. It is also noticed that increasing the antenna elements can improve the efficiency.

42
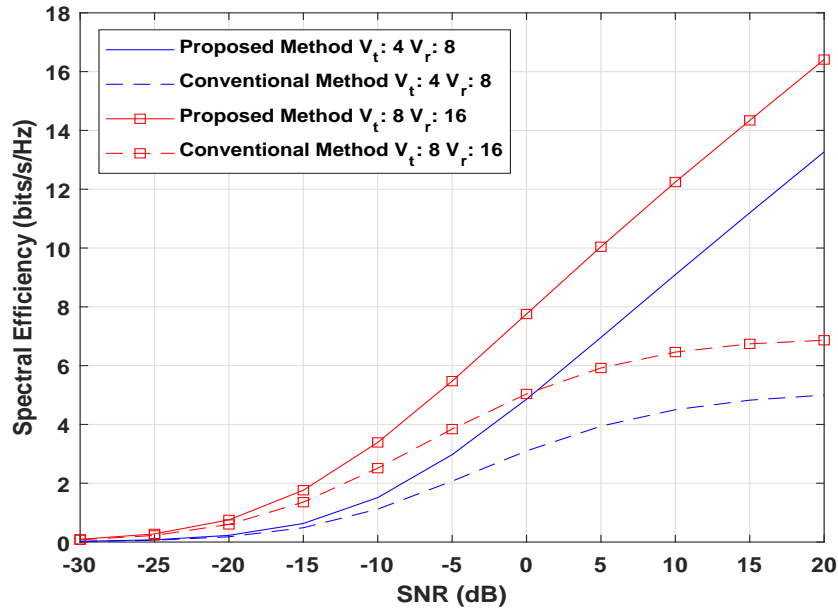
Figure 3.3: Spectral efficiency vs SNR with SINR optimization.

Similarly, Fig. 3.3 shows the spectral efficiency of the proposed DSM method compared to the conventional multiplexing method. However, this time the γ, m, k parameters are selected using (3.16). The figure clearly shows that despite the performance degradation the proposed algorithm can still double the spectral efficiency at high SNR. For example, at $10\ SNR$ value, the proposed DSM method achieved 12 and 9 bits/s/Hz efficiency for $V_t = 8, V_r = 8$ and $V_t = 8, V_r = 16$, respectively, while the conventional multiplexing method can provide around 4 and 6 bits/s/Hz efficiency.

The spectral efficiency versus SNR for individual data stream s_1, s_2, and s_3 is shown in Fig. 3.4 for $V_t = 4$ and $V_r = 8$. In the figure, each stream is represented with lines which are seperated by their mark and color. It can be noticed that with small degradation in the s_1 and s_2 data streams performance, s_3 gained a great enhancement on the spectral efficiency and resulted total performance to be improved.
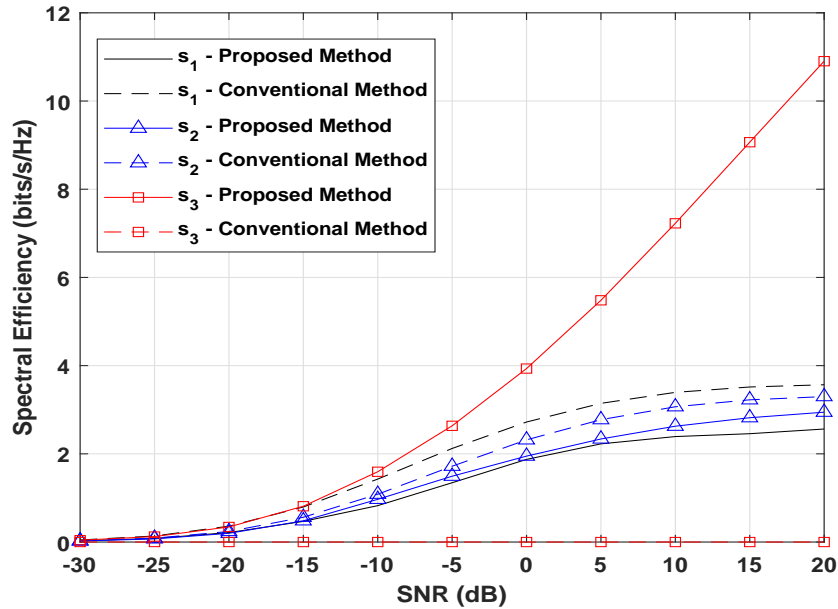
Figure 3.4: Spectral efficiency of each individual streams vs SNR for $V_t = 4$, $V_r = 8$.

3.4 Conclusion

In this chapter, a dynamic multiplexing approach has been proposed for the mmWave beamspace MIMO systems to break the restriction of the conventional multiplexing in mmWave beamspace MIMO scheme that can only serve one user/data-stream for each transmitted beam at the same time-frequency resources. In the proposed approach, the data is precoded at the transmitter to transmit over an insufficient number of beams while receiving a sufficient number of beams at the receiver. Such a method can be advantageous in systems where the transmitter needs to be low cost (i.e. UE) while the receiver can have more complex hardware (i.e. BS). Thus, considering UE and BS example, using the proposed method the communication network can provide higher speeds of uplink data or it can simply reuse the extra uplink resources for some other purpose.

Chapter 4: Joint Approach to Beam Optimization and User Association[2]

Tremendous growth on capabilities of mobile devices increased the variety of application and their requirements. In the past, only voice applications were available for mobile devices, the current trend has been advancing toward more innovative applications like high definition video conference, cloud computing/storage. The requirements of those applications, e.g. high data rate, low delay, drive wireless technology to become more efficient. Self-optimization methods for wireless communication networks, has been presented to continuously provide efficient system performance for varying conditions [72].

Load balancing is a self-optimization method to adapt serving area of cells to relieve heavily loaded cells. The desired effect on service area can be introduced by changing the transmission power, antenna parameters, or both [72]. Also, forced handover without any adaptation on the deployment parameters is a load balancing option. [73] presents antenna tilt adaptation for heterogeneous networks to relief the heavy load on hotspots. In the presented adaptation algorithm, each cell optimizes antenna tilt parameter individually to change service area. With the inspiration of bubble pressure dynamics, a bubble oscillation algorithm is proposed in [74] for load balancing. The pressure in the bubble is represented by the traffic, and the volume is seen as the coverage area of each cell. The authors suggest that by oscillating the bubbles, balance in the load can be achieved. However, in this approach, frequent changes on coverage increases handover rates and it may cause problems in the network. [75] proposes connection request blocking to direct users to

---

light loaded cells. In [76], a centralized scheduler for load balancing is presented. The scheduler receives the available channel measurements between user and each base station, and assigns a serving cell for each user to maximize capacity. Therefore, the serving cell might change for each scheduling period which requires heavy coordination between cells.

Studies in [77, 78] show that the optimum antenna parameters (antenna tilt and vertical beamwidth) change with the range of the cell. Therefore, individual optimization of antenna parameters for load balancing will also change effective range of neighboring cells. This necessitates joint optimization between cells for efficient system performance. [79] presents the importance of beam parameters and its effects on received. A joint optimization method for antenna tilt and horizontal beam parameters is presented in [80]. However, this method does not consider user-cell association as a parameter in the optimization process. The user-cell association plays an important role in load distribution of the network.

In this chapter, we present a method to optimize antenna parameters such as antenna tilt, vertical and horizontal beam width. Despite the conventional approaches the presented method optimize the goal function for target of joint optimal state/setting of antenna parameters and user-cell association. Using different goal functions, the approach can be targeted to maximize edge user performance, user fairness, total capacity, or other system targets. When targeting for maximum edge user performance or user fairness, the developed algorithm flow aims to distribute user/traffic to available cells evenly and deriving an optimal serving range for the cell by adapting their antenna parameters, jointly. In other word, the presented approach does not only change the serving range of each cell but also re-assign users to cells for maximum gain. Thus, it provides load balancing while also optimizing antenna parameters.

4.1   System Model

We consider a wireless communication system with multiple base stations. The target system could be, but not limited to 3GPP-LTE with small cells. For simplicity, downlink transmission is assumed. Achievable capacity for each user can be written in terms of associated users with cell, bandwidth and SINR as

$$\gamma_i = \sum_{j \in \mathbb{B}} x_{ij} \frac{B_j}{N_j} \log\left(1 + \alpha_{ij}\right) \tag{4.1}$$

where $i \in \mathbb{U}$ represents each user, $j \in \mathbb{B}$ indicates base station index, x_{ij} is the logic indicator of user-cell association, N_j shows the total number of users associated with the cell j, B_j represents available bandwidth for each cell, and α_{ij} is the SINR of user i. SINR is formulated as

$$\alpha_{ij} = \frac{P_{ij}}{\sum_{j \in \mathbb{B}} (1 - x_{ij}) P_{i,j} + \sigma_n} \tag{4.2}$$

where $P_{i,j}$ is the received power from jth cell to user i, and σ_n is represented as noise power. The received power can be modeled in terms of user location, omni directional received power, and transmitter antenna beam pattern to represent only the antenna effects on the equation [81]. Thus, the received power becomes

$$P_{ij} = 10^{[K_{ij} + \beta(\theta_{ij})]/10} \tag{4.3}$$

$$\beta(\theta_{ij}) = -\min\left\{ 20, 12 \left(\frac{\theta_{ij} - \phi_j}{\Delta_{\phi_j}} \right)^2 \right\}, \tag{4.4}$$

where K_{ij} represents the omni directional received power in dB, $\beta(\theta_{u,j})$ is antenna pattern gain, Δ_{ϕ_j} and ϕ_j are the parameters of jth base station for 3 dB beamwidth and antenna tilt, respectively.

Total capacity of the system can be written as,

$$\Gamma = \sum_{i \in \mathbb{U}} \gamma_i \tag{4.5}$$

4.2 Proposed Method

In our utility function, we target edge users to increase performance. Therefore, the utility function of the problem can be written as,

$$\mathcal{U}(\boldsymbol{\phi}, \boldsymbol{\Delta}_{\phi}, \mathbf{x}) = \sum_{k \in \mathbb{K}} \gamma_k, \tag{4.6}$$

$$\mathcal{U}(\boldsymbol{\phi}, \boldsymbol{\Delta}_{\phi}, \mathbf{x}) = \sum_{k \in \mathbb{K}} \left\{ \sum_{j \in \mathbb{B}} x_{kj} \frac{B_j}{N_j} \left[\log \left(\sum_{m \in \mathbb{B}} P_{km} + \sigma_n \right) - \log \left(\sum_{m \in \mathbb{B}} (1 - x_{km}) P_{km} \right) \right] \right\} \tag{4.7}$$

where $\mathbb{K} \subset \mathbb{U}$ represents the index numbers of minimum 5 %-tile users. Using (4.1) and (4.2) utility function can be driven as (4.7). A closed form solution to maximization of (4.7) is hard to find. Therefore, an iterative greedy algorithm can be implemented to get closer to a local optimum. The iteration can be given as,

$$A_j(t+1) = \underset{A_j}{arg\,max}\, \mathcal{U}(\boldsymbol{\phi}, \boldsymbol{\Delta}_{\phi}, \mathbf{x}) \qquad\qquad \forall j \in \mathbb{B} \tag{4.8}$$

$$x_{ij} = \underset{x_{ij}}{arg\,max}\, \mathcal{U}(\mathbf{A}, \mathbf{x}), \qquad\qquad \forall j \in \mathbb{B} \forall i \in \mathbb{U} \tag{4.9}$$

where antenna parameters $A_j = \{\phi_j, \Delta_{\phi_j}\}$ is selected from a set of predefined antenna settings.

The implementation of the method can be described as in following steps:

- Initial deployment has fixed antenna parameters (e.g. $\phi = 15°, \Delta_\phi = 10°$) for all the cells

- For each user, pick a cell to connect by maximizing (4.1),

- Iterate following steps for several times

    – For each cell,

        * For each possible antenna setting,

            · Calculate new received signal powers to each user by (4.3).

48
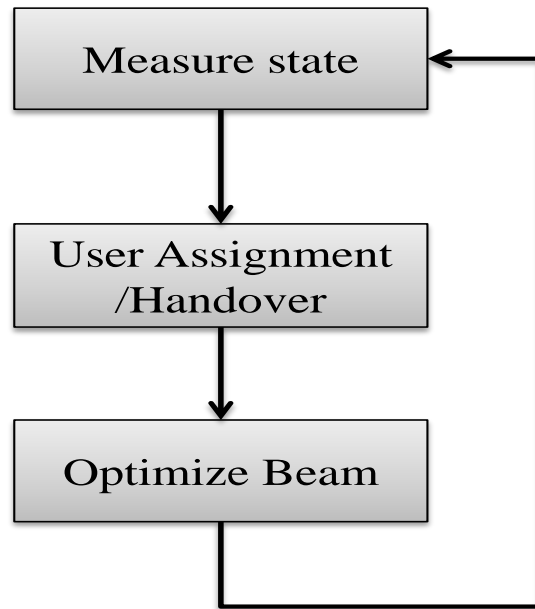
Figure 4.1: Conventional approach for load balancing and antenna optimization

> · Re-associate all the users to maximize (4.1).

> · Determine 5%-tile of user throughputs.

> ∗ Select the antenna settings that maximizes the objective.

> ∗ Renew all the related parameters for the selected antenna setting.

- Do transmission with selected antenna setting and cell-user association until the next measurement period.

The presented algorithm requires high computational power for big networks or implementation clusters, since it requires power calculations for each cell and antenna settings. However, the results clearly show that the joint approach to the problem gives increased performance results compared to conventional methods. The algorithm can be run with a fixed vertical beamwidth to decrease the computational requirement by reducing the number of possible antenna settings.
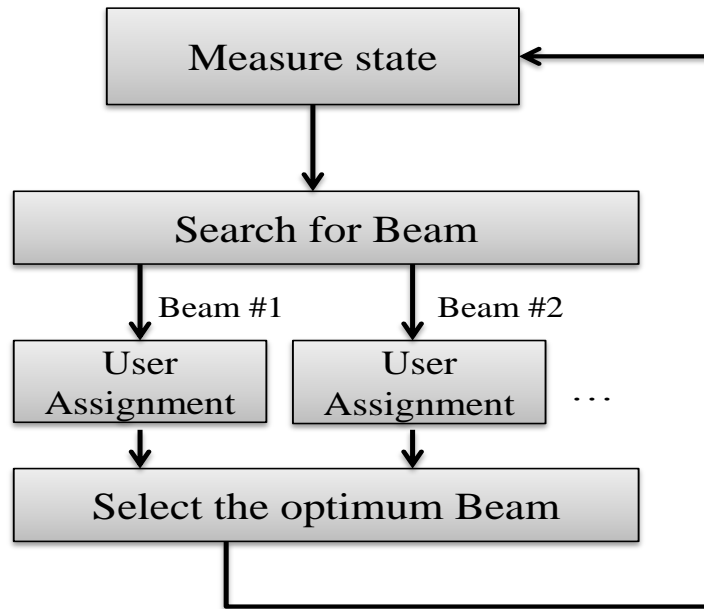
Figure 4.2: Proposed approach for load balancing and antenna optimization

Fig. 4.1 and Fig. 4.2 show conventional and the proposed approach to the problem in algorithm flow. For the both approaches, the system measures the state of users at first as initial to the algorithms. Then, in the conventional approach, users are assigned to cells and antenna beam is optimized, consecutively. In another conventional approach, first the heavily loaded cell reduces its range by changing antenna properties and let the users hand over to other cells. In the proposed approach user association and antenna parameters are optimized, jointly. This is done by a brute force search for each possible antenna setting and it's optimized user-cell association. According to simulation results which are provided in the following section, the proposed approach show significant gain compared to conventional approach.

Table 4.1: Simulation Parameters

Parameter	Description
Network Topology	19 hexagonal Macro cells wrapped around
Small Cells	12 small cells/ Macro cell
Inter-site distance	150m
Individual Users	20 per Macro Cell, Uniformly distributed
Hot spots	Uniformly distributed 4 groups of 20 users
Path loss model	$PL = 72 + 29.2\log_{10}(d)$
Lognormal Shadowing	$\sigma = 8.7\,dB$
Transmit Power	$30\,dBm$

4.3 Performance Evaluation

In order to show effectiveness of the proposed algorithm, system level simulations for LTE small cell deployment has been performed based on simulation parameters provided in [81]. Under 19 hexagonal cell layout with 500 m inter-site distance, 12 small cells uniformly distributed to each cell. Also, in total 100 users are deployed to each cell. 20 of them are uniformly distributed and the rest of the users are deployed in groups of 20 to represent heavy load.

The user throughput and SINR results are shown for 5 different scenarios. The first scenario, fixed antenna w/o load balancing, shows the results for the system where a fixed antenna with optimized settings have been used without any load balancing algorithm. In this scenario the users are associated to the cell which sends the most powerful signal. In the second scenario, fixed antenna, the users are associated with cells to maximize (4.1) and the system has the same antenna settings as the first scenario ($\phi = 15°, \Delta_\phi = 10°$). The third scenario, adaptive antenna, shows results for the system where both antenna parameter adaptation and load balancing separately implemented to emulate conventional approach. The system first associate users to cells to maximize capacity then for this user-cell association the antenna parameters for each cell are optimized. The last two scenarios present the results for the proposed joint approach. While the fourth scenario keeps vertical beamwidth fixed and adapts only antenna tilt in the optimization, the fifth scenario adapts vertical beamwidth and antenna tilts.
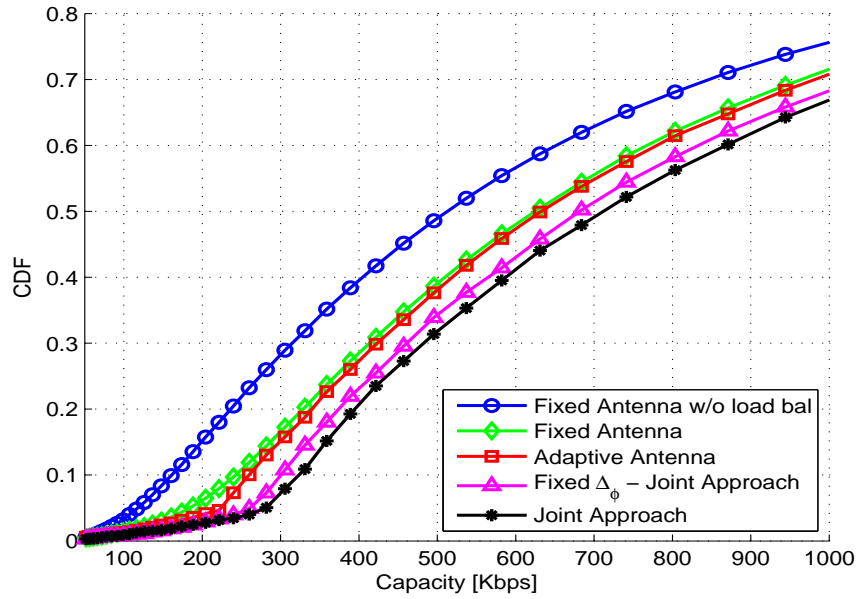
Figure 4.3: Cumulative distribution of achievable capacity that can be accomplished by each user.

Fig. 4.3 illustrates cumulative distribution of achievable capacity of each user. As it can be seen from the figure, the proposed algorithm increases the performance for edge users (5%-tile) and median users (50%-tile). A conventional system with no load balancing algorithm shows 120 kbps and 510 kbps user throughput for edge and median users, respectively. For second and third scenario which can be seen as conventional approach to load balancing problem, the results indicate about 220 kbps and 630 kbps capacity. The proposed approach provides 280 kbps and 720 kbps capacity which shows about 116% and 27% gain for edge users against first and third system scenario, respectively.

Fig. 4.4 shows cumulative distribution of user SINRs. As it can be seen from the figure, the SINR change is not significant in the proposed system, since the SINR is used in the objective function. Compared to first scenario, the edge users' SINR dropped from -4 dB to -5 dB, while the median users' SINR remains same at 3 dB.
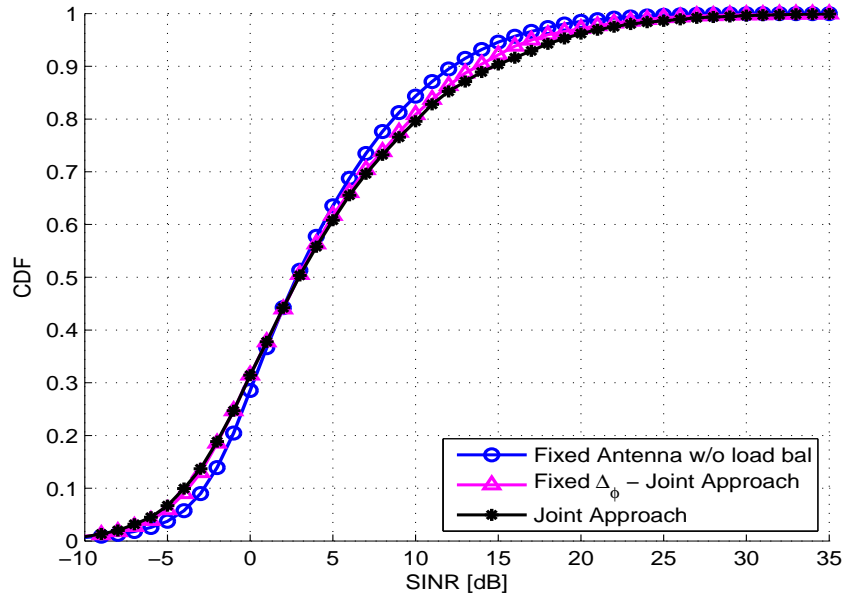
Figure 4.4: Cumulative distribution of average SINR that can be provided to each user.

4.4 Conclusion

The importance of joint approach to load balancing and range optimization has been investigated with the proposed algorithm. The results show that the joint approach can increase total system capacity and edge user capacity by optimizing user assignments to cells and cell ranges, jointly. Edge users observed 27% capacity gain against its counterpart. The required high computation power can be reduced by fixing the vertical beamwidth. SINRs performance of the system also investigated and it is seen that the proposed approach does not affect SINR, dramatically.

Chapter 5: Mobility Performance of Macrocell-Assisted Small Cells in Manhattan Models[3]

Tremendous development on mobile devices increased their requirements from wireless networks with advanced applications, e.g. high definition video conference, cloud computing/storage. These requirements, e.g. high data rate, low delay, drive wireless technology to develop further and to work efficiently. Small cell network is a good candidate to provide the requirements in the future [83]. 3rd generation partnership project (3GPP) has initialized a workshop on Long Term Evolution (LTE) Release 12 to clarify a path to future technologies [84]. Among the various candidate technologies, enhanced small cells attract interest from the majority of companies. 3GPP also released a technical report on the scenarios and requirements of small cell enhancement [85].

Low power short range cell deployments under macrocell coverage have been proposed in the literature to increase total system capacity. In [86], street micro cells are presented, and their signal propagation is investigated. In [83], current problems of small cell deployments and research areas have been discussed. Despite their capability to provide high system capacity, small cells have mobility and interference problems. The deployment of small cells will result in serious interference with neighbor cells (macrocells in co-channel deployments and small cells in small cell dedicated carrier deployments) because of the frequently repeated usage of resources. Also, when user equipment (UE) moves through the network, dense small cells (more than 10 small cells per macro cell) can increase the number of handovers (HOs) and HO failures compared to conventional macrocell deployments. This significantly increases cell planning, management, and optimization efforts due to a large number of HO points.

---

[3]This chapter was published in [82]. Permission is included in Appendix A.

To improve interference management, flexible cell planning, and energy saving, macrocell-assisted small cell concepts, such as Phantom Cell and soft cell are proposed in the literature. In [87], the soft small cells are part of the macrocell and share the same system information with the macro cell. The control signaling can be transmitted from the macrocell and the small cell simultaneously, and this results in an improved SINR through an over-the-air signal combination. In the Phantom Cells concept [88], a massive number of small cells using higher frequency band are deployed. The small cells only handle data traffic, and the macrocells handle all the control signaling. In both soft cell and Phantom Cell conceptions, there is macrocell involvement to improve the link between the small cell and its user. Since dense small cell networks can provide high data rates, these concepts are good candidates to be implemented in crowded urban areas (e.g. downtown New York City). Therefore, the Manhattan grid mobility model, which is widely used for urban areas, is suitable to implement realistic simulations for this concept [89, 90]. In this chapter, The Manhattan grid model is used to implement more realistic scenarios in LTE simulations. Macrocell performance is investigated in the simulator, and the results are interpreted for small cell mobility.

Our main contribution consists of two parts. First, we improve the current LTE simulator for macrocells by incorporating the Manhattan grid mobility model. The Manhattan grid is seamlessly built upon the conventional hexagonal cell layout. Macrocell deployment and UE movement are also specified. Path loss and shadow fading calculation for cells are also elaborated. Secondly, the impact of UE mobility and macrocell location on HO failure and HO rate are thoroughly studied. The simulation results show that macrocell performance highly depends on relative location of neighboring cells and buildings. To improve performance, line-of-site (LOS) to non-line-of-site (NLOS) transitions at the cell borders should be avoided while deploying macrocells.

5.1 Macrocell-Assisted Small Cell Concept

Macrocell-assisted small cells, called Phantom Cells are proposed in [88] for capacity problem in high-traffic outdoor environments. In the Macrocell-assisted small Cell concept, the C-plane/U-plane are split as shown in Fig. 5.1. One major advantage for this configuration is the possibility of offering substantial capacity increase to an existing network at the same time
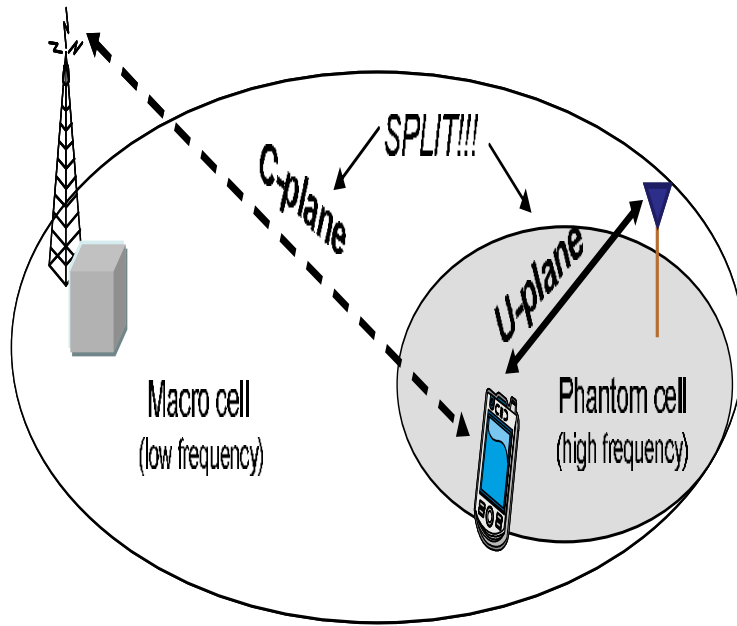
Figure 5.1: Phantom cell C-plane/U-plane split

exploiting the reliable coverage and mobility performance of the macrocell layer. In the proposed architecture, macrocell-assisted small cells are allocated with higher frequency bands while the macrocells keep the existing band. Therefore, the C/U-plane split configuration allows for high capacity connection with U-plane through the small cell (with more bandwidth), while the C-plane is maintained by a more reliable macrocell layer. This configuration also allows operators to deploy a small number of small cells in a sparse manner to boost the user experience at some specific high-traffic spots, which is the case for the initial dense small cell deployment. Since the macrocell layer keeps the reliable coverage and performance, fine cell planning, configuration, and optimization efforts are not required in the small cell layer. For example the operators do not need to worry about the coverage holes any more in the small cell layer. Furthermore, the total capacity can linearly increase as the operators increase the number of cells. This easy-upgrade characteristic is very important in terms of practical system development especially for higher frequency bands, since achieving conventional full cellular coverage is very costly, bothersome, and almost impossible due to poor propagation characteristic at high frequency.

5.2 System Model

Manhattan grid layout and mobility model is assumed to investigate mobility in realistic downtown scenario. The streets and the buildings are organized as in Fig. 5.2. Table 5.1 shows a set of values for block parameters with 500m inter-site distance (ISD) of macrocells. The block length-to-width ratio is chosen as $\sqrt{3}/2$ to fit the layout on hexagonal layout as in Fig. 5.3. The model details are given in the following subsections.
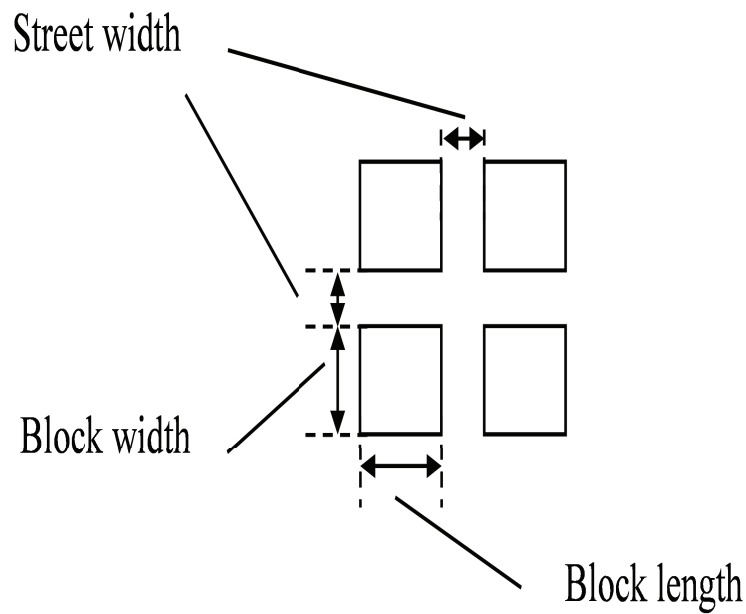
Figure 5.2: Manhattan grid layout

Table 5.1: Block size and street width

Items	Description
ISD of macro eNBs	500 m
Block length	110 m
Block width	≈ 93.3 m
Street width	15 m
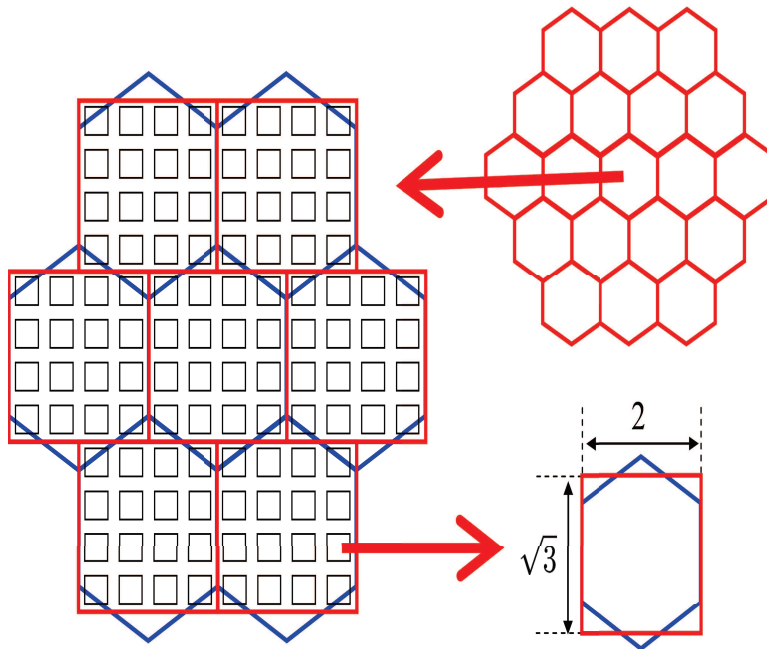
Figure 5.3: Macrocell deployment to the corner of buildings

5.2.1 Macrocell Deployment

To implement the Manhattan model, the conventional hexagonal cell layout has been fit onto Manhattan blocks. Figure 5.3 gives a Manhattan grid layout for macrocell deployment, when the macrocells are located at the corner of building (at the intersection). Macrocells are uniformly deployed to fixed locations in a 19-cell cluster area with each of the macrocells containing 16 Manhattan blocks. The layout also wrapped around to provide continuity.

To analyze different deployment options macrocells can be also located on 4 different locations. Figure 5.4 shows possible locations for macrocells. For each option, whole 19-cell grid has been shifted to desired location.

(a) At the center of the building (b) At the corner of the buiding

(c) At the north of the building (d) At the East of the building
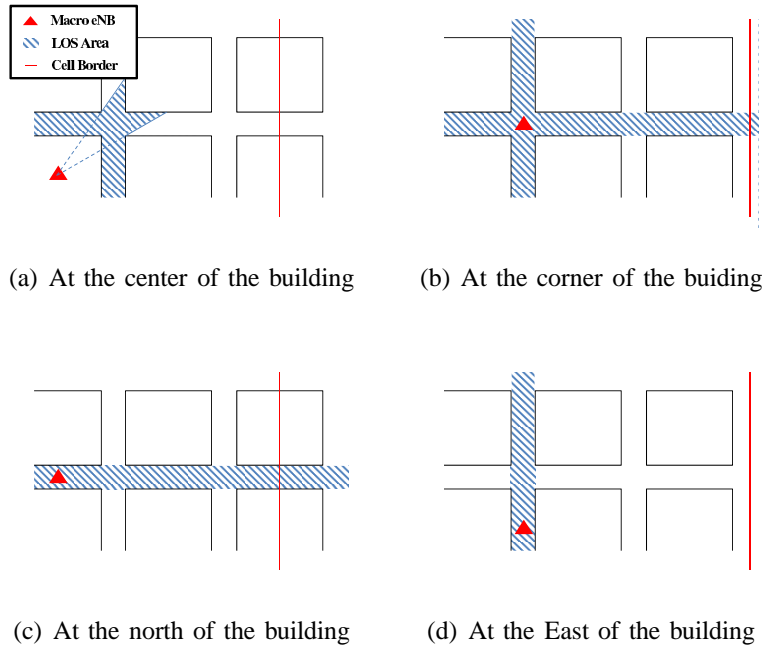
Figure 5.4: Macrocell locations

5.2.2 User Deployment and Mobility

Users are randomly confined to streets with uniform distribution. There is no user in the buildings. Users can move in horizontal or vertical directions. At the intersections, UE chooses a direction to move. The probability of going straight is 0.5 and taking a left or right is 0.25 each. Two speed options are implemented for users. To simulate pedestrian and vehicular mobility, 3 km/h and 50 km/h speeds are chosen as user speed, respectively.

5.2.3 Signal Propagation

The effects of terrestrial environment on signal propagation can be classified into three types, i.e., the path loss, slow fading caused by shadowing from obstacles, and fast fading caused by multipath effects. In this subsection, generation of path loss and shadowing in the Manhattan grid is described.

59

In the Manhattan grid, there are two conditions for the relative position between UE and the Macro cell, i.e., LOS, NLOS that affect the distance loss. Figs. 5.4 shows assumed LOS and NLOS regions for different Macrocell locations. The path loss formulas for the LOS condition and the NLOS condition are given in the urban macro (UMa) model (Table A1-2 in [91]).

In urban areas, shadow fading has the log-normal distribution, and changes slowly over the period of use. When user moves, shadow fading has to be updated according to the autocorrelation between shadow fading at the current user position and the next user position. Shadow fading is generated and updated using the following steps:

1. N independent normal distributed random variables are created, i.e., $x = [x_1, x_2, \ldots, x_N]$, where N is the number of cells, $x_i \sim \mathcal{N}(0, 1)$, $i = 1, 2, \ldots, N$.

2. The cross-correlation matrix Γ is constructed as follows:

$$\Gamma = \begin{bmatrix} 1 & \rho_{12} & \cdots & \rho_{1N} \\ \rho_{21} & 1 & \cdots & \rho_{2N} \\ \vdots & \vdots & \ddots & \vdots \\ \rho_{N1} & \rho_{N2} & \cdots & 1 \end{bmatrix}, \tag{5.1}$$

where $\rho_{ij} = 0.5$ ($i \neq j$) is the correlation coefficient of the shadow fading between the radio links i and j. Since Γ is a symmetric positive definite matrix, it can be decomposed into a lower and upper triangular matrix by Cholesky decomposition technique, i.e., $\Gamma = C^T C$ and C is an upper triangular matrix.

3. Shadow fading standard deviation is constructed in vector $\Sigma = [\sigma_1, \sigma_2, \ldots, \sigma_N]$, where σ_i is the shadow fading standard deviation at link $i, i = 1, 2, \ldots, N$. In UMa model (Table A1-2 in [91]), the standard deviation is 4 for the LOS condition and 6 for the NLOS condition. Let $y = [y_1, y_2, \ldots, y_N] = xC\text{diag}(\Sigma)$. Then, y_i will be the cross-correlated log-normal shadow fading component for radio link i.

4. When UE moves, the shadow fading components have to be updated. Let x be the independent log-normal vector at the current position obtained in step 1) and $\overline{x}$ be the one at the future position, which is Δd away from the current position. According to the Gudmundson auto-correlation model, the correlation between x and $\overline{x}$ is $\mathbb{E}[x^T\overline{x}] = \text{diag}([\tau_1, \tau_2, \ldots, \tau_N])$, where

$$\tau_i = e^{-\frac{|\Delta d|}{D_i}}, i = 1, 2, \ldots, N. \tag{5.2}$$

According to the UMa model, $D_i = 37$ m if link i is LOS and $D_i = 50$ m if link i is NLOS (TABLE A1-7 in [91]). Then, the update formula for ith component of $\overline{x}$ is $\overline{x}_i = \tau_i * x_i + \sqrt{1 - \tau_i^2} * z_i$, where $z_i \sim \mathcal{N}(0, 1)$ is independent of x_i. $\overline{x}_i$ will also be normally distributed with mean 0 and variance 1.

5. The cross-correlated log-normal shadow fading vector y at the future position is updated to be $\overline{y} = \overline{x}C\text{diag}(\Sigma)$.

6. Iterate over steps 4) and 5) throughout the simulation.

5.3 Performance Evaluation

This section presents mobility results for the Manhattan grid mobility model with urban macrocells.

5.3.1 Simulation Setup

Table A1-2 in [91] is used as basic simulation settings. Additionally, Table 5.2 shows mobility parameters implemented in the simulations. In order to simulate and analyze the infinite cellular network using only one macrocell cluster, the wrap-around model in [92] is utilized. SINRs and HO rate are used as the performance metric. Also, SINR just before the HO command is sent, is observed to investigate HO failure. As a tentative failure threshold -8 dB SINR is used to find out failure rate. Since SINR before HO is the last SINR value that user sees, it also shows the minimum SINR.

Table 5.2: Parameters for mobility performance evaluation

Items	Description
Traffic load	100%
Multipath channel model	Vehicular A
RSRP Measurement bandwidth	25 resource blocks
L1 measurement period	200 msec (5 samples)
Handover preparation (decision) delay	40 ms
Handover execution time	40 ms
SINR threshold for HO failure	-8 dB
Time-to-trigger	160 msec
A3 offset	3 dB

5.3.2   Effect of Macrocell Location

In Fig. 5.5, cumulative distribution function (CDF) of SINR just before the HO is shown for different locations of macrocell at 50 km/h user speed. As it can be seen from the figure, while macrocells are located at the center or at the North, HO failure rate is about 3%. However, when the macrocells are located at the corner or at the East, HO failure rate increases up to 25%. The main reason for that difference can be explained by LOS to NLOS change at the border of a cell as shown in Fig. 5.6. For corner and East location cases, when UE makes a turn towards the target cell, LOS/NLOS condition changes and the received signal power from source cell drops, dramatically. When macrocell is located at the center, LOS condition only occurs at the center area as seen in Fig. 5.4(a). Therefore, sudden signal level drop at cell boarder does not occur for center case. However, in the North side location case, when the LOS to NLOS change happens at the border, it happens for both target cell and the source cell. Therefore, interference and signal power level drop with similar rates which does not affect the mobility performance.

In summary, macrocell location, more specifically where the LOS/NLOS condition change occur, affects the mobility performance in Manhattan grid model. That is, if the LOS/ NLOS transitions occur in HO areas, the HO performance is degraded due to dramatic change on signal levels for the source cell and target cell. It is noted that macrocells are more likely to be deployed at the center of the building (Fig. 5.4(a)), but the other cases (Figs. 5.4(b), 5.4(c), 5.4(d)) can
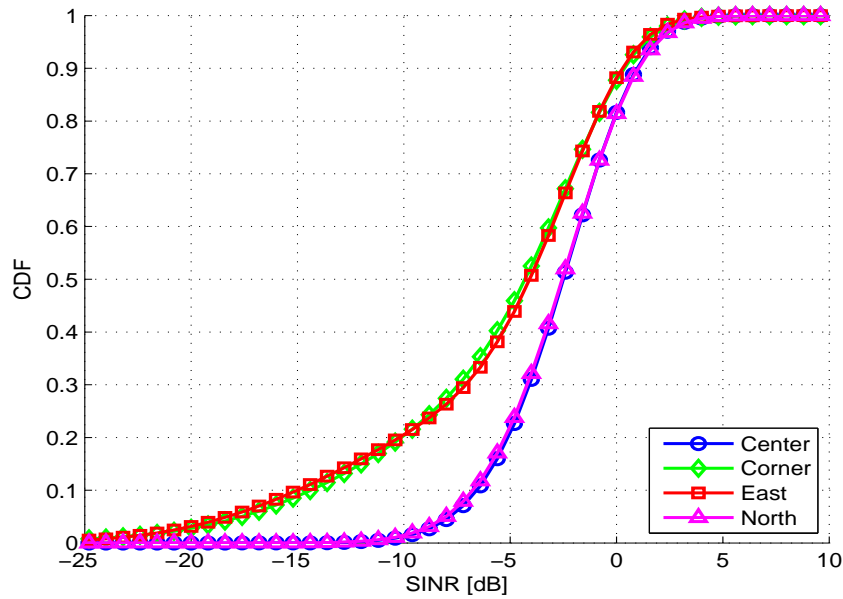
Figure 5.5: CDF of SINR Before handover for 50km/h

also be observed in actual deployments. The location based issues can be mitigated in a case-by-case manner for cell optimization. For instance, HO points can be shifted by cell-specific HO offset or cell coverage adjustment by antenna tilting to change HO area to avoid possible LOS to NLOS transitions during HO. These problems caused by LOS/NLOS condition change can be solved with better network planning and optimization. However, since small cells are deployed in large numbers and randomly, this kind of effort can require more operational cost for small cells compared to macrocells. Therefore, macrocell-assisted mobility management gains an interest to reduce operational cost to provide good HO performance.

5.3.3 Effect of User Speed

In Fig. 5.7, CDF of SINR just before the HO is shown for different speeds, when macrocell is located at the center or at the corner. As it can be seen from the figure, UE speed has a significant impact on HO performance. When UE speed drops to 3 km/h, HO failure rate is also drops from 3% to 0.1% and from 25% to 14% compared to 50 km/h for center and corner locations, respectively.
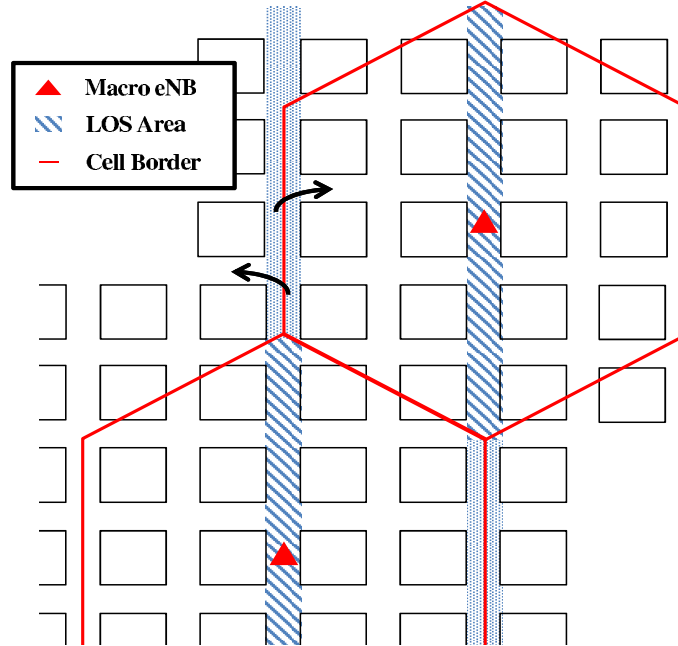
Figure 5.6: Handover location

5.3.4 Overall System Performance

In Fig. 5.8 and Fig. 5.9, CDF plots of SINR for whole coverage area are shown for user speed 3 km/h and 50 km/h, respectively. The figures indicate that the minimum user SINR is higher than -5 dB, i.e. there are no coverage holes, in all the cases. It can also be seen that the median user SINR (i.e. 50%-tile user) is around 6-7 dB for different locations. It indicates that location of macrocell does not affect overall SINR performance.

5.3.5 Comparison between Macrocell Deployment and Small Cell Deployment

Table 5.3 shows a summary of HO performance results for macrocell deployment in Manhattan model and compares them with dense small cell deployments results. In the table HO rate, HO failure rate and as a combination of these two, handover failure in time, are given for 4 different cases of macrocell deployment and for 2 different scenarios of small cell deployment. The combination, handover failure, can be seen as connection loss rate because of mobility and this loss requires users to re-establish connection with the network. When macrocell and small cell deployments are compared for 50 km/h user speed, the handover rate is a little more than
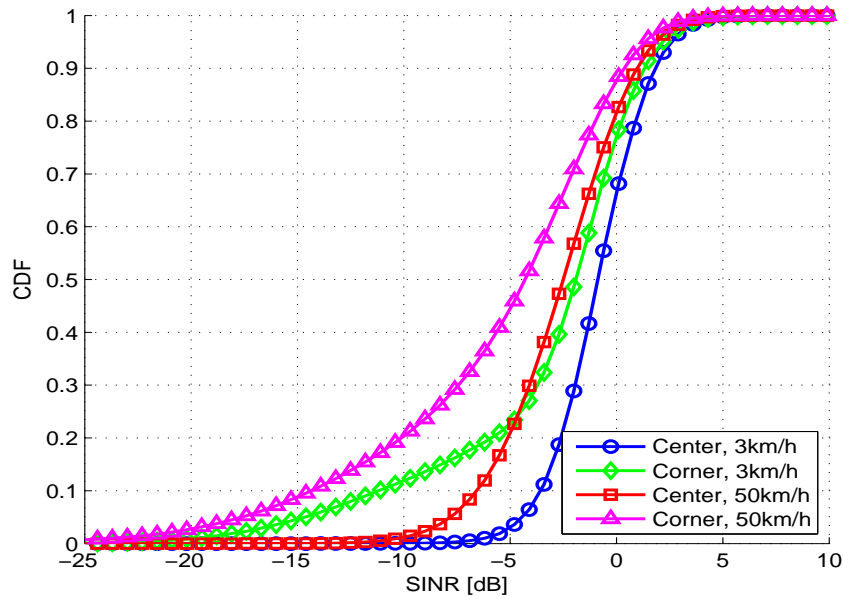
Figure 5.7: CDF of SINR Before handover for different speeds

doubled. This may be acceptable for some networks. However, connection loss rate for small cells is more than 4 times and more than 30 times compared to macrocells located to center and to corner, respectively. These results show the importance of macrocell cooperation for mobility performance as it is introduced in [88].

5.4 Conclusions

Macrocell cooperation is expected to be implemented to improve interference and mobility performance in dense small cells which are candidate solution for high data rate demanding urban areas. Therefore, by implementing Manhattan grid layout, capability of macrocells to support small cell mobility has been investigated for downtown environment of crowded cities. Macrocells are placed on different locations to compare its effects. The results show that without a macrocell support, dense small cells would require at least 4 times more re-connection load because of the mobility problems. Compared to best case macrocell deployment this load requirement goes up to 30 times more. The results also show that there are location related problems for Manhattan model due to LOS to NLOS transitions in HO area. These issues can be mitigated by network planning

65
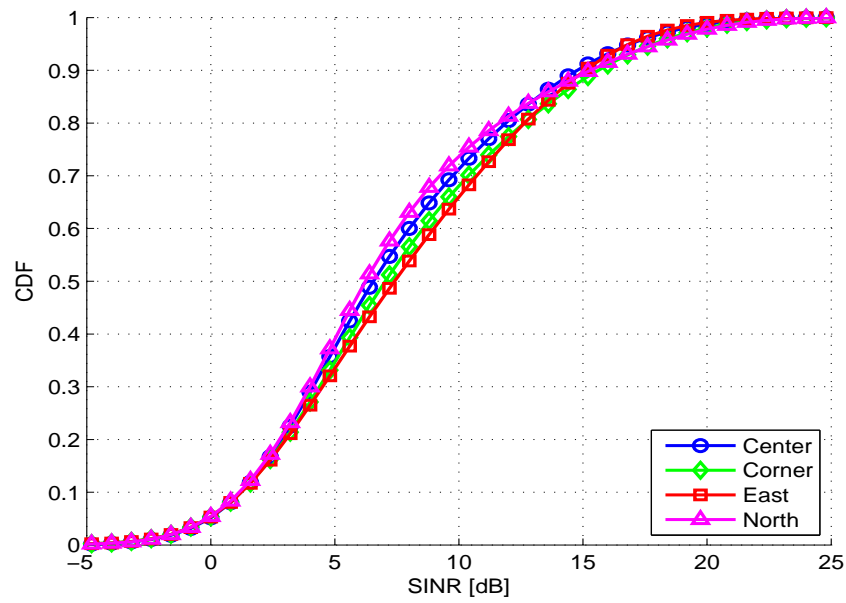
Figure 5.8: CDF of SINR for 3 km/h

and optimization methods. Implementation of such methods would be more practical for macrocell deployment compared, since small cell deployments are random and in mass amount. Therefore, we can say that macrocell cooperation with dense small cells gives a huge performance advantages for mobility issues and network planning.
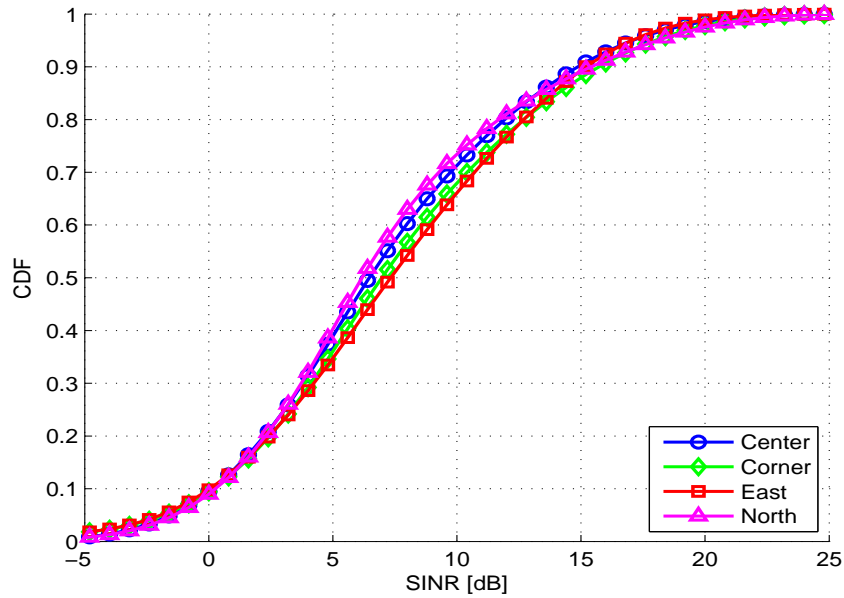
Figure 5.9: CDF of SINR for 50km/h

Table 5.3: Handover performance

Case	HO rate [HOs/sec/user]	HO failure rate [Fails/HO]	HO failure [Fails/sec/user]
Macrocell, 3km/h, Center	0.0058	0.001	5.8×10^{-6}
Macrocell, 3km/h, Corner	0.0054	0.14	756×10^{-6}
Macrocell, 50km/h, Center	0.0662	0.03	1986×10^{-6}
Macrocell, 50km/h, Corner	0.0644	0.25	16600×10^{-6}
Small cell, 3km/h	0.0131	0.06	786×10^{-6}
Small cell, 50km/h	0.1478	0.45	66510×10^{-6}

Chapter 6: Arraymetrics: Authentication Through Chaotic Antenna Array Geometries

The emergence of quantum computing has recently shown that currently used conventional encryption techniques can be cracked with ease in the near future [93]. This pushed researchers to finding new horizons that satisfy security requirements through the use of non-cryptographic approaches [94], such as utilizing the physical layer (PHY) properties of the system [95] or machine learning techniques [96] to infer presence of adversaries and defend accordingly. Quantum password cracking aside, PHY authentication becomes critical in authenticating simplex broadcasts in which cryptographic approaches cannot be utilized, such as spoofed global positioning system (GPS) signals as in [97]. In [98], layered security approaches were investigated in detail , and were shown to be redundant and inflexible for future network structures [99].

Authenticating UEs using their PHY characteristics in developing a PHY security approach have been gaining traction [100]. The idea of extracting artifacts caused by imperfections in the source network interface card to authenticate devices have been around for more than a decade [101]. Channel similarities in addition to the RF fingerprint of the device, of which recent extraction advances is detailed in [102], are also utilized in the control-layer based authenticator designed in [103], that aims to replace high-latency connections to remotely located authentication servers with local verification among 5G heterogeneous network (HetNet) access points (APs).

Antenna array geometry optimization literature has historically focused on designing "smart" [104] or adaptive antenna arrays with improved far- or near-field spatiospectral localization [105]; and is rich in this context. Although PHY security using multiple antennas was also introduced more than a decade ago when signals received from MIMO transmitters are authenticated using the spatiospectrotemporal correlation of the wireless channel in [106]. Despite the further studies of PHY security of MIMO systems in [107, 108], the literature for PHY authentication for this systems remains underdeveloped to date.

Physical layer security aspect of multiple antenna configurations were most recently evaluated to the extent of passive confidentiality and active availability attacks using massive MIMO systems [109]. Recent developments in signal intelligence techniques for MIMO wireless communications are surveyed in [110]. A secure receive spatial modulation scheme that randomizes precoders but not antenna arrays is proposed in [111].

In this work, we propose a novel authentication scheme that combines chaotic antenna array geometries with pseudorandom pilot sequences and antenna array activation sequences. This novel approach combining all three allows unclonable authentication devices, even if the adversaries eavesdrop the message exchange or figure out the unique antenna array geometry by x-ray radiography. The accuracy and scalability of the approach is investigated. It is observed that the proposed authentication scheme can provide 1% false authentication rate at $10\,\mathrm{dB}$ SNR, while it is achieving less than 1% missed authentication rates.

The rest of this chapter is organized as follows: Section II provides the adopted system model. Section III introduces the proposed chaotic and pseudorandom designs and briefly presents their effects on the detection metrics. The detection performance results are shown in Section IV. Finally, the chapter is concluded in Section V.
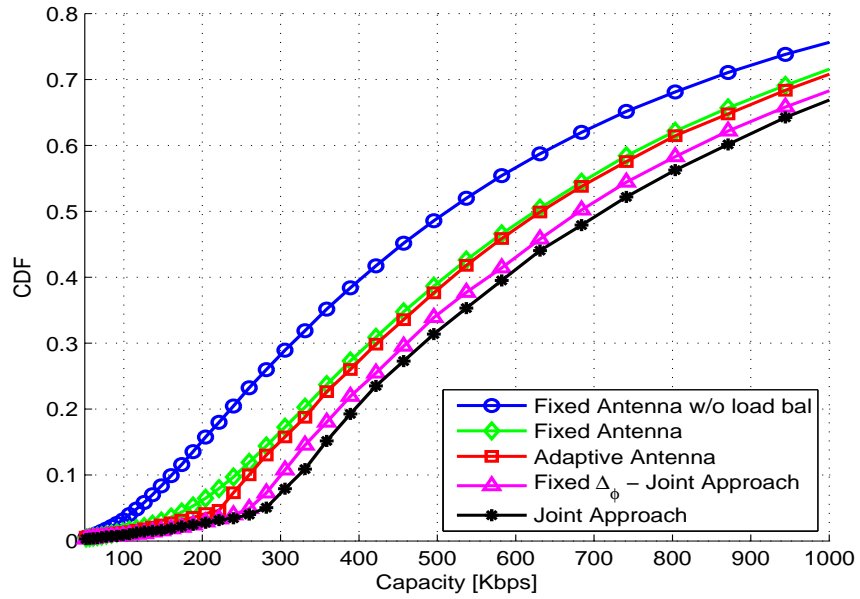
Figure 6.1: Cumulative distribution of achievable capacity that can be accomplished by each user.

Throughout this chapter, vectors are represented using lowercase bold-face letters, matrices are uppercase bold-face letters, and non-bold letters are used for scalars. The superscripts $(\cdot)^{\mathsf{H}}$, $(.)^{-1}$ stand for the conjugate-transpose, and inverse operations, respectively. $\mathbb{C}$ represents the complex numbers domain, $\sim \mathcal{CN}\left(\mu, \sigma^2\right)$ corresponds to complex Gaussian distributed random variable with mean μ and variance σ^2, and $\mathcal{U}\left(a, b\right)$ corresponds to the uniformly distributed random variable between a and b. $\|\cdot\|$ corresponds to the Euclidean norm, $A \odot B$ and $A \oslash B$ correspond to the Hadamard multiplication of matrices A and B and division of matrix A to B, respectively.

The authenticating device and the device being authenticated will hereinafter be referred to as "Seraph" and "Neo", respectively, with subscripts $\cdot_s$ and $\cdot_n$ used to describe their respective attributes.

Fig. 6.1 illustrates cumulative distribution of achievable capacity of each user. As it can be seen from the figure, the proposed algorithm increases the performance for edge users (5%-tile) and median users (50%-tile). A conventional system with no load balancing algorithm shows 120 kbps and 510 kbps user throughput for edge and median users, respectively. For second and
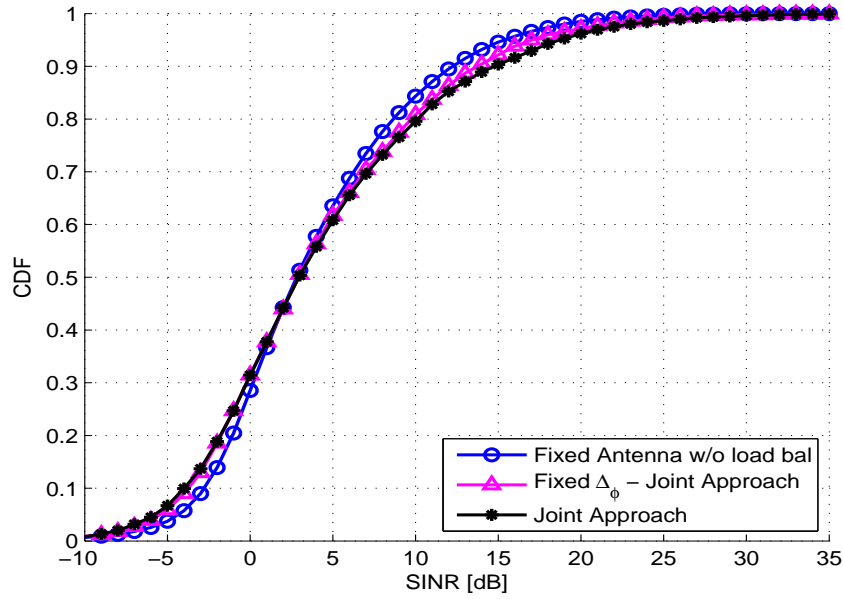
Figure 6.2: Cumulative distribution of average SINR that can be provided to each user.

third scenario which can be seen as conventional approach to load balancing problem, the results indicate about 220 kbps and 630 kbps capacity. The proposed approach provides 280 kbps and 720 kbps capacity which shows about 116% and 27% gain for edge users against first and third system scenario, respectively.

Fig. 6.2 shows cumulative distribution of user SINRs. As it can be seen from the figure, the SINR change is not significant in the proposed system, since the SINR is used in the objective function. Compared to first scenario, the edge users' SINR dropped from -4 dB to -5 dB, while the median users' SINR remains same at 3 dB.

6.1 System Model

The working principle of this system is similar to that of an active RFs identification (RFID) tag. But, instead of the device-specific variation of binary load state or load impedance as a function of time, it is assumed that Seraph has identified and saved the particular pilot sequence transmitted by Neo, the particular antenna activation sequence used by Neo and the chaotic antenna array geometry identifying Neo into an allowlist during a first encounter with Neo. This and subsequent sections investigate ensuing encounters, during which Seraph authenticates Neo's identity by simultaneously

71

verifying all attributes of Neo. The analysis further assumes that, as is the case with RFID tags, Seraph and Neo are synchronized; and the wireless propagation channel between each antenna of Seraph and Neo is representable in the form of a single tap over the utilized bandwidth without loss of generality, is time-invariant throughout the transmission interval, and is known by Seraph through readily available techniques.

Neo is equipped with $M_n = H_n \times V_n \in \mathbb{N}$ antennae wherein $H_n \in \mathbb{N}$ and $V_n \in \mathbb{N}$ correspond to the number of antennae on the horizontal and vertical edges of Neo's 2D antenna array. Neo's 2D antenna array starts off as a standard $\lambda_0/2$ spaced uniform linear antenna array (ULAA), where λ_0 is the free space wavelength at the center carrier frequency. Each antenna element starts off as square patch antennae of edge length $\lambda_g/2$, where $\lambda_g < \lambda_0$ is the guided wavelength at the center carrier frequency, and each vertex of each antenna element is translated from its original location as $p_{m,\alpha} = \bar{p}_{m,\alpha} + u_{x,m,\alpha}\hat{i} + u_{y,m,\alpha}\hat{j}$, where $p_{m,\alpha}$ is the final coordinate of the $\alpha \in \mathbb{Z}^+_{\leq 4}$th the vertex of the $m \in \mathbb{Z}^+_{\leq M_n}$th antenna element, $\bar{p}_{m,\alpha}$ is the original coordinate thereof, $u_{x,m,\alpha}$ and $u_{y,m,\alpha}$ are both $\sim \mathcal{U}\left(-\lambda_g/4, \dfrac{\lambda_0 - \lambda_g}{4}\right)$ and denote the horizontal and vertical displacement of the aforementioned vertex from its original location, respectively, and $\hat{i}$ and $\hat{j}$ are the horizontal and vertical unit length vectors, respectively. Furthermore, the joint probability density function (PDF) for any two displacement satisfies $f_U\left(u_{\beta_0,m_0,\alpha_0}, u_{\beta_1,m_1,\alpha_1}\right) = f_U\left(u_{\beta_0,m,\alpha_0}\right) f_U\left(u_{\beta_1,m,\alpha_1}\right) \forall \beta_{0,1} \in \{x, y\}; m_{0,1} \in \mathbb{Z}^+_{\leq M_n}; \alpha_{0,1} \in \mathbb{Z}^+_{\leq 4}$. Note that by independently displacing all vertices in two dimensions, each antenna element is translated, rotated, scaled or skewed chaotically from the ULAA design. As a result, it is assumed that complex noise is introduced to Neo's spatial signature in the transmit direction of Ω [112] as

$$h_n\left(\Omega\right) = \frac{h\left(\Omega\right) + \sigma_h \tilde{h} \odot e_{\mathrm{t}}\left(\Omega\right)}{\sqrt{2}}, \tag{6.1}$$

wherein $h(\Omega) \in \mathbb{C}^{M_n \times 1}$ is the spatial signature of Neo's nonmodified ULAA in the transmit direction of Ω as described in [112, Eq. (7.24)] of which construction is not recited here due to space constraints, $\sigma_h \in \mathbb{R}^+$ is the standard deviation thereof and corresponds to the positive square root of the channel gain, $e_t(\Omega) \in \mathbb{C}^{M_n \times 1}$ is Neo's nonmodified ULAAs unit spatial signature in the transmit direction of Ω as described in [112, Eq. (7.25)], and $\tilde{h} \in \mathbb{C}^{M_n \times 1}$ is the introduced chaotic noise of which each element is $\sim \mathcal{CN}(0,1)$ independent from others. Accordingly, we will refer to Neo's final ULAAs unit spatial signature in the transmit direction of Ω as

$$e_n(\Omega) = \frac{\sqrt{2}h_n(\Omega) - h(\Omega)}{\sigma_h} \oslash \tilde{h}. \tag{6.2}$$

Each antenna is connected to an independent RF chain that is capable of carrying a complex (IQ modulated) sinusoid pulse uncorrelated to those of other antennae. The reciprocal of the duration of each pulse is analogous to widely known "baud rate" and is assumed constant, at least for Neo, to ease practical aspects concerning transceiver implementation. Neo may also utilize nonsinusoidal wavelets, or, further utilize plurality of wavelets wherein each signal element utilizes a different wavelet for further scalability and security, but these are beyond the scope of this art and will be considered in future works to maintain the work in hand concise. Neo transmits the pilot sequence over $T_n \in \mathbb{N}$ baud intervals, and the pilot symbol modulating the sinusoid transmitted from the $m \in \mathbb{Z}^+_{\leq M_n}$th antenna during the $t \in \mathbb{Z}^+_{\leq T_n}$th baud interval is given in the mth row and tth column of the pilot matrix $X_n \in \mathbb{C}^{M_n \times T}$ and denoted by $X_n(m,t)$, wherein $\angle X_n(m,t) \sim \mathcal{U}(-\pi, \pi)$ and

$$|X_n(m,t)| = \begin{cases} \sim \sqrt{\mathcal{U}(0,1)} & , v_{n,m,t} \geq v_n \\ 0 & , \text{o.w.} \end{cases}, \tag{6.3}$$

where $v_{n,m,t} \sim \mathcal{U}(0,1)$ is a random variable that determines whether Neo's mth antenna during the tth baud interval and v_n is Neo's activation threshold that determines the antenna activation probability; furthermore

$$f_P\left(v_{n,m_0,t_0}, v_{n,m_1,t_1}\right) = f_P\left(v_{n,m_0,t_0}\right) f_P\left(v_{n,m_1,t_1}\right) \forall m_0, m_1 \in \mathbb{Z}_{\leq M_n}^+; t_0, t_1 \in \mathbb{Z}_{\leq T_n}^+. \tag{6.4}$$

A zero entry in X_n implies that no transmission occurs from that antenna during that baud interval.

Seraph is equipped with $N_s \in \mathbb{N}$ antennae that is formed in a nonmodified 2D ULAA, and has the default spatial signature thereof. Accordingly, the channel matrix $H_n \in \mathbb{C}^{N_s \times M_n}$ is composed as done in [112, Eq. (7.56)], with the difference being the unit spatial signature in the transmit direction of Ω term denoted by $e_t(\Omega)$ is replaced with $e_n(\Omega)$ derived in (6.2). The signal received at Seraph's $n < N_s$th antenna at the end of the $t < T_n$th baud interval is given on the nth row and tth column of $y_s \in \mathbb{C}^{N_s \times T_n}$, where

$$y_s = H_n X_n + w, \tag{6.5}$$

where $w \in \mathbb{C}^{N_s \times T_n}$ is the additive white Gaussian noise (AWGN) matrix comprising independent elements identically distributed with $\sim \mathcal{CN}\left(0, (\sigma_h/\gamma_n)^2\right)$ wherein γ_n is Neo's SNR.

6.2 Proposed Receiver

Since Seraph relies on random deviations of spatial signature, a detection algorithm for Neo's spatial signature deviation can be implemented to decide if the received signal is coming from Neo or not. The detection algorithm can be derived by correlating Neo's expected received signal over y_s. The correlation is calculated using

$$\rho = \text{tr}\left(X_n{}^{\mathsf{H}} H_n{}^{\mathsf{H}} y_s\right). \tag{6.6}$$

As noise floor is sensitive to temperature and possible signal emission from imposters, the noise variance, $\hat{\sigma}_n^2 \in \mathbb{R}$, is estimated by similarly correlating $\boldsymbol{y}_s$ with any signature orthogonal to that of Neo and all other possible authorized users. The detection metric $\beta \in \mathbb{R}$ is then given by

$$\beta = \frac{\rho}{\hat{\sigma}_n^2}. \tag{6.7}$$

The detection metric is then compared to a threshold value (ψ). To minimize the error, one threshold can be selected as half of the distance between two states as

$$\psi_e = \frac{\mathrm{tr}\left(\boldsymbol{X}_n{}^\mathsf{H}\boldsymbol{H}_n{}^\mathsf{H}\boldsymbol{H}_n\boldsymbol{X}_n\right)}{2\hat{\sigma}_n^2}. \tag{6.8}$$

However, ψ_e is not a good threshold for low SNR scenarios, which results in high false alarm rates. To prevent that, a threshold (ψ_{FA}) can be precalculated to fix the false alarm probability to a designed value. False alarm probability can be represented as

$$\mathrm{Pr}\left(\mathrm{FA}\right) = \mathrm{Pr}\left(\beta > \psi | \boldsymbol{y}_s = \boldsymbol{w}\right) \tag{6.9}$$

which is $\sim \mathcal{N}\left(0, \mathrm{tr}\left(\boldsymbol{X}_n{}^\mathsf{H}\boldsymbol{H}_n{}^\mathsf{H}\boldsymbol{H}_n\boldsymbol{X}_n\right)\right)$. The final threshold is found as the combination of both thresholds as

$$\psi = \max(\psi_e, \psi_{FA}) \tag{6.10}$$

to improve the performance of the system. Performance analysis for a variety of false alarm thresholds is presented in section 6.3.

6.3   Performance Analysis

To evaluate the proposed authentication method, link level simulations have been performed under highly scattering Rayleigh channel. Seraph is assumed to have 512 antennas at all times, while Neo may have different number of active antennas depending on η_n.
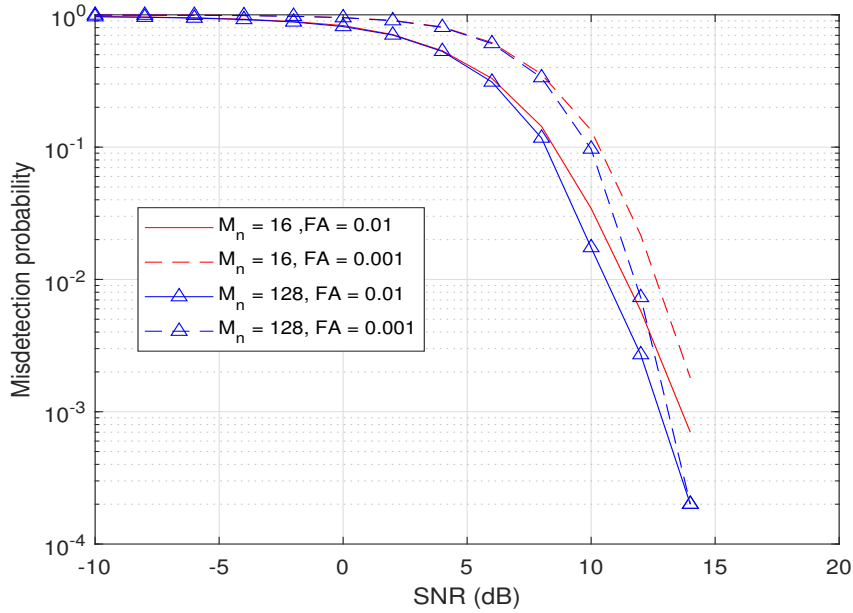
Figure 6.3: Missed detection rate for various M_n and false alarm targets.

In fig. 6.3, missed detection rate of Neo's signature is presented against SNR. The proposed method fails to authenticate Neo with less than 1% probability at most at 13 dB SNR if $M_n = 16$ antennas are activated while $\Pr\left(\text{FA}\right) = 0.001$. It is also seen that 1% misdetection probability can be achieved when 8 dB SNR for both $M_n = 16$ and $M_n = 128$ active antennas with relaxed FA requirement of $\Pr\left(\text{FA}\right) = 0.01$. Lower rates are possible as the number of active antennas are increased or false alarm probability requirement is relaxed.

fig. 6.4 shows false detection rates of Neo's signature when Seraph is only receiving noise. As it is seen from the figure, the desired FA rates of $\Pr\left(\text{FA}\right) = 0.001$ and $\Pr\left(\text{FA}\right) = 0.01$ are closely achieved for SNR values upto 12 dB and 10 dB, respectively. After that SNR values the secondary threshold of ψ_e becomes effective and improves the false alarm performance for Neo's signature detection algorithm.

The success rate of a random signature authentication is presented in fig. 6.5. In this scenario, Seraph receives a signal from a transmitter which has a random signature that is different than Neo's signature. As seen in the figure, false detection performance shows similar behaviour to the previous scenario where only noise is received by Seraph. Due increased signal power and
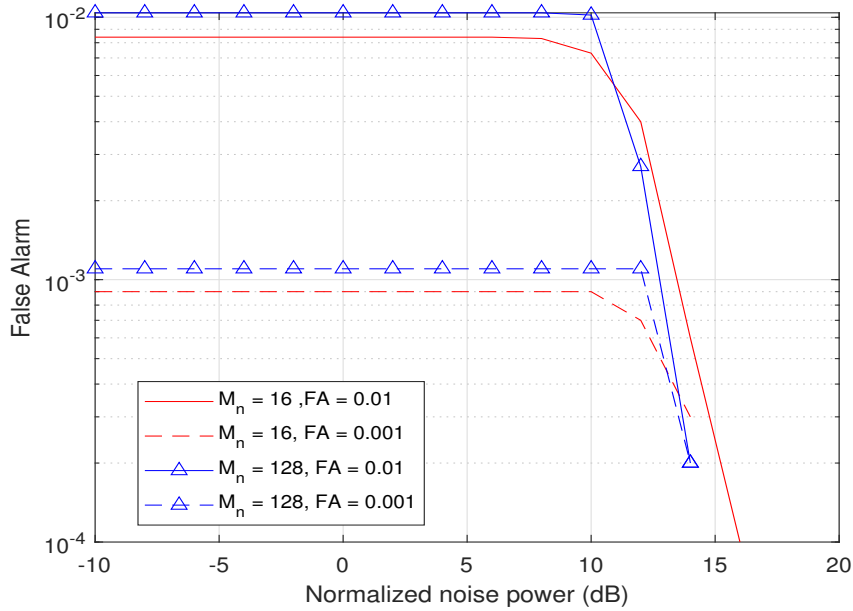
Figure 6.4: False detection rate when receiving only noise, for various M_n and false alarm targets.

false alarm rates being fixed for noise only scenario, false authentication rates slightly increases at around $10\,\mathrm{dB}$ SNR. Then similar to previous case, after SNR values of $12\,\mathrm{dB}$ and $10\,\mathrm{dB}$ for $\mathrm{Pr}\,(\mathrm{FA}) = 0.001$ and $\mathrm{Pr}\,(\mathrm{FA}) = 0.01$, respectively, the secondary threshold of ψ_e becomes effective and improves the false alarm performance.

6.4   Conclusion

A novel authentication approach combining chaotic antenna array geometries with signal and antenna activation sequences has been presented. Possible degrees of freedom in perturbing antenna array geometries, affected physical properties and their detection are presented. While enforcing false alarm rate to be less than 1%, the proposed authentication method is able to provide less than 1% missed detection rates above It is observed that the proposed authentication scheme can provide 1% false authentication rate at $8\,\mathrm{dB}$ SNR. Practical approached to randomized chaotic antenna array manufacturing and statistical signature distribution of the manufactured arrays can be investigated as a future study.
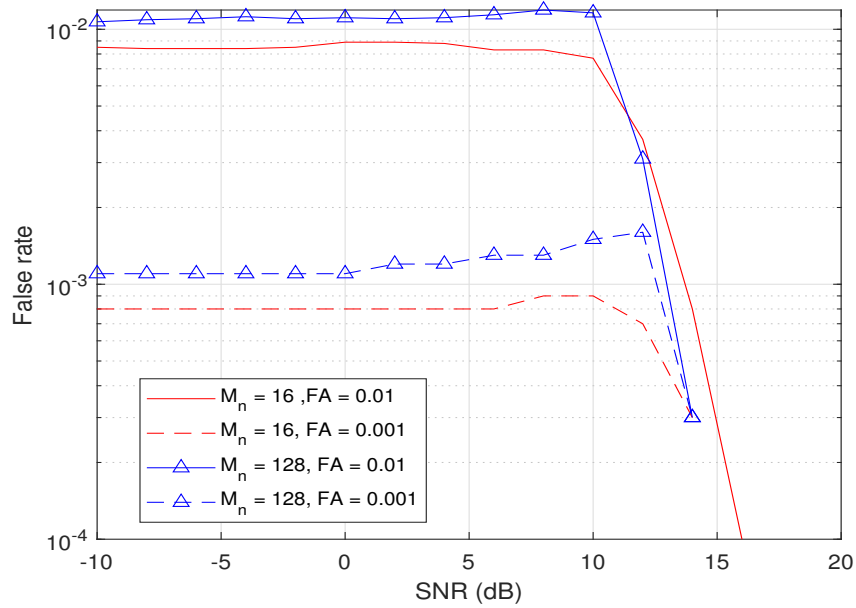
Figure 6.5: False detection rate when receiving signature from a random transmitter for various M_n and false alarm targets and random transmitter's SNR.

Chapter 7: RF Circuit Implementation

of a Real-Time Frequency Spread Emulator[4]

On-site measurements provide reliable and realistic results for evaluation of prototype devices. However, it is time-consuming and costly to execute, especially for air-ground communication due to necessity of an airplane. In order to mitigate these challenges, measurement instruments that generate desired environmental channel effects are widely utilized as channel emulators to facilitate affordable evaluation and verification tool in the laboratory environments. Channel effects, i.e. time dispersion, frequency dispersion, and additive noise, can be emulated using the measurement instruments presented in the literature. [114] and [115] introduce hardware designs that add white Gaussian noise to baseband signals. [116] proposes an infinite impulse response (IIR) filter that introduces time varying channel to baseband signals. [117] presents a Doppler emulation method with partially overlapping windows to overcome issues of finite response filters. [118] implements Rayleigh fading channel using low computational resources on an FPGA board. [119–121] demonstrate doubly dispersive emulators that affect the signal in time and frequency. The given emulator approaches introduce channel effects on digital baseband signals to utilize flexibility. However, baseband emulators require RF signal input to be down-converted, digitized, processed, and up-converted again. Thus, the baseband emulators introduce high processing delays on top of their complex structure and high cost. On the other side, RF domain channel emulators introduce channel effects to the signal without digitization or baseband conversion. [122] introduces an approach using RF mixers to generate the time variation. [123] presents a method that controls coherence

---

[4]This chapter was published in [113]. Permission is included in Appendix A.

time of the channel with stirrers in a reverberation chamber. Similarly, [124] presents a method to manipulate the Doppler spread of a chamber. Because of their straightforward and simple design, reverberation chambers require larger forms that may exceed a room, and they have limited control over the emulated channel.

Complementing the RF circuit design for time dispersive effect of a channel presented in [125], in this study generating frequency dispersion is focused. Thus, a doubly dispersive channel emulator can be implemented by combining both studies. Although [122] already presents a Doppler spread solution as an RF circuit, it requires a complicated process to generate desired effects using the mixers. Similarly, [126] presents a design on single chip to generate channel coefficients but applies them on a very narrow band signal. In this study, a simple novel Doppler emulator design using variable attenuators, switches, and power splitters, is proposed to provide low-cost and real-time solution with a small form factor. The channel variation has been implemented in RF domain by manipulating the attenuation and switching between RF paths with different phases. Therefore, the input RF signal does not need to pass through a costly conversion process into and out of digital domain. The prototype circuit is designed to introduce Doppler spread of air-ground channels. Experimental measurements have been performed to validate the circuit and the results match with the desired environmental channel model.

7.1 Doppler Spread in Wireless Channels

A wireless channel can be modeled with its time varying impulse response as,

$$h(t) = \sum_{i=0}^{M-1} \alpha_i(t)\delta(t - \epsilon_i) \tag{7.1}$$

where α_i and ϵ_i represents i^{th} tap time varying channel coefficient and tap delay, respectively. The channel coefficient $\alpha(t)$ is assumed to be wide sense stationary and the fading process for each tap is modeled as a complex Gausian random process. The power spectral density (PSD) of this process depends on mobility, environmental scatters of the transmitted signal and radiation pattern of transmitter/receiver antenna. For air to ground communication, Doppler spectrum has been
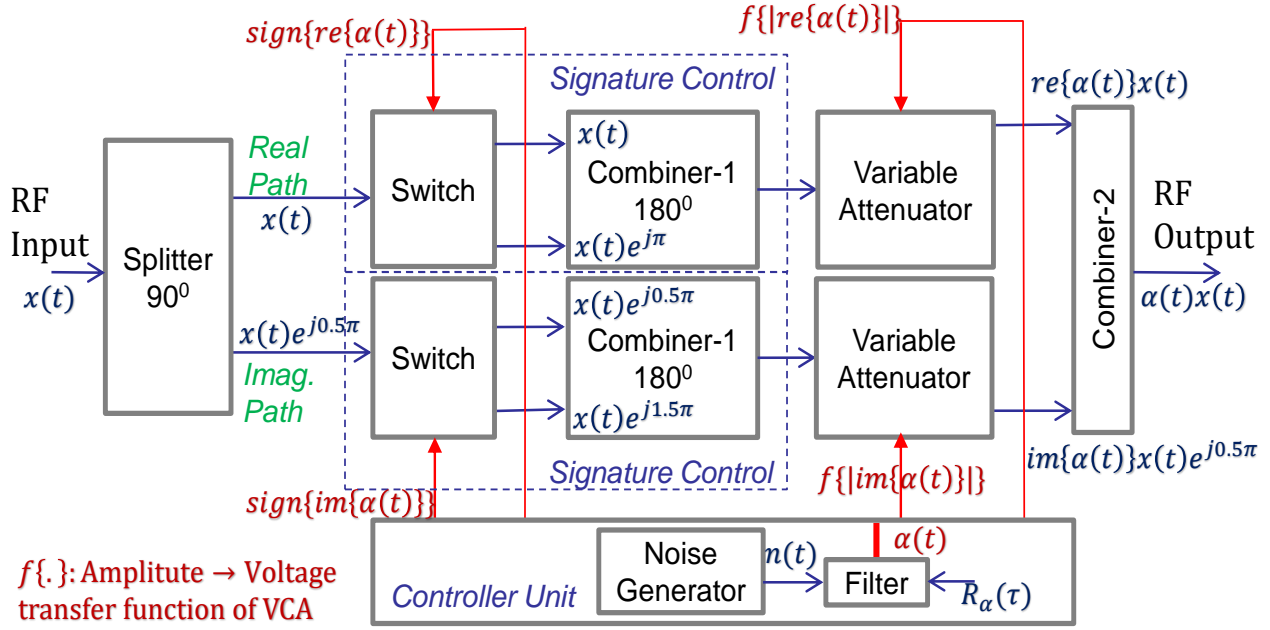
Figure 7.1: RF circuit block diagram

analyzed through theory and measurements in [127, 128], and PSD of α_i can be given as,

$$S(f) = \frac{G}{B\sqrt{\pi}} exp\left(\frac{-(2f^2)}{B^2}\right), \tag{7.2}$$

where G represents path gain and B is the Doppler bandwidth. The Doppler Bandwidth can be given as $B = 2f_c(v/c)\beta \sin \gamma$, where f_c, c, β, v, and γ represent the carrier frequency, speed of light, rms surface slope, the vehicle ground velocity, and elevation angle, respectively. A typical value for rms surface (β) can be given as 0.1 for sea surface [127].

7.2 Doppler Emulator Circuit Design

The Doppler spread effect introduces time varying scaling on the transmitted signal while it passes through the channel. The equation representing this effect can be given as,

$$y(t) = \alpha(t)x(t), \tag{7.3}$$

81

where $y(t)$ and $x(t)$ represent output and input RF signals, respectively. $\alpha(t)$ is the time varying channel coefficient and its auto-correlation function can be written as,

$$R_\alpha(\tau) = \text{IF}\{S(f)\}, \tag{7.4}$$

where $\text{IF}\{.\}$ is inverse Fourier transform. For easier understanding of the circuit design, α coefficient in (7.3) can be rewritten with its real and imaginary parts as,

$$\begin{aligned}\alpha(t) = {}& \text{sign}\{\text{real}\{\alpha(t)\}\} \times |\text{real}(\alpha(t))| \\ & + j \, \text{sign}\{\text{imag}\{\alpha(t)\}\} \times |\text{imag}(\alpha(t))|.\end{aligned} \tag{7.5}$$

The designed circuit given in Fig. 7.1, multiples the input signal with $\alpha(t)$. The coefficients are generated by filtering normally distributed complex noise sequence ($n(t) \sim N(0,1)$) with desired correlation $R_\alpha(\tau)$ given in (7.4). In the block diagram, the first component is a 2 way-90° power splitter which has an output 90° phase-shifted related to the other output. The input signal is divided into two paths by the first component and combined by the last. This process reflects the real and imaginary terms in (7.5). In each path, switches together with Combiner-1, introduce the signature of real and imaginary terms by adding 0° or 180° phase shift. The absolute value in each term is applied with voltage controlled attenuator (VCA) by changing the loss in the path. In addition to signature handling, the controller is also used to generate a time sequence of control voltages which are calculated using the voltage to attenuation transfer function given in the datasheet of the VCA. For the real path, the attenuation value is calculated in each time instant as $20\log_{10}(|\text{real}(\alpha(t))|)$. The calculated attenuation values are increased by 10 dB and clipped to work in the approximately linear part (8 dB to 34 dB) of the transfer function. Same derivations are applied to imaginary part to variate the complex coefficient in time.

During our studies, the following important design factors have been observed.

- In the circuit, when the switch changes its state due to a signature change in imaginary or real part of $\alpha(t)$, it may cause a distortion in the signal during rise and fall time due to non-ideal characteristics of the switch. Since the coefficient is correlated in time, the amplitude will drop before any signature change which will reduce the power of aforementioned distortion to a negligible level.

- As a design criteria, phase unbalance of the power splitters should be as minimum as possible, since it disturbs the signal when combined again. In the components used in our design the maximum phase unbalance introduced by 2 way-90° power splitter as 3.8° at 1.2 GHz. Considering this value, the error caused by the given phase unbalance can be calculated as $-23.6\,\mathrm{dB}$ using $error = \alpha(t)\{1 - e^{j\pi 3.8/180}\}$. This problem can be fixed simply by increasing the trace length between 90° output and the switch. The required increment should be enough to introduce additional 3.8° phase shift. Since the disturbance error is too low, it has been ignored in our design. To keep the error below 1% of desired signal, the phase unbalance should be kept below 5.7°.

- The Doppler bandwidth that can be introduced by the circuit is limited by the processor speed. From Nyquist theorem, the relation can be given as $B < 2f_{control}$ where $f_{control}$ is the maximum possible speed to change each control signal. Note that, rise and fall times of the active components (i.e. Switch, VCA) should be compatible with the desired speeds.

7.3 Experimental Analysis

7.3.1 Measurement Setup and Description

The proposed emulator design was implemented using the components given in Table 7.1. The emulator can be used for the frequency range of 0.82-1.6 GHz, since this is the range that the components can support. It is also possible to implement the circuit for different frequency range by easily changing the components.

Table 7.1: RF circuit component list

Name	Specs.	Producer / Part Number
Combiner1	IL: 0.5 dB, $0.82 - 1.6$ GHz	MiniC. / QCS-152+
Combiner2	IL: 0.8 dB, $0.8 - 2.1$ GHz	MiniC. / GP2S+
Splitter	IL: 1.7 dB, $0.5 - 2.25$ GHz	MiniC. / SYPJ-2-222+
Switch	IL: 1.0 dB, $0.5 - 6$ GHz	MiniC. / VSWA2-63DR+
VCA	IL: 2.6 dB, $0.05 - 6$ GHz	RFMD / RFSA2013
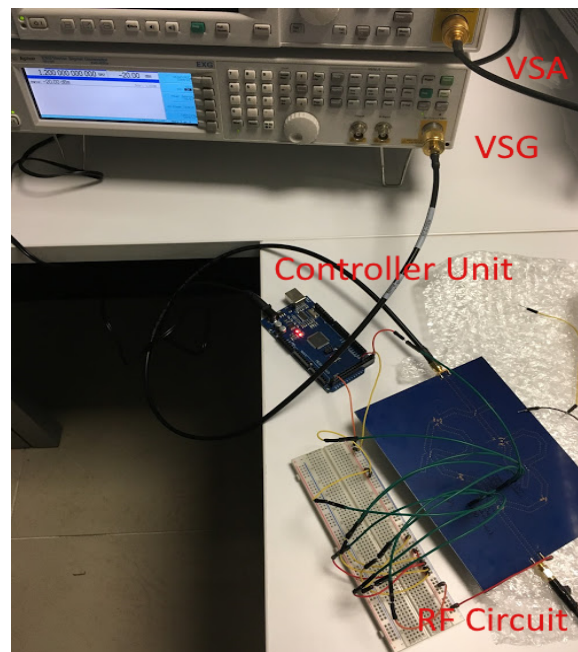
Figure 7.2: Measurement Setup

The prototype circuit has been tested via a setup shown in Fig. 7.2. MATLAB software was used to control vector signal generator (VSG) and vector signal analyzer (VSA) in addition to the processing of the received data. As for VSG and VSA, Keysight N5172B and N9010A were used, respectively. They have a shared 10 MHz reference clock to eliminate any equipment based frequency offset on the signal. VSG has been set to generate a single tone at 1.2 GHz frequency and is fed to the Doppler emulator. The emulated output is taken from the RF circuit to the VSA for analysis. The VSA captured the data at 128 kHz sampling rate for 5 seconds and then the data was ported to MATLAB via network connection.

7.3.2 Measurement Results and Discussion

The PSD of the captured data obtained via Welch's PSD estimator (pwelch) on MATLAB, is given in Fig. 7.3 with 50 Hz resolution bandwidth. The dashed red line shows the PSD of designed coefficients, while solid blue line presents measured signal PSD that is distorted by the emulator. Although, Gaussion PSD is described, the figure compares the performance of the emulator for Gaussian and Jakes' models. As it can be seen from the figure, the Doppler spectrum of the emulated signal matches with desired Doppler Bandwidth and follows a similar shape. The distortion may be caused by truncated attenuation levels and quantized control voltage (50 levels).

Fig. 7.4 shows the in-phase component of the received signal at RF. It can be seen clearly from the figure that unmodulated single tone input signal is distorted by the Doppler emulator and the envelope is changing in time. The coherence time of the signal can be calculated using the equation given in [123] as $T_C = 9/(16\pi B)$. 450 Hz of 10 dB bandwidth from the desired PSD yields $T_C = 0.4$ ms. Fig. 7.4 validates these results as the time domain envelope changes in 0.4 ms.
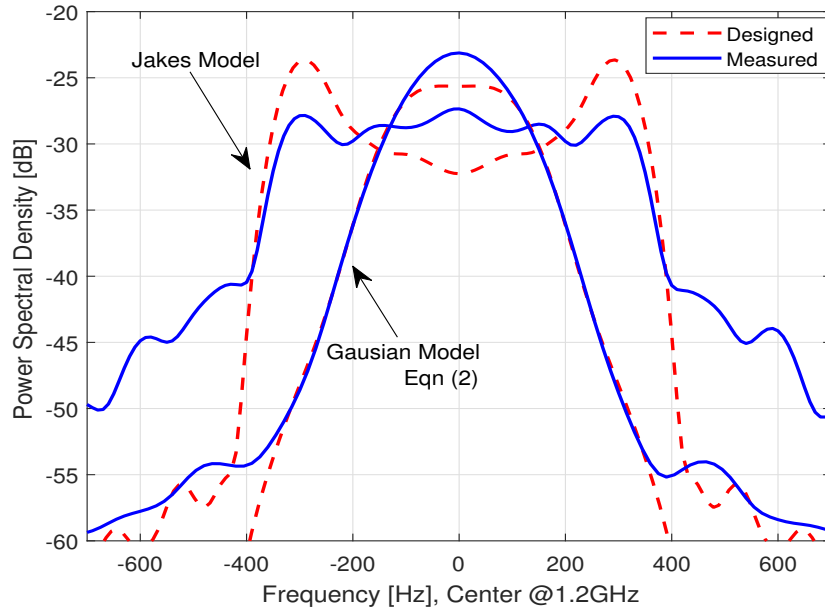
Figure 7.3: PSD of received signal and generated channel coefficients
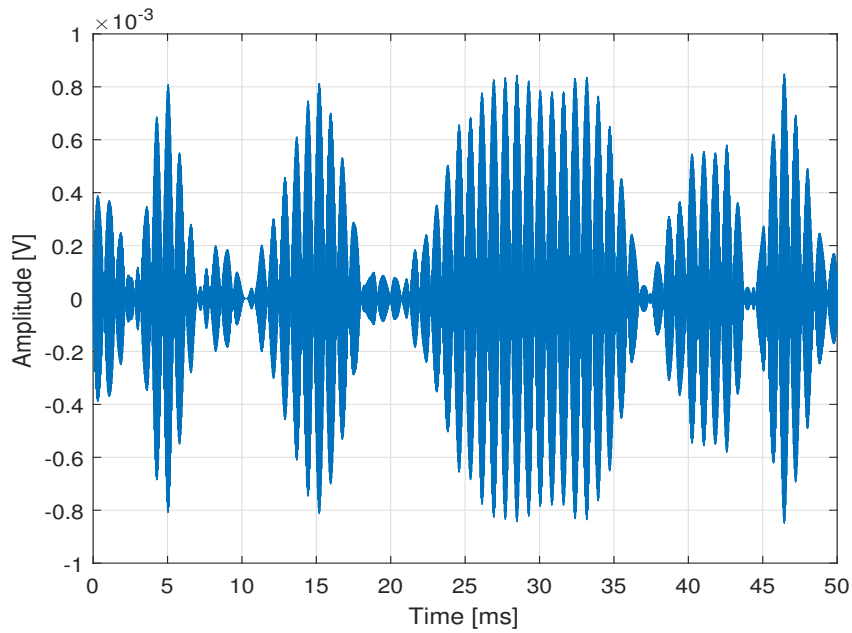
Figure 7.4: In-phase component of the received time domain signal at RF

7.4 Conclusion

A Novel RF domain Doppler emulator has been presented and its prototype is evaluated through experiments. The results validate that the desired time variation can be introduced to input signals. Because of its simple and cheap design, the presented circuit can be used to avoid expensive conversion stages of baseband emulators for frequency spread emulation. Additionally, with the combination of study presented in [125], both time and frequency dispersion can be implemented in RF domain. The design of RF domain channel emulators for MIMO channels, especially for the application of 5G systems, can be a promising future work.

References

[1] T. S. Rappaport, *Wireless communications: principles and practice*. Prentice Hall PTR, 1996.

[2] T. S. Rappaport, Y. Xing, G. R. MacCartney, A. F. Molisch, E. Mellios, and J. Zhang, "Overview of millimeter wave communications for fifth-generation (5G) wireless networks—with a focus on propagation models," *IEEE Trans. Antennas Propag.*, vol. 65, no. 12, pp. 6213–6230, 2017.

[3] Z. Pi and F. Khan, "An introduction to millimeter-wave mobile broadband systems," *IEEE Commun. Mag.*, vol. 49, no. 6, pp. 101–107, 2011.

[4] R. W. Heath, N. Gonzalez-Prelcic, S. Rangan, W. Roh, and A. M. Sayeed, "An overview of signal processing techniques for millimeter wave MIMO systems," *IEEE J. Sel. Topics in Signal Process.*, vol. 10, no. 3, pp. 436–453, 2016.

[5] I. A. Hemadeh, K. Satyanarayana, M. El-Hajjar, and L. Hanzo, "Millimeter-wave communications: Physical channel models, design considerations, antenna constructions, and link-budget," *IEEE Commun. Surveys & Tut.*, vol. 20, no. 2, pp. 870–913, 2017.

[6] Z. Lin, X. Du, H.-H. Chen, B. Ai, Z. Chen, and D. Wu, "Millimeter-wave propagation modeling and measurements for 5G mobile networks," *IEEE Wireless Commun.*, vol. 26, no. 1, pp. 72–77, 2019.

[7] T. S. Rappaport, S. Shu, R. Mayzus, Z. Hang, Y. Azar, K. Wang, G. N. Wong, J. K. Schulz, M. Samimi, and F. Gutierrez, "Millimeter wave mobile communications for 5G cellular: It will work!" *IEEE Access*, vol. 1, pp. 335–349, 2013.

[8] Federal Communications Commission, "FCC takes steps to facilitate mobile broadband and next generation wireless technologies in spectrum above 24 GHz," Tech. Rep., Jul. 2016. [Online]. Available: https://apps.fcc.gov/edocs_public/attachmatch/DOC-340301A1.pdf

[9] J. G. Andrews, S. Buzzi, W. Choi, S. V. Hanly, A. Lozano, A. C. K. Soong, and J. C. Zhang, "What will 5G be?" *IEEE Journal on Selected Areas in Communications*, vol. 32, no. 6, pp. 1065–1082, June 2014.

[10] S. Rangan, T. S. Rappaport, and E. Erkip, "Millimeter-wave cellular wireless networks: Potentials and challenges," *Proceedings of the IEEE*, vol. 102, no. 3, pp. 366–385, March 2014.

[11] T. Bai, A. Alkhateeb, and R. W. Heath, "Coverage and capacity of millimeter-wave cellular networks," *IEEE Communications Magazine*, vol. 52, no. 9, pp. 70–77, September 2014.

[12] A. I. Sulyman, A. T. Nassar, M. K. Samimi, G. R. MacCartney, T. S. Rappaport, and A. Alsanie, "Radio propagation path loss models for 5G cellular networks in the 28 GHz and 38 GHz millimeter-wave bands," *IEEE Communications Magazine*, vol. 52, no. 9, pp. 78–86, 2014.

[13] M. Elkashlan, T. Q. Duong, and H.-H. Chen, "Millimeter-wave communications for 5G: fundamentals: Part I [guest editorial]," *IEEE Communications Magazine*, vol. 52, no. 9, pp. 52–54, 2014.

[14] W. Roh, J.-Y. Seol, J. Park, B. Lee, J. Lee, Y. Kim, J. Cho, K. Cheun, and F. Aryanfar, "Millimeter-wave beamforming as an enabling technology for 5g cellular communications: theoretical feasibility and prototype results," *IEEE Communications Magazine*, vol. 52, no. 2, pp. 106–113, feb 2014.

[15] S. Sun, T. Rappaport, R. Heath, A. Nix, and S. Rangan, "Mimo for millimeter-wave wireless communications: beamforming, spatial multiplexing, or both?" *IEEE Communications Magazine*, vol. 52, no. 12, pp. 110–121, dec 2014.

[16] T. S. Rappaport, F. Gutierrez, E. Ben-Dor, J. N. Murdock, Y. Qiao, and J. I. Tamir, "Broadband millimeter-wave propagation measurements and models using adaptive-beam antennas for outdoor urban cellular communications," *IEEE Transactions on Antennas and Propagation*, vol. 61, no. 4, pp. 1850–1859, April 2013.

[17] Y. Niu, Y. Li, D. Jin, L. Su, and A. V. Vasilakos, "A survey of millimeter wave communications (mmWave) for 5G: Opportunities and challenges," *Wireless Networks*, vol. 21, no. 8, pp. 2657–2676, 2015.

[18] S. Sun, T. S. Rappaport, R. W. Heath, A. Nix, and S. Rangan, "MIMO for millimeter-wave wireless communications: Beamforming, spatial multiplexing, or both?" *IEEE Communications Magazine*, vol. 52, no. 12, pp. 110–121, December 2014.

[19] S. Kutty and D. Sen, "Beamforming for millimeter wave communications: An inclusive survey," *IEEE Communications Surveys Tutorials*, vol. 18, no. 2, pp. 949–973, Secondquarter 2016.

[20] J. G. Andrews, T. Bai, M. N. Kulkarni, A. Alkhateeb, A. K. Gupta, and R. W. Heath, "Modeling and analyzing millimeter wave cellular systems," *IEEE Transactions on Communications*, vol. 65, no. 1, pp. 403–430, Jan 2017.

[21] D. Muirhead, M. A. Imran, and K. Arshad, "A survey of the challenges, opportunities and use of multiple antennas in current and future 5G small cell base stations," *IEEE Access*, vol. 4, pp. 2952–2964, 2016.

[22] F. Sohrabi and W. Yu, "Hybrid digital and analog beamforming design for large-scale MIMO systems," in *2015 IEEE International Conference on Acoustics, Speech and Signal Processing (ICASSP)*, April 2015, pp. 2929–2933.

[23] M. Giordani, M. Mezzavilla, and M. Zorzi, "Initial access in 5G mmwave cellular networks," *IEEE Communications Magazine*, vol. 54, no. 11, pp. 40–47, November 2016.

[24] A. Alkhateeb, Y. H. Nam, M. S. Rahman, J. Zhang, and R. W. Heath, "Initial beam association in millimeter wave cellular systems: Analysis and design insights," *IEEE Transactions on Wireless Communications*, vol. 16, no. 5, pp. 2807–2821, May 2017.

[25] R. Bonjour, M. Singleton, S. A. Gebrewold, Y. Salamin, F. C. Abrecht, B. Baeuerle, A. Josten, P. Leuchtmann, C. Hafner, and J. Leuthold, "Ultra-fast millimeter wave beam steering," *IEEE Journal of Quantum Electronics*, vol. 52, no. 1, pp. 1–8, Jan 2016.

[26] G. M. Rebeiz, S. Y. Kim, O. Inac, W. Shin, O. Gurbuz, Y. C. Ou, F. Golcuk, T. Kanar, and B. H. Ku, "Millimeter-wave large-scale phased-arrays for 5G systems," in *Proc. 2015 IEEE MTT-S International Microwave Symposium*, May 2015, pp. 1–3.

[27] S. Zihir, O. D. Gurbuz, A. Karroy, S. Raman, and G. M. Rebeiz, "A 60 ghz 64-element wafer-scale phased-array with full-reticle design," in *Proc. 2015 IEEE MTT-S International Microwave Symposium*, May 2015, pp. 1–3.

[28] A. Alkhateeb, J. Mo, N. Gonzalez-Prelcic, and R. W. Heath, "MIMO precoding and combining solutions for millimeter-wave systems," *IEEE Communications Magazine*, vol. 52, no. 12, pp. 122–131, dec 2014.

[29] F. Gholam, J. Via, and I. Santamaria, "Beamforming design for simplified analog antenna combining architectures," *IEEE Transactions on Vehicular Technology*, vol. 60, no. 5, pp. 2373–2378, 2011.

[30] X. Zhang, A. Molisch, and S.-Y. Kung, "Variable-phase-shift-based RF-baseband codesign for MIMO antenna selection," *IEEE Transactions on Signal Processing*, vol. 53, no. 11, pp. 4091–4103, nov 2005.

[31] O. E. Ayach, S. Rajagopal, S. Abu-Surra, Z. Pi, and R. W. Heath, "Spatially sparse precoding in millimeter wave MIMO systems," *IEEE Transactions on Wireless Communications*, vol. 13, no. 3, pp. 1499–1513, mar 2014.

[32] C. Rusu, R. Mendez-Rial, N. Gonzalez-Prelcic, and R. W. Heath, "Low complexity hybrid precoding strategies for millimeter wave communication systems," *IEEE Transactions on Wireless Communications*, vol. 15, no. 12, pp. 8380–8393, dec 2016.

[33] R. Mendez-Rial, C. Rusu, N. Gonzalez-Prelcic, A. Alkhateeb, and R. W. Heath, "Hybrid MIMO architectures for millimeter wave communications: Phase shifters or switches?" *IEEE Access*, vol. 4, pp. 247–267, 2016.

[34] A. Mezghani and J. A. Nossek, "On ultra-wideband MIMO systems with 1-bit quantized outputs: Performance analysis and input optimization," in *2007 IEEE International Symposium on Information Theory*, 2007, pp. 1286–1289.

[35] J. Mo, A. Alkhateeb, S. Abu-Surra, and R. W. Heath, "Hybrid architectures with few-bit ADC receivers: Achievable rates and energy-rate tradeoffs," *IEEE Transactions on Wireless Communications*, vol. 16, no. 4, pp. 2274–2287, 2017.

[36] A. Abbaspour-Tamijani and K. Sarabandi, "An affordable millimeter-wave beam-steerable antenna using interleaved planar subarrays," *IEEE Transactions on Antennas and Propagation*, vol. 51, no. 9, pp. 2193–2202, sep 2003.

[37] J. Brady, N. Behdad, and A. M. Sayeed, "Beamspace MIMO for millimeter-wave communications: System architecture, modeling, analysis, and measurements," *IEEE Trans. Antennas and Propag.*, vol. 61, no. 7, pp. 3814–3827, 2013.

[38] Y. Zeng and R. Zhang, "Millimeter wave MIMO with lens antenna array: A new path division multiplexing paradigm," *IEEE Trans. Commun.*, vol. 64, no. 4, pp. 1557–1571, 2016.

[39] Y. J. Cho, G.-Y. Suk, B. Kim, D. K. Kim, and C.-B. Chae, "RF lens-embedded antenna array for mmWave MIMO: Design and performance," *IEEE Communications Magazine*, vol. 56, no. 7, pp. 42–48, jul 2018.

[40] W. Huang, Y. Huang, Y. Zeng, and L. Yang, "Wideband millimeter wave communication with lens antenna array: Joint beamforming and antenna selection with group sparse optimization," *IEEE Transactions on Wireless Communications*, vol. 17, no. 10, pp. 6575–6589, oct 2018.

[41] C. Feng, W. Shen, and J. An, "Beam selection for wideband millimeter wave MIMO relying on lens antenna arrays," *IEEE Communications Letters*, vol. 23, no. 10, pp. 1875–1878, oct 2019.

[42] Y. Zeng, L. Yang, and R. Zhang, "Multi-user millimeter wave MIMO with full-dimensional lens antenna array," *IEEE Transactions on Wireless Communications*, vol. 17, no. 4, pp. 2800–2814, apr 2018.

[43] G. Mumcu, M. Kacar, and J. Mendoza, "Mm-wave beam steering antenna with reduced hardware complexity using lens antenna subarrays," *IEEE Antennas and Wireless Propagation Letters*, vol. 17, no. 9, pp. 1603–1607, sep 2018.

[44] M. Karabacak, G. Mumcu, and H. Arslan, "Hybrid MIMO architecture using lens arrays," U.S. Patent 10 714 836, July 14, 2020.

[45] M. Khalily, R. Tafazolli, T. A. Rahman, and M. R. Kamarudin, "Design of phased arrays of series-fed patch antennas with reduced number of the controllers for 28-GHz mm-Wave applications," *IEEE Antennas and Wireless Propagation Letters*, vol. 15, pp. 1305–1308, 2016.

[46] B. Avser, J. Pierro, and G. M. Rebeiz, "Random feeding networks for reducing the number of phase shifters in limited-scan arrays," *IEEE Transactions on Antennas and Propagation*, vol. 64, no. 11, pp. 4648–4658, 2016.

[47] F. Akbar and A. Mortazawi, "Scalable phased array architectures with a reduced number of tunable phase shifters," *IEEE Transactions on Microwave Theory and Techniques*, vol. 65, no. 9, pp. 3428–3434, 2017.

[48] K. Shila and G. Mumcu, "Mm-wave beam steering antenna based on extended hemispherical lens antenna subarrays," in *2020 IEEE International Symposium on Antennas and Propagation and USNC-URSI Radio Science Meeting*, Jul. 2020, pp. 1–2.

[49] A. Forenza, D. J. Love, and R. W. Heath, "Simplified spatial correlation models for clustered MIMO channels with different array configurations," *IEEE Transactions on Vehicular Technology*, vol. 56, no. 4, pp. 1924–1934, 2007.

[50] Hao Xu, V. Kukshya, and T. S. Rappaport, "Spatial and temporal characteristics of 60-GHz indoor channels," *IEEE Journal on Selected Areas in Communications*, vol. 20, no. 3, pp. 620–630, 2002.

[51] P. F. M. Smulders and L. M. Correia, "Characterisation of propagation in 60 GHz radio channels," *Electronics Communication Engineering Journal*, vol. 9, no. 2, pp. 73–80, 1997.

[52] A. Yazdan, J. Park, S. Park, T. A. Khan, and R. W. Heath, "Energy-efficient massive MIMO: Wireless-powered communication, multiuser MIMO with hybrid precoding, and cloud radio access network with variable-resolution ADCs," *IEEE Microwave Magazine*, vol. 18, no. 5, pp. 18–30, 2017.

[53] S. He, C. Qi, Y. Wu, and Y. Huang, "Energy-efficient transceiver design for hybrid sub-array architecture mimo systems," *IEEE Access*, vol. 4, pp. 9895–9905, 2016.

[54] E. Karami, "Tracking performance of least squares MIMO channel estimation algorithm," *IEEE Transactions on Communications*, vol. 55, no. 11, pp. 2201–2209, 2007.

[55] M. Biguesh and A. B. Gershman, "Training-based MIMO channel estimation: a study of estimator tradeoffs and optimal training signals," *IEEE Transactions on Signal Processing*, vol. 54, no. 3, pp. 884–893, 2006.

[56] M. Karabacak, L. Afeef, and H. Arslan, "Dynamic sidelobe multiplexing in beamspace MIMO systems," *accepted for publication in IEEE Wireless Communications Letters*, 2020.

[57] S. A. Busari, K. M. S. Huq, S. Mumtaz, L. Dai, and J. Rodriguez, "Millimeter-wave massive MIMO communication for future wireless systems: A survey," *IEEE Commun. Surveys & Tut.*, vol. 20, no. 2, pp. 836–869, 2017.

[58] S. Han, I. Chih-Lin, Z. Xu, and C. Rowell, "Large-scale antenna systems with hybrid analog and digital beamforming for millimeter wave 5G," *IEEE Commun. Mag.*, vol. 53, no. 1, pp. 186–194, 2015.

[59] A. Sayeed and J. Brady, "Beamspace MIMO for high-dimensional multiuser communication at millimeter-wave frequencies," in *2013 IEEE GLOBECOM*. IEEE, 2013, pp. 3679–3684.

[60] Q. Xue, X. Fang, and C.-X. Wang, "Beamspace SU-MIMO for future millimeter wave wireless communications," *IEEE J. Sel. Areas in Commun.*, vol. 35, no. 7, pp. 1564–1575, 2017.

[61] K. Yang, X. Yan, K. Qin, and Q. Wang, "A uniform beam selection algorithm for beamspace MIMO-NOMA in millimeter-wave communication system," in *2018 15th ICCWAMTIP*. IEEE, 2018, pp. 166–169.

[62] L. Dai, X. Gao, S. Han, I. Chih-Lin, and X. Wang, "Beamspace channel estimation for millimeter-wave massive MIMO systems with lens antenna array," in *2016 IEEE/CIC ICCC*. IEEE, 2016, pp. 1–6.

[63] B. Wang, L. Dai, Z. Wang, N. Ge, and S. Zhou, "Spectrum and energy-efficient beamspace MIMO-NOMA for millimeter-wave communications using lens antenna array," *IEEE J. Sel. Areas Commun.*, vol. 35, no. 10, pp. 2370–2382, 2017.

[64] B. Wang, L. Dai, X. Gao, and L. Hanzo, "Beamspace MIMO-NOMA for millimeter-wave communications using lens antenna arrays," in *2017 IEEE 86th VTC-Fall*. IEEE, 2017, pp. 1–5.

[65] P. Liu, Y. Li, W. Cheng, W. Zhang, and X. Gao, "Energy-efficient power allocation for millimeter wave beamspace MIMO-NOMA systems," *IEEE Access*, vol. 7, pp. 114 582–114 592, 2019.

[66] V. N. Kamble, S. V. Kadam, and S. R. Choudhury, "A novel user clustering based beamspace MIMO-NOMA," in *2019 IEEE 9th IACC*. IEEE, 2019, pp. 50–54.

[67] J. Li, X. Li, A. Wang, and N. Ye, "Beamspace MIMO-NOMA for millimeter-wave broadcasting via full-duplex D2D communications," *IEEE Trans. Broadcasting*, 2020.

[68] Z. Wei, L. Zhao, J. Guo, D. W. K. Ng, and J. Yuan, "Multi-beam NOMA for hybrid mmwave systems," *IEEE Trans. Commun.*, vol. 67, no. 2, pp. 1705–1719, 2018.

[69] P. Patel and J. Holtzman, "Analysis of a simple successive interference cancellation scheme in a DS/CDMA system," *IEEE J. Sel. Areas Commun.*, vol. 12, no. 5, pp. 796–807, 1994.

[70] B. Ling, C. Dong, J. Dai, and J. Lin, "Multiple decision aided successive interference cancellation receiver for NOMA systems," *IEEE Wireless Commun. Lett.*, vol. 6, no. 4, pp. 498–501, 2017.

[71] M. Karabacak and H. Arslan, "Joint approach to beam optimization and user association," in *IEEE Radio and Wireless Symposium (RWS)*, 2020, pp. 221–224.

[72] O. G. Aliu, A. Imran, M. A. Imran, and B. Evans, "A survey of self organisation in future cellular networks," *IEEE Communications Surveys & Tutorials*, vol. 15, no. 1, pp. 336–361, 2013.

[73] J.-S. Wu, J.-K. Chung, and C.-C. Wen, "Hot-spot traffic relief with a tilted antenna in CDMA cellular networks," *IEEE Transactions on Vehicular Technology*, vol. 47, no. 1, pp. 1–9, 1998.

[74] L. Du, J. Bioham, and L. Cuthbert, "A bubble oscillation algorithm for distributed geographic load balancing in mobile networks," in *IEEE INFOCOM*, vol. 1.   IEEE, Mar. 2004, pp. 330–338.

[75] C.-Y. Liao, F. Yu, V. Leung, and C.-J. Chang, "A novel dynamic cell configuration scheme in next-generation situation-aware CDMA networks," *IEEE Journal on Selected Areas in Communications*, vol. 24, no. 1, pp. 16–25, jan 2006.

[76] S. Das, H. Viswanathan, and G. Rittenhouse, "Dynamic load balancing through coordinated scheduling in packet data systems," in *INFOCOM 2003*, vol. 1.   IEEE, Mar. 2003, pp. 786–796.

[77] O. Yilmaz, S. Hamalainen, and J. Hamalainen, "Analysis of antenna parameter optimization space for 3GPP LTE," in *IEEE Vehicular Technology Conference*, Fall 2009, pp. 1–5.

[78] S. Saur and H. Halbauer, "Exploring the vertical dimension of dynamic beam steering," in *Proc. International Workshop on Multi-Carrier Systems & Solutions*.   IEEE, may 2011, pp. 1–5.

[79] S. Dogan, M. Karabacak, and H. Arslan, "Optimization of antenna beamwidth under blockage impact in millimeter-wave bands," in *Proc. IEEE International Symposium on Personal, Indoor and Mobile Radio Communications (PIMRC)*.   IEEE, sep 2018, pp. 1–5.

[80] A. Awada, B. Wegmann, I. Viering, and A. Klein, "Optimizing the radio network parameters of the long term evolution system using Taguchi's method," *IEEE Transactions on Vehicular Technology*, vol. 60, no. 8, pp. 3825–3839, oct 2011.

[81] 3GPP TR 36.814 v9.0.0, *Further advancements for E-UTRA physical layer aspects*, Mar. 2010.

[82] M. Karabacak, D. Wang, H. Ishii, and H. Arslan, "Mobility performance of macrocell-assisted small cells in manhattan model," in *IEEE 79th Vehicular Technology Conference (VTC Spring)*, 2014, pp. 1–5.

[83] T. Nakamura, S. Nagata, A. Benjebbour, Y. Kishiyama, T. Hai, S. Xiaodong, Y. Ning, and L. Nan, "Trends in small cell enhancements in LTE advanced," *IEEE Communications Magazine*, vol. 51, no. 2, pp. 98–105, 2013.

[84] 3GPP, RWS-120045, *Summary of 3GPP TSG-RAN Workshop on Releae 12 and Onward.*, Jun. 2012.

[85] 3GPP TR 36.932 v12.1.0, *Scenarios and requirements for small cell enhancements for E-UTRA and E-UTRAN*, Mar. 2013.

[86] J.-E. Berg, "A recursive method for street microcell path loss calculations," in *Proc. IEEE Int. Symp. on Personal, Indoor and Mobile Radio Comm.*, vol. 1, 1995, pp. 140–143.

[87] S. Parkvall, E. Dahlman, G. Jöngren, S. Landström, and L. Lindbom, "Heterogeneous network deployments in LTE - the soft-cell approach," *Ericsson review*, 2011.

[88] H. Ishii, Y. Kishiyama, and H. Takahashi, "A novel architecture for LTE-B: C-plane/U-plane split and Phantom Cell concept," in *Proc. IEEE Globecom Wksp.*, Dec. 2012, pp. 624–630.

[89] M. Gudmundson, "Cell planning in manhattan environments," in *Proc. IEEE Veh. Tech. Conf.*, 1992, pp. 435–438 vol.1.

[90] P. E. Ostling, "Implications of cell planning on handoff performance in manhattan environ-ments," in *Proc. IEEE Int. Symp. on Personal, Indoor, and Mobile Radio Comm.*, 1994, pp. 625–629 vol.2.

[91] "Guidelines for evaluation of radio interface technologies for IMT-Advanced," ITU-R M.2135, Tech. Rep., 2008.

[92] H. Jamshid, "CDMA uplink power control methodology in SEAMCAT (voice only)," *CEPT WGSE PT SE21, QUALCOMM*, 2003.

[93] P. W. Shor, "Algorithms for quantum computation: discrete logarithms and factoring," in *Proceedings 35th Annual Symposium on Foundations of Computer Science*, 1994, pp. 124–134.

[94] C. H. Bennett and P. W. Shor, "Privacy in a quantum world," *Science*, vol. 284, no. 5415, pp. 747–748, 1999. [Online]. Available: https://science.sciencemag.org/content/284/5415/747

[95] W. Trappe, "The challenges facing physical layer security," *IEEE Communications Magazine*, vol. 53, no. 6, pp. 16–20, 2015.

[96] J. Qadir, A. Al-Fuqaha, and M. Shafique, "Adversarial ML for vehicular networks: Strategies for attack and defense," in *Proceedings of the IEEE Vehicular Technology Conference-Spring*, 04 2019, pp. 1–150.

[97] A. Ranganathan, H. Ólafsdóttir, and S. Capkun, "SPREE: A spoofing resistant GPS receiver," in *Proceedings of the 22nd Annual International Conference on Mobile Computing and Networking*, ser. MobiCom '16. New York, NY, USA: Association for Computing Machinery, 2016, p. 348–360. [Online]. Available: https://doi.org/10.1145/2973750.2973753

[98] S. Sharma, R. Mishra, and K. Singh, "A survey on cross layer security," *IJCA Proceedings on National Conference on Innovative Paradigms in Engineering and Technology (NCIPET 2012)*, no. 5, pp. 10–14, March 2012.

[99] K. Sharma and M. Ghose, "Cross layer security framework for wireless sensor networks," *International Journal of Security and Its Applications*, vol. 5, pp. 39–52, 01 2011.

[100] X. Wang, P. Hao, and L. Hanzo, "Physical-layer authentication for wireless security enhancement: current challenges and future developments," *IEEE Communications Magazine*, vol. 54, no. 6, pp. 152–158, 2016.

[101] V. Brik, S. Banerjee, M. Gruteser, and S. Oh, "Wireless device identification with radiometric signatures," in *Proceedings of the 14th ACM International Conference on Mobile Computing and Networking*, ser. MobiCom '08. New York, NY, USA: Association for Computing Machinery, 2008, p. 116–127. [Online]. Available: https://doi.org/10.1145/1409944.1409959

[102] Q. Xu, R. Zheng, W. Saad, and Z. Han, "Device fingerprinting in wireless networks: Challenges and opportunities," *IEEE Communications Surveys Tutorials*, vol. 18, no. 1, pp. 94–104, 2016.

[103] X. Duan and X. Wang, "Authentication handover and privacy protection in 5G HetNets using software-defined networking," *IEEE Communications Magazine*, vol. 53, no. 4, pp. 28–35, 2015.

[104] R. B. Ertel, P. Cardieri, K. W. Sowerby, T. S. Rappaport, and J. H. Reed, "Overview of spatial channel models for antenna array communication systems," *IEEE Personal Communications*, vol. 5, no. 1, pp. 10–22, Feb 1998.

[105] H. Lebret and S. Boyd, "Antenna array pattern synthesis via convex optimization," *IEEE Transactions on Signal Processing*, vol. 45, no. 3, pp. 526–532, March 1997.

[106] L. Xiao, L. J. Greenstein, N. B. Mandayam, and W. Trappe, "Using the physical layer for wireless authentication in time-variant channels," *IEEE Transactions on Wireless Communications*, vol. 7, no. 7, pp. 2571–2579, 2008.

[107] M. Hafez, M. Yusuf, T. Khattab, T. Elfouly, and H. Arslan, "Secure spatial multiple access using directional modulation," *IEEE Transactions on Wireless Communications*, vol. 17, no. 1, pp. 563–573, 2018.

[108] B. Peköz, M. Hafez, S. Köse, and H. Arslan, "Reducing precoder/channel mismatch and enhancing secrecy in practical MIMO systems using artificial signals," *IEEE Communications Letters*, vol. 24, no. 6, pp. 1347–1350, 2020.

[109] D. Kapetanovic, G. Zheng, and F. Rusek, "Physical layer security for massive MIMO: An overview on passive eavesdropping and active attacks," *IEEE Communications Magazine*, vol. 53, no. 6, pp. 21–27, June 2015.

[110] Y. A. Eldemerdash, O. A. Dobre, and M. Öner, "Signal identification for multiple-antenna wireless systems: Achievements and challenges," *IEEE Communications Surveys Tutorials*, vol. 18, no. 3, pp. 1524–1551, 2016.

[111] L. Zhang, M. Sun, Z. Ou, C. Ouyang, and H. Yang, "A secure receive spatial modulation scheme based on random precoding," *IEEE Access*, vol. 7, pp. 122 367–122 377, 2019.

[112] D. Tse and P. Viswanath, "MIMO I: spatial multiplexing and channel modeling," in *Fundamentals of Wireless Communication*. Cambridge University Press, 2005, p. 290–331.

[113] M. Karabacak, A. H. Mohammed, M. K. Özdemir, and H. Arslan, "RF circuit implementation of a real-time frequency spread emulator," *IEEE Transactions on Instrumentation and Measurement*, vol. 67, no. 1, pp. 241–243, 2018.

[114] E. Boutillon, J.-L. Danger, and A. Ghazel, "Design of high speed AWGN communication channel emulator," *Analog Integr. Circuits Signal Process.*, vol. 34, no. 2, pp. 133–142, 2003.

[115] E. Boutillon, Y. Tang, C. Marchand, and P. Bomel, "Hardware discrete channel emulator," in *Proc. 2010 IEEE Int. Conf. on High Performance Computing & Simulation (HPCS)*, Caen, France, Jun. 2010, pp. 452–458.

[116] C. Komninakis, "A fast and accurate Rayleigh fading simulator," in *Proc. 2003 IEEE Global Telecommun. Conf. (GLOBECOM)*, San Francisco, CA, Dec. 2003, pp. 3306–3310.

[117] J. Yang, C. A. Nour, and C. Langlais, "Correlated fading channel simulator based on the overlap-save method," *IEEE Trans. Wireless Commun.*, vol. 12, no. 6, pp. 3060–3071, Jun. 2013.

[118] P. Huang, "A novel structure for Rayleigh channel generation with consideration of the implementation in FPGA," *IEEE Tran. Circuits Syst. II, Exp. Briefs*, vol. 63, no. 2, pp. 216–220, Feb. 2016.

[119] J. Mar, C.-C. Kuo, Y.-R. Lin, and T.-H. Lung, "Design of software-defined radio channel simulator for wireless communications: Case study with DSRC and UWB channels," *IEEE Trans. Instrum. Meas.*, vol. 58, no. 8, pp. 2755–2766, Aug. 2009.

[120] A. Stephenne and B. Champagne, "Effective multi-path vector channel simulator for antenna array systems," *IEEE Trans. Veh. Technol.*, vol. 49, no. 6, pp. 2370–2381, 2000.

[121] J. Olmos, A. Gelonch, F. Casadevall, and G. Femenias, "Design and implementation of a wide-band real-time mobile channel emulator," *IEEE Trans. Veh. Technol.*, vol. 48, no. 3, pp. 746–764, May 1999.

[122] Z. Li, W. Ji, G. Zheng, and X. Zhu, "The real-time simulation of doppler spread in wireless mobile environment by RF circuits," *Chinese J. Electron.*, vol. 24, no. 4, pp. 837–843, Oct. 2015.

[123] A. Sorrentino, G. Ferrara, and M. Migliaccio, "On the coherence time control of a continuous mode stirred reverberating chamber," *IEEE Trans. Antennas Propag.*, vol. 57, no. 10, pp. 3372–3374, Oct. 2009.

[124] S. Guzelgoz, S. Yarkan, and H. Arslan, "Investigation of time selectivity of wireless channels through the use of RVC," *Elseiver J. Meas.*, vol. 43, no. 10, pp. 1532–1541, Dec. 2010.

[125] M. Karabacak, A. Sahin, and H. Arslan, "RF domain channel emulation techniques with SAW filters," in *Proc. 2013 Wireless Inn. Forum Conf. on Commun. Technol. and Softw. Defined Radio (WInnComm)*, Washington, DC, Jan. 2013.

[126] R. Goubran, H. Hafez, and A. Sheikh, "Implementation of a real-time mobile channel simulator using a DSP chip," *IEEE Trans. Instrum. Meas.*, vol. 40, no. 4, pp. 709–714, 1991.

[127] R. Sutton, E. Schroeder, A. Thompson, and S. Wilson, "Satellite-aircraft multipath and ranging experiment results at L band," *IEEE Trans. Commun.*, vol. 21, no. 5, pp. 639–647, May 1973.

[128] P. Bello, "Aeronautical channel characterization," *IEEE Trans. Commun.*, vol. 21, no. 5, pp. 548–563, May 1973.

Appendix A: Copyright Permissions

Dynamic Sidelobe Multiplexing in Beamspace MIMO Systems

Author: Murat Karabacak

Publication: IEEE Wireless Communications Letters (L-WC)

Publisher: IEEE

Date: Dec 31, 1969

Copyright © 1969, IEEE

Thesis / Dissertation Reuse

The IEEE does not require individuals working on a thesis to obtain a formal reuse license, however, you may print out this statement to be used as a permission grant:

Requirements to be followed when using any portion (e.g., figure, graph, table, or textual material) of an IEEE copyrighted paper in a thesis:

1) In the case of textual material (e.g., using short quotes or referring to the work within these papers) users must give full credit to the original source (author, paper, publication) followed by the IEEE copyright line © 2011 IEEE.
2) In the case of illustrations or tabular material, we require that the copyright line © [Year of original publication] IEEE appear prominently with each reprinted figure and/or table.
3) If a substantial portion of the original paper is to be used, and if you are not the senior author, also obtain the senior author's approval.

Requirements to be followed when using an entire IEEE copyrighted paper in a thesis:

1) The following IEEE copyright/ credit notice should be placed prominently in the references: © [year of original publication] IEEE. Reprinted, with permission, from [author names, paper title, IEEE publication title, and month/year of publication]
2) Only the accepted version of an IEEE copyrighted paper can be used when posting the paper or your thesis on-line.
3) In placing the thesis on the author's university website, please display the following message in a prominent place on the website: In reference to IEEE copyrighted material which is used with permission in this thesis, the IEEE does not endorse any of [university/educational entity's name goes here]'s products or services. Internal or personal use of this material is permitted. If interested in reprinting/republishing IEEE copyrighted material for advertising or promotional purposes or for creating new collective works for resale or redistribution, please go to http://www.ieee.org/publications_standards/publications/rights/rights_link.html to learn how to obtain a License from RightsLink.

If applicable, University Microfilms and/or ProQuest Library, or the Archives of Canada may supply single copies of the dissertation.

BACK   CLOSE WINDOW

The permission above is for the use of materials in Chapter 3.

The permission above is for the use of materials in Chapter 4.

The permission above is for the use of materials in Chapter 5.

The permission above is for the use of materials in Chapter 7.

About the Author

Murat Karabacak received his B.S. and M.Sc. degrees in Electrical and Electronics Engineering from Istanbul University, Istanbul, Turkey in 2008 and 2010, respectively. He is currently pursuing his Ph.D. degree in Electrical Engineering at the University of South Florida. In 2013, he was with the research group of NTT Docomo Inc., CA, USA, as an intern where he was involved in the research of mobility, load balancing, analog beamforming in small cells. His research interests are physical and medium access control layer algorithms on mobility management, initial access, and self-organization in cellular networks for optimization of efficient control in wireless networks.